Technische Universität München
Max-Planck-Institut für Biochemie
Abteilung für Molekulare Strukturbiologie

Image analysis of molecular complexes present in cryo-tomograms of neuronal synapses

Zdravko Kochovski

Vollständiger Abdruck der von der Fakultät für Physik
der Technischen Universität München
zur Erlangung des akademischen Grades eines
Doktors der Naturwissenschaften
genehmigten Dissertation.

Vorsitzender:		Univ.-Prof. Dr. A. Bausch
Prüfer der Dissertation:	1.	Hon.-Prof. Dr. W. Baumeister
	2.	Univ.-Prof. Dr. M. Zacharias

Die Dissertation wurde am 27.06.2014 bei der Technischen Universität München eingereicht
und durch die Fakultät für Physik am 17.07.2014 angenommen.

Contents

1 Abstract

The postsynaptic density (PSD) is a complex molecular machine that controls the strength of synaptic signaling and plays a major role in synaptic plasticity. While previous studies have provided some insights on its structure, further work is needed to elucidate its precise supramolecular organization, which is considered to be essential for its function.

We employed Cryo-electron tomography to study the native, three-dimensional supramolecular architecture of the PSD in both pharmacologically treated and control synaptosomes, and PSDs isolated from such synaptosomes. Furthermore, we used template matching to detect CaMKII, a major postsynaptic protein and key regulator of long-term potentiation (LTP), in these tomograms. Since a number of structural studies have previously produced highly diverging views of the CaMKII holoenzyme structure and because no structure existed for the activated state of CaMKII, a part of this work was to obtain the structures of both activated and non-active CaMKII by Cryo-EM single particle analysis.

We showed that NMDAR stimulation of synaptosomes can induce a significant increase in the amount of Thr286 phosphorylated CaMKII, and induce translocation of CaMKII from distal parts of the postsynaptic terminal to the PSD. However, no clear morphological differences could be visually discerned between PSDs from pharmacologically treated and control synaptosomes. Our data suggests that the core structure of the PSD consists of a mesh-like scaffold consisting of a dense network of filaments, oriented parallel and perpendicular to the synaptic cleft, that serve the role of a foundation on top of which additional PSD components can attach.

We solved the 3D structures of activated and non-active recombinantly expressed mouse CaMKII by sub-tomogram averaging and single particle analysis. However, we were

unable to reliably detect these structures by template matching in tomograms collected on scintilator-coupled CCDs, suggesting that tomograms of higher resolution, such as the made possible by the combination of TEM phase plates and DDDs, will be required for the faithful detection.

2 Introduction

2.1 The chemical synapse

Neurons send signals to individual target cells via specialized intercellular junctions called synapses. In the case of chemical synapses in the mammalian central nervous system, these signals come in the form of a neurotransmitter that gets released onto the target cell upon stimulation. This unidirectional signaling gives rise to the formation of distinct structures on each side of the synapse (respectively termed pre- and postsynaptic terminals) separated by a 20-25 nm gap commonly known as the synaptic cleft. Presynaptic terminals (or boutons) are specialized portions of the axon containing neurotransmitter-filled synaptic vesicles, the molecular machinery required for their fusion and recycling and a number of supporting structures and organelles, such as mitochondria and endoplasmic reticulum. Usually located on dendritic spines and held tightly to the presynaptic terminal by the cell adhesion molecules of the synaptic cleft is the postsynaptic terminal. It is characterized by an aggregation of neurotransmitter receptors, scaffolding proteins, signaling molecules and cytoskeletal elements assembled into a highly organized and electron-dense structure known as the postsynaptic density (PSD). Synaptic signaling involves the fusion of the neurotransmitter-filled synaptic vesicles with the presynaptic plasma membrane followed by the release of neurotransmitter molecules into the cleft and the subsequent activation of receptors in the postsynaptic plasma membrane. The vast majority of synapses in the CNS are of the aforementioned type and are typically regarded to as excitatory or glutamatergic synapses (since they use glutamate as neurotransmitter).

2.2 The postsynaptic terminal of excitatory synapses

The postsynaptic membrane is the first place where signals from the axon carried by the neurotransmitter glutamate get processed as they arrive at the dendrite. Ionotropic glutamate receptors on the postsynaptic membrane mediate most of the excitatory

synaptic signaling in the CNS and function by opening their associated ion selective transmembrane ion channels following glutamate binding. Glutamate targets at least two discrete types of ionotropic glutamate receptors on the postsynaptic membrane: -amino-3-hydroxy-5-methyl-4-isoxazolepropionic acid receptors (AMPARs) and N-methyl-D-aspartate receptors (NMDARs). These glutamate receptors mediate most of the fast excitatory synaptic signaling in the CNS via the ion flux through their associated channels. In contrast to AMPARs, NMDARs channel opening requires both glutamate binding and the depolarization-mediated removal of Mg2+ ions that block the channel in a voltage-dependent manner in order to allow ion flux. Calcium ions (Ca2+) influx through NMDARs plays a critical role in excitatory synaptic signaling and plasticity (Franks and Sejnowski, 2002). The major part of the machinery required for further processing of the signal is contained in the postsynaptic density attached to the cytosolic face of the postsynaptic membrane. Much of the molecular diversity of synapses lies in the postsynaptic terminal and this where the signal transduction events leading to long term synaptic plasticity take place (Sheng and Hoogenraad, 2007).

2.2.1 The postsynaptic density

The PSD is a complex molecular machine visible in the electron microscope as a thickening of the postsynaptic membrane, extending some tenths of nanometers into into the cytosol. Consisting of hundreds of distinct proteins it regulates the strength of synaptic signaling and has a major role in synaptic plasticity. The structure and composition of the PSD can be modified by external stimuli and synaptic activity over the time course of seconds to minutes and hours to days (Sheng and Hoogenraad, 2007). One way to gain an understanding on postsynaptic signal processing is to unravel the structures, functions and physical interconnections of the proteins in the PSD. Functionally, its core constituents can be broadly categorized in the following groups: ion channels/receptors (glutamate-activated channels/receptors NMDAR and AMPAR), scaffolding proteins (PSD-95 family, GKAP, Shank, Homer), signaling proteins (Calcium/calmodulin de-

pendent protein kinase II - CaMKII, SynGAP) and cytoskeleton-related proteins (actin, α-actinin). Many other proteins were identified in the recent years by mass-spectrometry (MS), with their number currently reaching few hundred (Husi et al., 2000; Peng et al., 2004; Cheng et al., 2006; Walikonis et al., 2001). The current understanding of the molecular organization of the PSD is to a great extent based on studies of specific protein-protein interactions of PSD proteins (Figure 1).

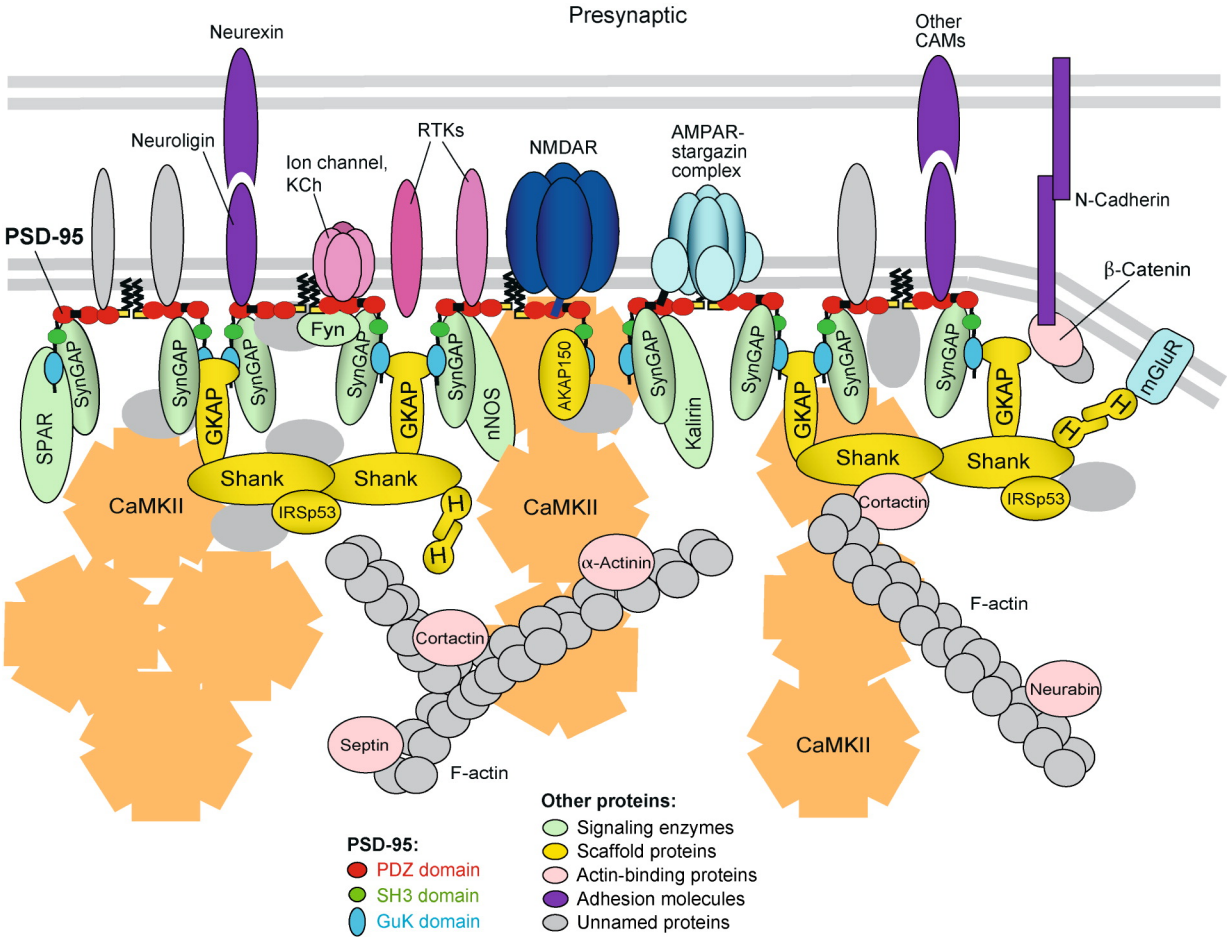

AR Sheng M, Hoogenraad CC. 2007.
Annu. Rev. Biochem. 76:823–47

Figure 1: Organization of proteins and protein-protein interactions in the PSD (adapted from (Sheng and Hoogenraad, 2007)).

A fraction of CaMKII is expected to be found close to the membrane due to its binding

to the NMDAR (Bayer et al., 2001). PSD-95 binds NMDARs directly and AMPARs through an intermediate protein (Kim and Sheng, 2004). Furthermore, palmitoylation may anchor PSD-95 to the postsynaptic membrane (El-Husseini et al., 2002). PSD-95 is also known to multimerize and cluster Kv1.4 voltage-gated potassium channels, although it is not clear what the mechanism controlling these processes is (Hsueh et al., 1997; Christopherson et al., 2003). All taken together, the PDS-95 family is thought to provide a structural scaffold that organizes channels, as well as other proteins in the PSD. Shank, on the other hand, is thought to provide another scaffolding structure, a bit further away from the postsynaptic membrane. Its binding to GKAP (a PSD-95 binding protein) provides a connection to the PSD-95 scaffold and it also binds Homer, which in turns can bind both metabotropic glutamate receptors on the cell membrane and IP3 receptors (Sheng and Kim, 2000). Shank itself might multimerize through the association of some of its domains. The SAM-SAM domain binding (Naisbitt et al., 1999) is of particular structural interest, because the atomic structure of a sheet formed by isolated SAM domains has been solved (Baron et al., 2006).

The interaction maps of PSD proteins can reveal a lot of information in an abstract way, but they are also potentially misleading, especially with hundreds of distinct proteins estimated in the PSD. A better functional insight into the postsynaptic molecular architecture requires an understanding of the stoichiometry and 3D structure of individual PSD components. The high and even medium resolution structures of the core PSD proteins are scarce. The atomic structures were determined for the individual domains of PSD-95 (Doyle et al., 1996; McGee et al., 2001), while for the whole PSD-95 a relatively low-resolution negative stain single particle electron microscopy (EM) structure shows a 10 nm long curled worm-like particle (Nakagawa et al., 2004). Different attempts to determine the structure of full-length CaMKII holoenzymes have produced contradictory views on the quaternary organization of this important signaling enzyme (please refer to section 2.2.2 for details). The atomic structure of a whole homomeric AM-

PAR has been determined by X-ray crystallography (Sobolevsky et al., 2009). There, however, appears to be a controversy between different structures of whole AMPARs obtained by negatively stain single-particle EM. While the structures of two different homomeric AMPARs show well-defined dimer-of-dimers conformations (Tichelaar et al., 2004; Midgett and Madden, 2008), the structures of native heteromeric AMPARs have multiple conformations (Nakagawa et al., 2005, 2006). Only individual domain structural information exists for the rest of the core PSD proteins. For determining the stoichiometry of some of the core molecules two approaches have been employed. Quantitative MS was used to provide absolute values for the molar amounts of the core PSD constituents (Cheng et al., 2006). Using the estimate for an average PSD mass from scanning transmission electron microscopy, numbers of core molecules per synapse were determined (Chen et al., 2005; Sheng and Hoogenraad, 2007). According to these studies, an average synapse is expected to contain around 20 NMDARs (four subunits each), 300 PSD-95s, 150 Shanks, 60 Homers, 5600 CaMKII subunits (12 subunits form a CaMKII holoenzyme) and 360 SynGAPs. It still remains a mystery why two enzymes - CaMKII and SynGAP - are so abundant in the PSD. Another approach was based on quantitative fluorescence measurements of overexpressed fusion proteins and immunocytochemistry in neuronal cultures (Sugiyama et al., 2005). The number of scaffolding proteins determined in this study (PSD-95, Shank, Homer) were all around 300. While the issues related to the two techniques used likely contribute to this discrepancy, sample differences may indicate that a portion of Shank and Homer population is loosely attached, or just localized near the PSD in the living cells, and is therefore not retained in the (detergent-extracted) PSD-fraction.

2.2.2 Calcium/calmodulin dependent protein kinase CaMKII

Calcium/calmodulin-dependent protein kinase II (CaMKII), a prominent mediator of Ca^{2+}-associated neural signaling, is a ubiquitous multifunctional serine/threonine kinase forming a dodecameric holoenzyme capable of reacting to both the amplitude and

frequency of activating Ca^{2+} pulses. It is highly concentrated in dendritic spines and it is a major component of the PSD. CaMKII is activated by the Ca^{2+}/calmodulin complex which displaces an autoinhibitory segment that otherwise blocks the active site of the enzyme. Upon activation this segment undergoes an autophosphorylation at a specific threonine residue Thr286 (mouse CaMKIIα numbering) which renders the enzyme active even in the absence of Ca^{2+}/calmodulin (Miller and Kennedy, 1986; Hanson et al., 1989; De Koninck and Schulman, 1998). Ca^{2+} influx through NMDARs and the resulting CaMKII activation by the Ca^{2+}/calmodulin complex have been shown crucial for the induction and maintenance of long-term potentiation (LTP), a physiological correlate for learning and memory characterized by the long-lasting strengthening of synaptic transmission induced by brief intervals of high-frequency synaptic stimulation (Fukunaga et al., 1993; Barria et al., 1997; Ouyang et al., 1999). A major role for CaMKII in the regulation of excitatory synaptic transmission has been already proposed almost three decades ago when it was identified as a major postsynaptic density protein (Erondu and Kennedy, 1985). There are four closely related CaMKII genes in mammals: α, β, γ and δ (Tobimatsu and Fujisawa, 1989; Karls et al., 1992). CaMKIIα and CaMKIIβ are the isoforms predominantly expressed in the brain, making up 1-2% of the total protein in the hippocampus (Erondu and Kennedy, 1985). These isoforms can form α or β homomultimers and α/β heteromultimers with each form of the holoenzyme having a markedly different role in regulating neuronal function (Griffith et al., 2003). CaMKIIα is especially enriched at regions of the brain displaying persistent LTP (Racine et al., 1983; Swanson et al., 1982) and is the isoform responsible for the anchoring of the CaMKII holoenzyme to the PSD (Miller and Kennedy, 1985). Each CaMKII subunit contains an N-terminal (Ser/Thr-specific) kinase domain, followed by an autoregulatory segment containing three essential autophosphorylation sites: Thr286, Thr305, and Thr306 (mouse CaMKIIα numbering) (Hudmon and Schulman, 2002) (Figure 2).

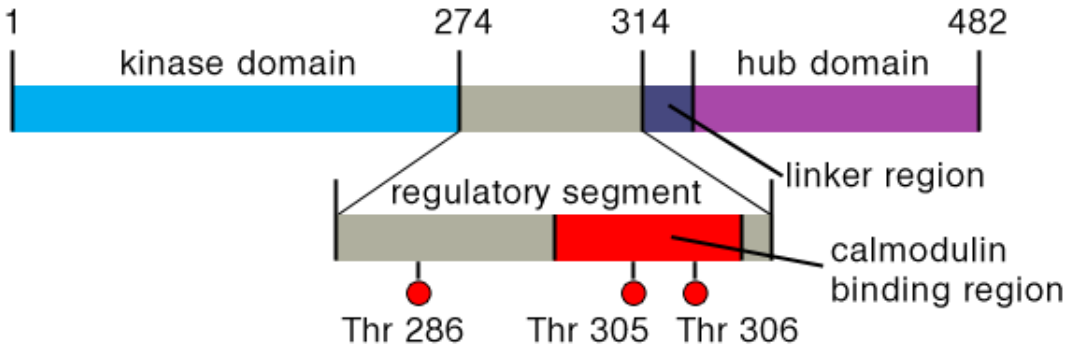

Figure 2: Domain architecture of an individual CaMKII subunit: the kinase domain (blue) is followed by a regulatory segment (gray), a variable linker region (dark blue), and the association (hub) domain (magenta). The regulatory segment contains the autophosphorylation site Thr286 and the calmodulin-binding region (red) containing Thr305 and Thr306.

Thr305 and Thr306 are located at the calmodulin-binding site of the autoregulatory segment and their phosphorylation prevents Ca^{2+}/calmodulin binding, hence serving an inhibitory role in the activation of the enzyme (Colbran, 1993; Hanson and Schulman, 1992). Thr286 is located at the base of an α helix within the autoregulatory segment that inhibits the binding of Ca^{2+}/calmodulin by docking to a hydrophobic patch on the kinase domain. Phosphorylation at Thr286 disrupts this docking and keeps the enzyme in its active state even in the absence of Ca^{2+}/calmodulin (Lai et al., 1986; Miller and Kennedy, 1986; Yang and Schulman, 1999). The autoregulatory segment is followed by a variable linker region that connects to the C-terminal hub domain (also referred to as the association domain). The hub domains are necessary for the formation of the CaMKII holoenzyme and assemble into two stacked hexameric rings giving rise to the dodecameric holoenzyme (Shen and Meyer, 1998; Kolodziej et al., 2000; Hoelz et al., 2003; Rellos et al., 2010). With the kinase and association domains of the different CaMKII isoforms being very similar (∼95% and ∼80% sequence identity respectively), the main difference between the different isoforms lies within the linker region that can vary in both length and sequence (Tombes et al., 2003). Different structural studies have produced diverging views of the CaMKII holoenzyme structure. Electron microscopy (EM)

cryo and negative stain preparations of full-length mouse CaMKII holoenzymes have yielded similar dodecameric structures with the kinase domains extending above and below the midplane of the central association domain (Kolodziej et al., 2000; Gaertner et al., 2004). This arrangement is somewhat similar to a recent X-ray structure of full-length human CaMKIIα construct with a very short CaMKIIβ7 (an alternative splicing variant of human CaMKIIβ) linker region (Chao et al., 2011). In another EM study using negative stain preparations of full-length mouse CaMKII holoenzymes, the kinase domains were however arranged in a ring coplanar with the midplane of the central association domain (Morris and Torok, 2001), an arrangement similar to the one seen in models of the CaMKII holoenzyme based on Small-angle X-ray scattering (SAXS) (Rosenberg et al., 2005).

Several studies have demonstrated that upon activation, CaMKII can translocate from the dendritic cytoplasm to the PSD. For example, real-time imaging of GFP-tagged CaMKII in cultured hippocampal neurons has revealed a fast (within seconds) postsynaptic translocation upon application of glycine-glutamate (a pharmacological treatment targeting the NMDAR) (Shen and Meyer, 1999). This translocation requires Calmodulin binding to CaMKII, and Thr286 autophosphorylation enhances its association with the PSD. Induction of LTP in rat hippocampal slices has been shown to result in a persistent translocation and accumulation of CaMKII at the PSD Otmakhov et al. (2004). It has been demonstrated that such translocations are the specific result of NMDAR-mediated postsynaptic Ca^{2+} influx (Thalhammer et al., 2006). In another study, brief pharmacological NMDAR stimulation of hippocampal slices and cultured neurons caused a rapid (1.5 min.) increase of the thickness of their PSDs that was at least in part a result of CaMKII accumulation on their cytosolic faces (Dosemeci et al., 2001). The majority of known CaMKII binding proteins are present in the PSD, including the NMDAR, actin, α-actinin, densin-180 and SynGAP, among others (Colbran, 2004; Merrill et al., 2005; Shen et al., 1998; Li et al., 2001; Walikonis et al., 2001; Robison et al., 2005).

Upon translocation to the PSD, CaMKII directly binds to the NMDAR (Bayer et al., 2001) and this binding is enhanced by Thr286 autophosphorylation (Strack and Colbran, 1998; Leonard et al., 1999; Strack et al., 2000; Bayer et al., 2001). There are several clues that link CaMKII postsynaptic translocation to the initiation of structural rearrangements in the PSD. The CaMKII binding domain on the NR1 subunit of the NMDAR overlaps NR1s Calmodulin and α-actinin-2 binding sites creating a situation in which these proteins compete for occupancy Leonard et al. (2002). Whats more, CaMKII competes with PSD95 for a binding site on the NR2A subunit of the NMDAR (Gardoni et al., 1999). Furthermore, protein kinase C-dependent CaMKII translocation to the PSD is accompanied by a rapid loss of synaptic NMDARs (Fong et al., 2002). Additionally CaMKII activation and postsynaptic translocation induce the synaptic trapping of AMPARs diffusing in the postsynaptic membrane (Opazo et al., 2010). These findings suggest that the postsynaptic translocation of CaMKII has an important role in the dynamic remodeling and organization of the PSD which are thought to be a fundamental aspect of postsynaptic signal transduction. Once localized at the PSD, CaMKII is also strategically positioned to sense Ca^{2+} entry through NMDARs and transduce these signals into changes in the phosphorylation state and activity of molecules important for synaptic signaling. In fact, a large number of CaMKII phosphorylation sites have been identified by mass spectrometry in PSD fraction (Trinidad et al., 2006).

2.2.3 Structural studies on the postsynaptic architecture using electron microscopy

The first reported observation of a dense region on the postsynaptic membrane was made in an early EM study on the ultrastructural architecture of CNS synapses (Palade and Palay, 1954). The existence of the PSD was confirmed in later EM studies (Palay, 1956, 1958) and while some described its structure as granular in nature (Gray, 1959) others considered it to be somewhat filamentous (De Robertis, 1962). More recently,

quantitative immunogold EM revealed a laminar organization of scaffold proteins within the PSD (Valtschanoff and Weinberg, 2001). PSD-95 was found to lie in the vicinity of the postsynaptic membrane (12 nm from its extracellular face), close to the cytoplasmic tails of NMDAR NR2 subunits. Shank and GKAP, on the other hand, were found to occupy a deeper position within the PSD (24-26 nm). The combination of immunolabeling with EM tomography has demonstrated that PSD95 forms perpendicular filaments at the PSD (Chen et al., 2008), which are in contact with parallel filaments, most likely composed of PSD95-binding partners such as GKAP, Shank and SynGAP, among others (Chen et al., 2011). Immunogold EM has also presented evidence for the heterogeneous distribution of NMDARs and AMPARs within the plane of the PSD, revealing that NMDARs are concentrated in the middle of the PSD, while AMPARs appear to be predominantly localized at its periphery (Kharazia and Weinberg, 1997; Racca et al., 2000). Rotary shadowing EM has provided three-dimensional structural information of isolated PSDs, revealing a somewhat smooth cleft surface and a convoluted cytoplasmic surface (Petersen et al., 2003). Immunogold labeling in this study showed CaMKII lying exclusively at the cytoplasmic surface of the PSD, associated with tower-like protrusions. More recently PSDs isolated from different developmental time points and studied by negative stain EM tomography were found to exhibit distinct morphological characteristics (Swulius et al., 2010). Very recently, attempts were also made to visually detect CaMKII at EM tomograms of isolated PSDs (Fera et al., 2012). The data in this study suggests that approximately half of the identified CaMKII molecules lie at the cytoplasmic surface of the PSD, while the rest are scattered throughout its thickness. Although those and other EM studies have produced information on the postsynaptic structural organization, further studies aiming to elucidate the precise supramolecular organization of the PSD are needed. Importantly, these studies have made use of conventional electron microscopy sample preparation techniques involving contrast enhancing heavy metals stains, dehydration, chemical fixation, embedding, sectioning and heavy metal evaporation. These techniques are known to introduce a number of artifacts such as

protein aggregation and structural rearrangements within the specimen and as a result can not ensure its structural preservation. Cryo-electron tomography (cryo-ET), on the other hand (please refer to section 3.3 for details) provides three-dimensional views of the molecular components of the cell in their native, fully hydrated environment, and is therefore uniquely positioned to unravel the native postsynaptic supramolecular organization.

3 Three-dimensional Electron microscopy

Three dimensional electron microscopy is capable of determining the three dimensional structure of biological specimens ranging from macromolecules and macromolecular assemblies to viruses, organelles and even whole cells. There are two main non-crystallographic methods for the reconstruction of the three-dimensional structure of objects imaged in an electron microscope. One method relies on the averaging of images of multiple identical copies of specimens, usually proteins, macromolecular assemblies or viruses, randomly oriented relative to the electron beam and is commonly referred to as single particle electron microscopy. The other method, commonly used for the structure determination of pleomorphic objects such as whole cells and organelles, involves the tilting of the sample under the electron beam in order to obtain projections at different sample orientations and the computational merging of the said projections into a 3D reconstruction (tomogram). This method, commonly referred to as electron tomography, can also be applied to macromolecular complexes or viruses present in multiple copies. In this case sub-tomograms containing single copies of the particle can be identified in the tomogram and computationally extracted, and averaged in order to obtain a higher-resolved structure, a technique called subtomogram averaging. Both methods described above have been applied to the work presented here and are discussed in detail in the current section along with the relevant principles of transmission electron microscopy (TEM) and cryo-sample preservation techniques, allowing the visualization biological samples in a functional and close to native frozen-hydrated state.

3.1 Principles of transmission electron microscopy (TEM)

The transmission electron microscope (TEM) is in many aspects similar to a light microscope, but instead of photons it uses accelerated electrons. For biological samples ,

medium acceleration voltages (120-300 kV) are used. Electrons interact strongly with matter thus limiting the specimen thickness. For instance in the case of 120 keV electrons and vitreous ice at liquid-N temperature, the mean free path for elastic and inelastic scattering are 280 nm and 85 nm respectively, which indicates that TEM samples can be up to few 100 nm thick. Because electrons are also scattered by air, the TEM column must be kept at high vacuum. The wavelength of electrons accelerated to 200 keV is 0.025 Å, which could theoretically allow achieving extremely high resolution. However, the resolution of the best electron microscopes is around 0.5 Å (Kisielowski et al., 2008).

The interaction of electrons with organic samples breaks chemical bonds and releases free radicals, that in turn causes further damage to the sample (Glaeser and Taylor, 1978). This further limits the achievable resolution reached by electron microscopy of biological samples, since it imposes a limitation on the amount of electron illumination, which in turn results in a very low signal to noise ratio (SNR) of the resulting images. For the past few decades the approach most commonly used to overcome that limitation has been to apply a heavy metal stain to the sample, usually in the form of a heavy metal salt (see section 3.2). While the stain doesn't protect organic material, it is more resistant to electron-induced radiation damage and can significantly improve the SNR in resulting images, primarily by an enhancement of amplitude contrast (see section 3.1.3). Heavy metal staining comes at the cost of losing high resolution features and internal structural details, mainly due to the fact that the information recovered in the image is limited to molecular surfaces accessible to the stain.

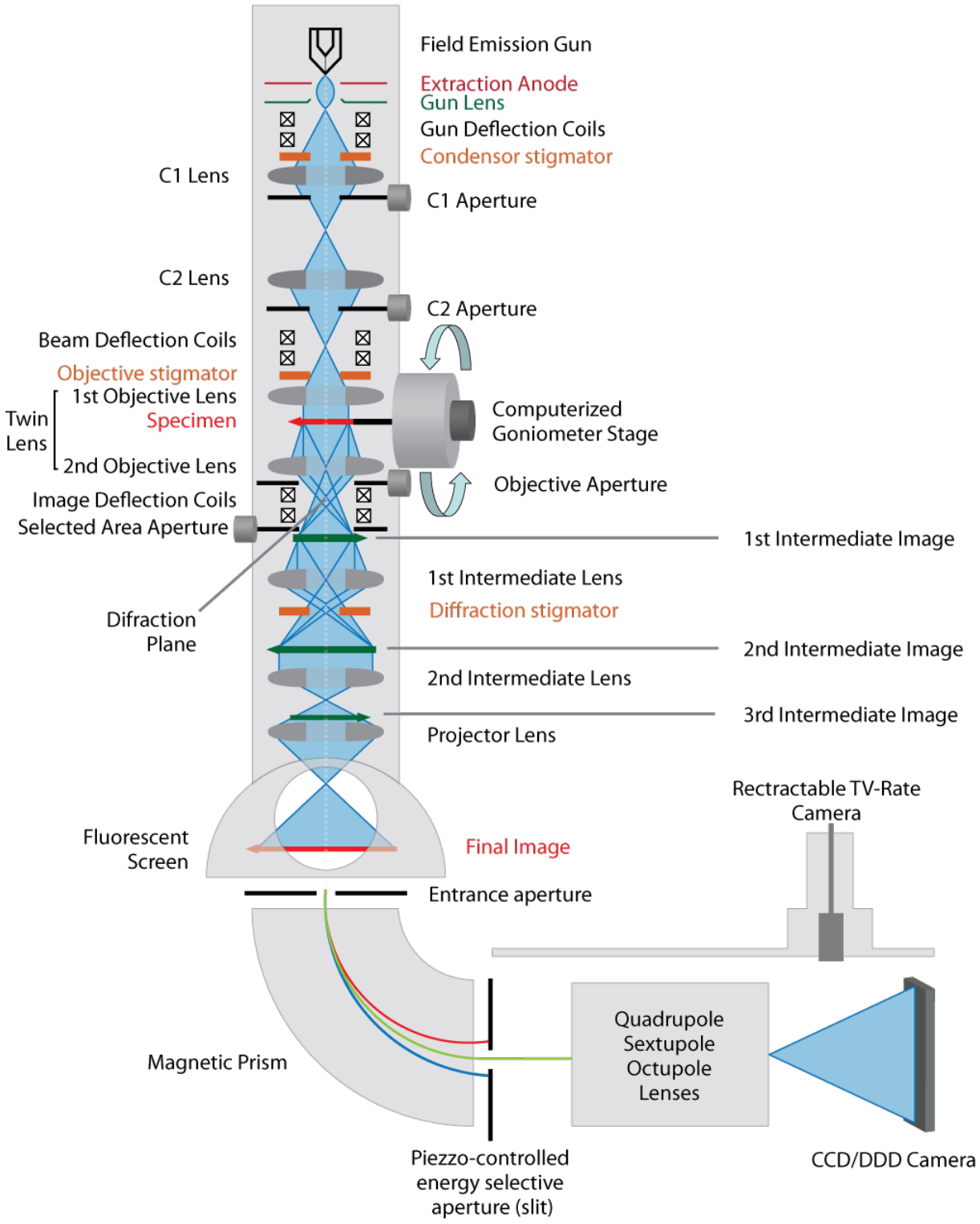

Figure 3: Schematic diagram a typical TEM system used for Cryo-ET in Martinsried.

3.1.1 Essential elements of a modern Transmission Electron Microscope

This section gives a brief overview of the essential elements of a typical modern transmission electron microscope used for Cryo-electron tomography and single particle cryo-electron microscopy (Figure 3).

Electron Gun The electron gun emits and accelerates electrons into the vacuum of the TEM column, producing an electron beam that ideally has a high brightness and high temporal and spatial coherence. The conventional type of electron gun makes use of thermionic emission from a tungsten or lanthanum hexaboride (LaB_6) wire, which is limited in both temporal and spatial coherence by the relatively high energy spread of the emitted electrons and the relatively large source size, respectively. Modern alternatives such as the Schottky emission gun and especially the field emission gun (FEG) produce significantly brighter electron beams, having a greatly reduced energy spread. The exceptionally high coherence (both temporal and spatial) of the FEG, achieved by quantum mechanical tunneling, makes it the best choice for high resolution TEM applications. All six electron microscopes used in the work presented here (please refer to section 7) were equipped with FEGs, capable of accelerating electrons to either 200 keV or 300 keV.

Illumination system The illumination system of modern TEMs usually consists of two condenser lenses ($C1$ and $C2$) and their respective apertures (Figure 3). It is responsible for shaping the electron beam and allows focusing (condensing) it on the specimen. It can produce a specimen illumination that ranges from a uniformly illuminated large specimen area at low magnifications, through a strongly focused smaller specimen area for higher magnifications, to an electron probe of less than a nanometer in diameter for scanning transmission electron microscopy (Reimer and Kohl, 2008). The majority of TEM electron lenses utilise electromagnetic coils to generate a radially symmetric magnetic field emanating from a central gap in the soft iron pole pieces of the lens. This magnetic field acts in a way similar to a convex optical lens, focusing the beam

of electrons at a constant focal length. Deviations from the radial symmetry of the magnetic field induce spherical and chromatic aberration, and cause astigmatism. TEM apertures, which are most commonly annular metallic plates, have the role of restricting the electron beam to electrons that are within a certain fixed distance from the optical axis. Condenser lens $C1$ de-magnifies the gun cross-over and thus controls the physical size of the beam on the specimen, also known as spot size. Condenser lens $C2$ on the other hand controls the convergence of the beam on the specimen (focusing) and the diameter of illumination on the specimen.

Imaging system The imaging system of modern TEMs comprises the objective lens, objective aperture, intermediate and projector lenses. The objective lens is the first TEM image-forming lens. While its magnification is quite modest (20-50 times) it is the most important lens in the electron microscope, since the quality of the first intermediate image it produces determines the overall resolution of the microscope. The resolution-limiting lens aberrations such as the chromatic and spherical aberrations are only of practical importance for the TEM objective lens, since for a magnification M, the angular aperture of the intermediate and projector lenses is decreased as $\alpha = \frac{\alpha_0}{M}$, while the diameter of the spherical aberration disc is proportional to α^3. Therefore even for a modest magnification M of 20-50 times at the first intermediate image produced by the objective lens, the aperture of the following lenses becomes so small that their spherical aberrations can be neglected (Reimer and Kohl, 2008). The objective aperture, located in the back focal plane of the objective lens, determines what portion of the scattered electrons contribute to the image and can improve its contrast by screening out electrons scattered at high angles. Typically two intermediate lenses are positioned between the objective lens and the projector lens, that projects the final image onto the fluorescent screen or detector. These intermediate lenses can be operated in different modes, allowing either an image (image mode) or a diffraction pattern (diffraction mode) to be formed on the camera. They also further magnify the image produced by the objective lens to a wide range of overall magnifications, although typical magnifications used for

this work were in the range of $40000x$ to $84000x$.
Furthermore, pairs of beam deflection coils integrated at different positions in the TEM column are used to either shift or tilt the electron beam in order to bring it on the optical axis or produce a rocking beam, used for focusing at low and medium magnifications (Figure 3). Additionally, stigmator lenses (stigmators) are used to correct the astigmatism of the electron lenses in the TEM column. There are typically three different sets of stigmators in a modern TEM that can control the astigmatism of either the condensor, objective or diffraction lenses (Figure 3).

Computerized Goniometer Stage Modern transmission microscopes are equipped with computerized goniometer stages that allow the precise shifting and tilting of the specimen, usually mounted on a metal grid around 3 mm in diameter. All the microscopes used for this work were equipped with computer controlled LN_2 cryostages capable of tilting the sample up to $\pm$ 70 degrees while keeping it at all times at LN_2 temperatures.

Image Recording and Detection Most TEMs are equipped with a phosphor coated fluorescent screen on which the final image can be projected and directly observed by cathodoluminescence. For a long time after the TEM was invented, images have been recorded on photographic emulsions, which were later replaced by imaging plates (Mori et al., 1988). Characterized by a wide dynamic range, high quantum efficiency and linearity, imaging plates are still in wide use today, but similar to photographic emulsions they demand a considerable amount of post processing and digitization, thus hindering high-throughput and preventing automatic data acquisition. Scintillator coupled Charge Coupled Device (CCD) cameras on the other hand provide an immediate digitization of the acquired image and have proven to be indispensable for electron tomography, which requires automated data acquisition. While CCDs can be used for direct electron detection (Daud et al., 1987; Stearns and Wiedwald, 1989), their prolonged exposure to high energy electrons results in the generation of defects that can lead to their failure

within a short period of time. For TEM applications, electrons are first detected by a thin scintillator which converts them to photons, which are then transported to the CCD array by either fiber optical or lens coupling. Due to scattering events in the scintillator or limitations in its optical coupling to the CCD, the point at which an electron enters the detector appears as a cloud of light at the sensor, resulting in a broad Point Spread Function (PSF), which ultimately leads to limitations in resolution. Most of the data for this work has been collected on TEMs equipped with scintillator coupled CCD cameras (please refer to section 7).

Energy Filter The interaction of the electron beam with relatively thick specimen ($> 200nm$) leads to many inelastic scattering events and the consequent wide energy spread of the scattered electrons, resulting in blurring of the image contrast. An energy filter can be used to filter out the inelastically scattered electrons, which results in a significant noise reduction and an increase in image contrast. One of the most common energy filter types for electron microscopy is a post-column energy filter, attached to the bottom flange of the TEM (Krivanek et al., 1995). It comprises a magnetic prism that disperses the electrons based on their energy, an energy selective slit that allows only electrons of a certain energy (range) to go through, and an electron lens array that reforms the image generated by these electrons on a detector (Figure 3). Both microscopes used for Cryo-ET of synaptosomes for this work were equipped with Gatan^{TM} post-column energy filters operated in "zero-loss" mode (Grimm et al., 1996). While being of little advantage for single particle Cryo-EM, where samples are relatively thin ($< 100nm$), energy filtering is of great importance for electron tomography of relatively thick ($> 200nm$) samples (Lučić et al., 2005).

3.1.2 New developments in Transmission Electron Microscopy

Recent technological developments are changing the field of Transmission Electron Microscopy. Digital cameras capable of direct electron detection, avoiding the need for a scintillator, have become commercially available in the past few years. Furthermore,

phase plates, which partially correct for the effects of the contrast transfer function (see section 3.1.3) are currently under active development.

Direct Detection Devices (DDDs) Very recently, digital cameras capable of directly detecting electrons, while resisting radiation damage caused by the high energy and charge deposition of the electron beam have become commercially available. These cameras are usually based on Active Pixel Sensor (APS) technology (Matsumoto et al., 1985) and unlike a CCD chip, where a readout of the chip requires a pixel-to-pixel charge transfer, each pixel contains a photodetector and an active amplifier that can be read-out individually. DDDs provide a superior quantum efficiency and improved resolution, compared to scintillator coupled CCD cameras, while retaining the convenience and advantages of immediate digital image availability (McMullan et al., 2009). Their high quantum efficiency, which results in an increase in image contrast, allows images to be acquired with a lower electron dose, which is particularly beneficial for Cryo-ET. A small portion of the tomographic data for this work has been collected on a TEM equipped with a DDD (please refer to section 7).

TEM Phase Plates Image contrast in cryo-EM relies heavily on defocus-induced phase contrast (discussed in more detail in section 3.1.3), which also receives a contribution from lens spherical aberration (Scherzer, 1949). This contrast generation mechanism is mathematically described by an oscillating function in Fourier space, also known as the contrast transfer function (CTF), that results in a selective image contrast (discussed in more detail in section 3.1.3). This is evident in the distinct low contrast and high-pass filtered appearance of cryo-EM images of biological samples. These limitations have motivated various attempts to develop more efficient TEM phase contrast methods, mainly based on devices that modulate the phase of the electron wave and are usually positioned in the back focal plane of the TEM objective lens (Danev and Nagayama, 2010). Similar to their counterparts in phase contrast light microscopy, such devices are typically referred to as "phase plates". One of the most common types of

TEM phase plates is the Zernike-type phase plate, consisting of a thin material film ($\sim 30nm$) with a small hole ($\sim 1\mu m$) in the centre (Danev and Nagayama, 2001). A novel type of phase plate has been developed very recently by Dr. Radostin Danev at the Department of Molecular Structural Biology at the Max Planck Institute of Biochemistry in Martinsried. Some data for this work has been obtained at two TEMs equipped with the aforementioned phase plate.

3.1.3 TEM Image formation

The interaction of the electron beam with the sample forms the basis of TEM image formation. Electrons are strongly scattered by atoms due to their electrostatic interactions with both the atomic electrons and nuclei. Electron scattering can be either elastic or inelastic. In elastic scattering only a negligible amount of kinetic energy is transferred from the electron to the sample and the scattered electrons have a rather wide angular distribution. Inelastic scattering, on the other hand, involves a significant loss of kinetic energy and the resulting scattered electrons have a very narrow angular distribution (Figure 4). Elastic scattering is the type of interaction that gives rise to high-resolution information in TEM, since it is an interaction process that is highly localized to the region occupied by the screened Coulomb potential of the atomic nucleus (Spence, 2013). Inelastic scattering is dominated by plasmon and interband excitations, which are less localized and therefore cannot contribute to high-resolution (Reimer and Kohl, 2008).

Due to their narrow angular distribution, most of the inelastically scattered electrons pass through the objective aperture and produce an undesired background noise. This noise can be usually tolerated in thin samples, but as sample thickness increases, it becomes more and more problematic (especially due to multiple scattering events), which requires energy filtering.

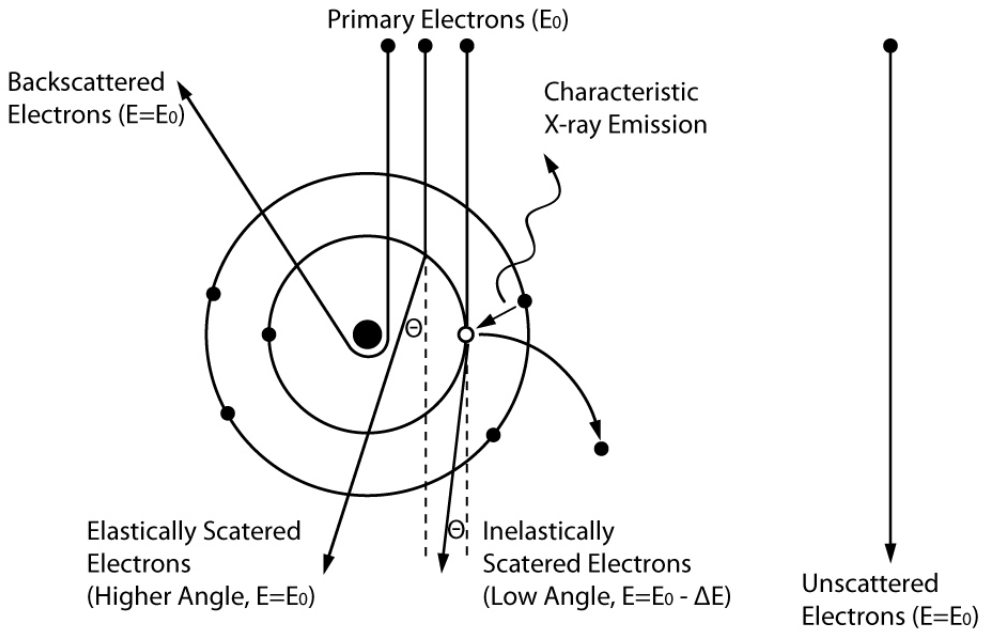

Figure 4: Pictorial description of an electron beam interacting with a carbon atom of the sample.

TEM image contrast (local intensity variations) is formed by two different mechanisms. Phase Contrast arises from complex interference effects resulting from the superposition of the electron waves at the image plane and depends on a number of parameters, including defocus, objective lens spherical aberration, and objective aperture size. Phase contrast is responsible for the majority of image contrast at high TEM resolutions and is the major contrast generating mechanism in Cryo-EM (Dubochet et al., 1988). Amplitude contrast (also referred to as scattering contrast), on the other hand, is caused by the loss of electrons that are scattered at high angles and removed by the objective aperture. These electrons have typically interacted with the high Coulomb potential near the atomic nucleus and their removal by the objective aperture results in a decrease of transmitted intensity. This contrast generating mechanism describes the image intensity at low or medium resolutions, where the phase contrast effects normally dont have to be considered.

Phase Contrast Electrons dont get absorbed by thin Cryo-EM samples, but instead most of them pass through and interact with the sample on the way.

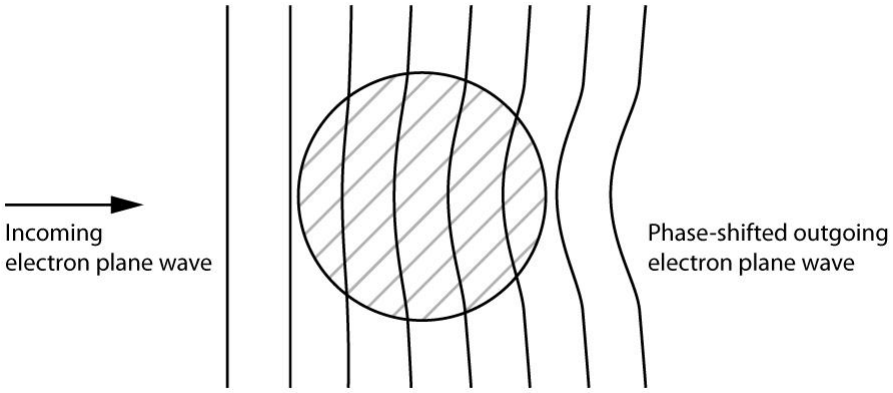

Figure 5: Phase shift of an electron plane wave passing the Coulomb potential of an atom.

Due to the elastic scattering interaction with the sample, the incoming electron wave traveling down the TEM column in the z-direction suffers a phase shift $\Phi(\mathbf{r})$ (Figure 5) given by (Frank, 2006), p.35:

$$\Phi(\mathbf{r}) = \int C(\mathbf{r}, z)dz \tag{1}$$

where $\mathbf{r} = \left[\begin{smallmatrix} x \\ y \end{smallmatrix}\right]$ and $C(\mathbf{r}, z)$ is the Coulomb potential distribution within the sample. The incoming plane wave $\Psi_0 = exp(ikz)$ with wavenumber k is thus modified according to (Frank, 2006), p.35:

$$\Psi(\mathbf{r}) = \Psi_0 \exp[i\Phi(\mathbf{r})] \tag{2}$$

The weak-phase object scattering approximation assumes that $\Phi(\mathbf{r}) \ll 1$, enabling the following expansion (Frank, 2006), p.35, which is normally truncated after the second term:

$$\Psi(\mathbf{r}) = \Psi_0\Big[1 + i\Phi(\mathbf{r}) - \frac{1}{2}\Phi(\mathbf{r})^2 + ...\Big] \tag{3}$$

which suggests that the wave behind the object can be decomposed into an unscattered wave (Ψ_0) and a weak scattered wave of low amplitude ($\Phi(\mathbf{r})$) that has suffered a phase

shift of $\frac{\pi}{2}$ with respect to the unscattered wave. Thus the image intensity is dominated by the interference of the scattered wave with the unscattered wave (known as bright-field electron microscopy). Since the scattered wave is $\frac{\pi}{2}$ out of phase with the unscattered wave, no significant change in the amplitude can be generated by interference and thus the scattered beam gives no contrast for a phase object. Additional phase shift is thus required to produce image contrast. Inherent objective lens aberrations and defocusing can shift the phase of the scattered wave by an amount given by (Frank, 2006), p.36:

$$\gamma(\mathbf{k}) = 2\pi\chi(\mathbf{k}) \tag{4}$$

where $\mathbf{k} = (k_x, k_y)$ is the spatial frequency and the term $\chi(\mathbf{k})$ is known as the wave aberration function. Expressed in polar coordinates with $k = |\mathbf{k}|,\ \phi = a\ \tan(k_x, k_y)$ by (Frank, 2006), p.36:

$$\chi(k, \phi) = -\frac{1}{2}\lambda\Big[\Delta z + \frac{z_a}{2}\sin 2(\phi - \phi_0)\Big]k^2 + \frac{1}{4}\lambda^3 C_s k^4 \tag{5}$$

where Δz is the defocus introduced by the objective lens; C_s, the third-order spherical aberration constant of the objective lens; λ, the electron wavelength; z_a, the focal difference due to axial astigmatism; and ϕ_0, the reference angle defining the azimuthal direction of the axial astigmatism.

According to the Fraunhofer approximation (Goodman 1968 - Intro to fourier Optics) that applies to electron microscopy, the wave function produced at the back focal plane of the objective lens, $\Psi_{bf}(\mathbf{k})$, can be expressed as the Fourier transform ($\mathfrak{F}\{\cdot\}$) of the wave function $\Psi(\mathbf{k})$ directly behind the object. This Fourier transform is multiplied by a term denoting the effect of the phase shift to the scattered wave introduced by the above mentioned objective lens aberrations and defocus, giving (Frank, 2006), p.37:

$$\Psi_{bf}(\mathbf{k}) = \mathfrak{F}\{\Psi(\mathbf{k})\}\exp[i\gamma(\mathbf{k})] \tag{6}$$

The wave function in the TEM image plane, $\psi_i(\mathbf{r})$, can be obtained by an inverse

Fourier transform ($\mathfrak{F}^{-1}\{\cdot\}$) from the wave function produced at the back focal plane of the objective lens that has been additionally modified by an aperture function $A(\mathbf{k})$ introduced by the objective lens aperture, (Frank, 2006), p.38:

$$\psi_i(\mathbf{r}) = \mathfrak{F}^{-1}\{\mathfrak{F}\{\psi'(\mathbf{k})\}A(\mathbf{k})\exp[i\gamma(\mathbf{k})]\} \tag{7}$$

$$A(\mathbf{k}) = \begin{cases} 1 & \text{for } |k| = \theta/\lambda \leq \theta_1/\lambda \\ 0 & \text{elsewhere} \end{cases} \tag{8}$$

where θ_1 is the angle corresponding to the radius of the objective lens aperture. The final observable intensity distribution in the TEM image plane is given by (Frank, 2006), p.38:

$$I(\mathbf{r}) = |\psi_i(\mathbf{r})|^2 \tag{9}$$

Contrast Transfer Function As discussed in the previous section, under the weak phase object approximation one can ignore the higher order terms resulting from multiple scattering events in Equation (3) and if one also assumes that $\Phi(\mathbf{r})$ is real, Equation (9) gives a linear relationship between $\mathfrak{F}\{\Phi(\mathbf{r})\}$ and the Fourier transform of the image contrast $\mathfrak{F}\{I(\mathbf{r})\}$ given by (Frank, 2006), p.39:

$$\mathfrak{F}\{I(\mathbf{r})\} = \mathfrak{F}\{\Phi(\mathbf{r})\}A(\mathbf{k})\sin\gamma(\mathbf{k}) \tag{10}$$

The function $\sin\gamma(\mathbf{k})$ (Figure 6) is known as the defocus phase-contrast transfer function (CTF). Due to its oscillatory nature, the CTF creates regions in the spatial frequency spectrum that strongly differ in the transmitted image intensity, resulting in a selective image contrast that allows only certain regions of the spectrum to be imaged adequately, while in other regions image contrast is diminished or inverted. The defocus Δz is virtually the only parameter that one can control in order to select the desired regions of the object's Fourier Spectrum that are properly transmitted. Equation (10) assumes an ideal situation where the illumination is highly coherent and monochromatic, which

in practice is not the case. The partial coherence and energy spread have the effect of dampening the CTF at higher spatial frequencies (Figure 6), posing a limitation on the achievable resolution. An additional term can be incorporated into Equation (10) in order to account for this dampening:

$$\mathfrak{F}\{I(\mathbf{r})\} = \mathfrak{F}\{\Phi(\mathbf{r})\}E(\mathbf{k})A(\mathbf{k})\sin\gamma(\mathbf{k}) \tag{11}$$

where $E(\mathbf{k}) = E_i(\mathbf{k})E_e(\mathbf{k})$ is referred to as the compound envelope function and the terms $E_i(\mathbf{k})$ and $E_e(\mathbf{k})$ account for partial coherence and energy spread respectively. The exceptionally high coherence (both temporal and spatial) of FEGs compared to LaB_6 thermionic emission guns significantly improves the dampening caused by the envelope function (Figure 6) and allows much higher spatial frequencies to be transmitted (Zhou and Chiu, 1993). The CTF tends to act both as a low- and high-pass filter, resulting in a general band-pass filtering effect. Its high-pass filtering effect is a consequence of its relatively low values for an extended range of low spatial frequencies. Its low-pass filtering property, on the other hand, results from the fact that for typical underfocus values, it is effectively equal to 0 around the first zero crossing and oscillates rapidly at higher spatial frequencies (Figure 6).

Amplitude Contrast Even though biological Cryo-EM samples predominantly consist of light atoms, the Coulomb potential near the nucleus is very high, causing some electrons to be scattered at high angles and removed by the objective aperture, giving rise to amplitude contrast. Equation (10) only accounts for the the phase contrast component of the imaged object. Unlike the its phase contrast counterpart, the Fourier transform of the amplitude contrast component is transferred by $\cos\gamma(\mathbf{k})$. The complete expression accounting for both phase and amplitude contrast is therefore given by (Frank, 2006), p.47:

$$\mathfrak{F}\{I(\mathbf{r})\} = O_r(\mathbf{k})\sin\gamma(\mathbf{k}) - O_i(\mathbf{k})\cos\gamma(\mathbf{k}) \tag{12}$$

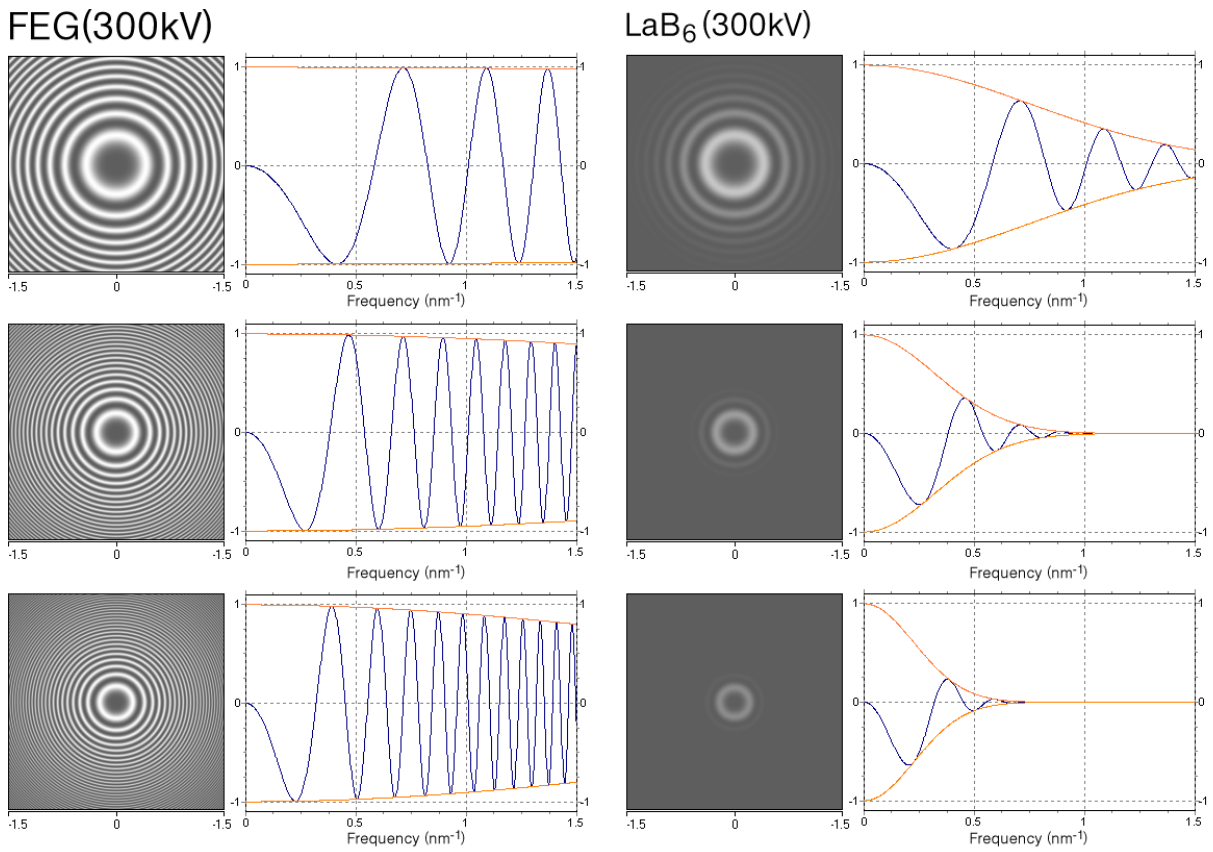

Figure 6: Theoretical Contrast Transfer Functions (CTFs) (blue) and their envelopes (orange) for a FEG (left column) and LaB_6 (right column) TEMs operated at 300kV for defocus values of -1.5 μm (first row), -3.5 μm (second row) and -5 μm (third row). The higher spatial coherence (illumination aperture =0.02 mrad and =0.2 mrad for FEG and LaB_6, respectively) and improved temporal coherence (energy width of the incident beam E=0.7 eV and E=3 eV for FEG and LaB_6, respectively) of TEMs equipped with a FEG lead to smaller attenuation of the CTF.

where $O_r(\mathbf{k})$ and $O_i(\mathbf{k})$ are the Fourier transforms of the phase and amplitude contrast components of the object, respectively (Erickson and Klug, 1970). The percentage of amplitude contrast is intuitively higher for heavier atoms, reaching values of up to 35% in negatively stained samples (Erickson and Klug, 1970), while being usually between 5% and 7% for Cryo-EM samples (Baker and Henderson, 2012).

CTF correction The recovery of higher resolution information beyond the first zero crossing of the CTF requires some form of computational signal restoration generally

know as CTF correction. The most general type of CTF correction, generally known as phase flipping (Typke et al., 1992), consists of inverting the signs of certain CTF regions (equivalent to a 180° phase shift) so that all Fourier components are transferred with the same sign, resulting in a continuous contrast transfer (either negative or positive). While this type of restoration solves the problem of contrast inversions throughout the spatial frequency domain, it still leaves the frequency dependent amplitude attenuation of the CTF unresolved. More elaborate restoration methods, such as the Wiener filter (Wiener, 1949) attempt to correct both the sign and the magnitude of the CTF amplitude, but are bound to limitations mainly imposed by the effects of the envelope function and the presence of noise (Downing and Glaeser, 2008). A solution to dealing with the missing (zeroes of the CTF) or suppressed (near zeroes of the CTF) image information in single particle analysis is to collect images at a series of defocus values in order to "fill" the missing information in Fourier space (Frank and Penczek, 1995; Penczek et al., 1997).

3.2 Sample preparation

Biological samples have to be placed in the TEM column and observed in the vacuum, which imposes certain requirements on sample preparation methods. Additionally, the contrast produced by biological molecules alone is low, which in the past has led to the development of diverse contrasting methods, such as staining by heavy metal salts (e.g. uranyl acetate) (Brenner and Horne, 1959). Heavy metals can surround the molecules of the specimen and also penetrate into some of their hydrophilic regions to replace water. The stain produces strong contrast and can sustain a higher degree of radiation resistance than the sample, but since it usually only surrounds the molecules (negative staining), the molecular surface contour alone is imaged and therefore only its shape can be reconstructed. Negative staining can directly be applied to samples of macromolecules and viruses up to a certain size. Cells and tissues, usually need to be thinned before imaging in EM. For that reason they are chemically fixed, dehydrated, embedded in plastic and sectioned before staining. These are harsh procedures that may introduce

a number of structural artifacts and often lead to the structural collapse and deformation of the sample (Hayat and Miller, 1990), making the interpretation of its three dimensional structure highly doubtful (Frank, 2006).

The development of methods for the embedment of biological samples in vitreous ice that closely resembles their native aqueous environment was a pivotal point in biological electron microscopy (Taylor and Glaeser, 1976; Dubochet et al., 1982). It provided an unprecedented level of biological structural preservation and since no heavy metal staining is used, it allowed for the first time the direct visualization of biological material at molecular resolution (Lučić et al., 2005). In this technique, the samples are rapidly frozen (typically cooling speeds of $10^5\,^{\circ}\mathrm{C}s^{-1}$ are reached) to temperatures below the point where water forms ice crystals (below 140C), resulting in a solid, crystal-free state of water (vitreous ice) that maintains its natural distribution. Therefore, samples are imaged in a fully hydrated state. Plunge freezing is the common type of preparation method for relatively thin biological samples ($20\mu m$ or thinner) and consists of plunging the specimen embedded in a thin film of aqueous solution on an EM grid, into a cryogen (a liquid with good heat-transfer characteristics, e.g. ethane or propane) (Vanhecke et al., 2011). While unstained, vitrified biological samples provide the best known structural preservation for EM, they are sensitive to the electron irradiation and generally have low contrast and signal-to-noise ratio (SNR).

3.3 Cryo-electron tomography

Cryo-electron tomography (Cryo-ET) enables the three-dimensional visualization of frozen hydrated biological samples at molecular resolution. During the tomographic image acquisition, the sample is rotated inside the TEM column by a computer-controlled specimen stage and a set of electron micrographs (tilt series) is recorded at the different angular orientations (Figure 7 left). The collected micrographs can be regarded as projections through the sample (Koster et al., 1997), which can be aligned and compu-

tationally merged into a 3D reconstruction (tomogram).

Johann Radon's work laid the foundations for the reconstruction of a function from a set of projections (Radon, 1917). The basic principle of 3D reconstruction from electron micrographs was introduced in the late 1960s (De Rosier and Klug, 1968), followed shortly after by the first 3D reconstruction from tilt series (Hoppe et al., 1974). Already in 1968, electron tomography of unstained biological samples has been proposed (Hart, 1968), although it didn't get much attention at the time.

Electron tomography gained a momentum with the introduction of computer controlled-microscopes equipped with CCD cameras, which enabled the automation of tomographic data acquisition (Typke et al., 1991; Koster et al., 1992). This solved problems associated with the cumbersome manual data collection and most importantly, allowed keeping the total electron dose within acceptable limits. Soon after, automated tomography in "low-dose mode" has been successfully applied to samples of vitrified biological samples (Dierksen et al., 1995; Grimm et al., 1997), paving the way for Cryo-ET as it is known today.

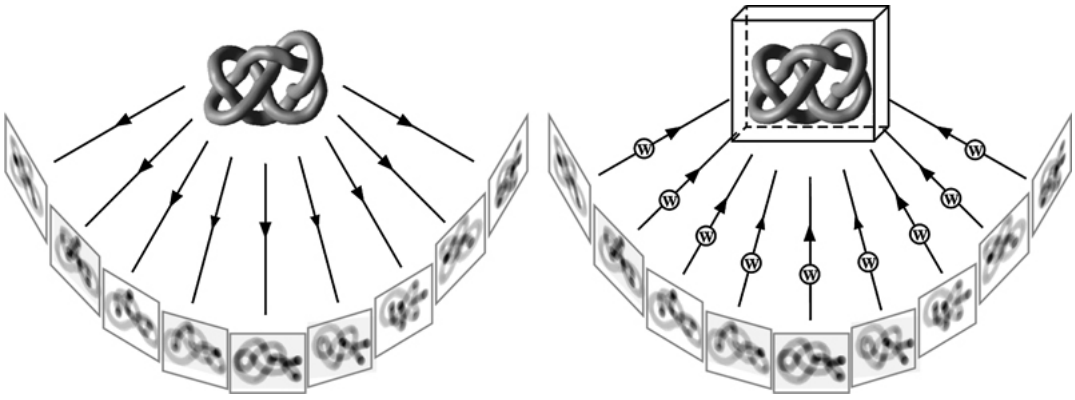

Figure 7: Principle of electron tomography. (left pannel) Projections of the specimen are recorded from different directions by tilting the specimen holder. (right pannel) A three-dimensional reconstruction of the sample is obtained by backprojection (adapted from (Lučić et al., 2005))

3.3.1 Data acquisition

Due to the high electron beam sensitivity of frozen-hydrated biological samples, tomographic data acquisition requires strict low-dose imaging conditions that are not feasible with manual data acquisition. The automation of tomographic data acquisition made it possible to acquire a tilt series under low-dose conditions, while keeping the sample within the field of view and at a constant level of defocus. The low-dose automated tilt series acquisition consists of three basic steps (Koster et al., 1992; Dierksen et al., 1992): tracking, autofocusing, and exposure. The purpose of the automated tracking step is to keep the object of interest in the field of view. In order to achieve that, any changes in the lateral displacement of the sample in relation to the previous tilt angle, typically a result of mechanical inaccuracies of the specimen stage, need to be determined. Usually a very low dose micrograph is recorded and compared by cross-correlation to one taken at a previous tilt angle and lateral displacements are compensated by introducing an image shift. The autofocusing step ensures that a constant level of defocus is present at each tilt angle by compensating for any sample movement in the beam direction. This is usually achieved by comparing micrographs acquired at different beam tilts to determine the actual defocus (Koster et al., 1989; Ziese et al., 2003). In order to keep the electron dose received by the object of interest to a minimum, tracking and focusing are usually performed at positions shifted a few micrometers along the tilt axis in respect to the exposure location. Finally, the exposure step is the actual recording of the projection.

3.3.2 Tilt Series Alignment and Reconstruction

First, the images comprising a tilt series are precisely aligned to a common coordinate system. The alignment procedure determines, among others, the tilt axis angle and the lateral shifts of the projections with respect to a reference projection that arise from the limited accuracy of the tracking procedure. The most widely used type of alignment methods are based on fiducial markers (typically colloidal gold that is added to the sample). The marker coordinates on each projection can be determined either manu-

ally or automatically (Amat et al., 2008), and an alignment model can be calculated using least-squares methods that aim to minimize the alignment error as a function of the tilt axis angle and lateral translations (Frank, 2008). Fiducial-less alignment methods based on cross correlation (Guckenberger, 1982) or the common lines algorithm (Liu et al., 1995) are not routinely used for Cryo-ET due to their high degree of noise sensitivity. After alignment, a three-dimensional reconstruction can be calculated from the projections by either real- or Fourier-based reconstruction methods. Real-space-based reconstruction methods are the most commonly used ones (Hawkes, 1980). Weighted backprojection (WBP) is one of the most popular reconstruction method used in Cryo-ET (Rademacher, 1992). In WBP the projections are simply projected back to form a three-dimensional reconstruction (Figure 7 right). Due to uneven sampling in Fourier space, resulting in an enhancement of low frequencies, a weighting function has to be applied to the projections before backprojection in order to ensure an accurate reconstruction. There are generally two types of weighting functions that are routinely applied: exact and analytical. Exact weighting functions use the physical size of the object of interest to be reconstructed to determine the sampling density in Fourier space (Harauz and van Heel, 1986). Analytical weighting functions, on the other hand, apply a weighting proportional to the frequency in the direction perpendicular to the tilt axis.

3.3.3 Angular sampling and tilting strategies

The Fourier space description helps to explain the rationale behind recovering three-dimensional information from the two-dimensional projections of an object. According to the projection slice theorem, the Fourier transformation of a projection of the tilt series corresponds to a central section in the three-dimensional Fourier transform of the imaged object (Figure 8). For an object with thickness d the thickness of this central section is given by $\frac{1}{d}$ and according to the Crowther criterion, the attainable resolution of a tomogram r in the direction of the electron beam is given by:

$$r = \frac{\pi d}{N} \tag{13}$$

where N is the number of equally-spaced projections in a tilt series (Crowther et al., 1970b). Therefore, in order to properly sample the imaged object in three-dimensional Fourier space one needs to acquire a large number of projection images (smaller angular increments) distributed over a wide angular range. At the same time the total electron dose accumulated in the sample during tilt series acquisition has to be kept within acceptable limits. The "dose-fractionation theorem" (Hegerl and Hoppe, 1976; McEwen et al., 1995) provides a solution to these contradicting requirements by suggesting that each voxel in a 3D reconstruction has the same variance as a 2D image of that same voxel taken at the same total electron dose. Thus, theoretically one may fractionate the total electron dose over many noisy projections, combine the them into a 3D reconstruction and obtain a separation of the object features in the direction of the electron beam at no extra cost. The only practical limitation is that each image has to have a sufficient signal-to-noise ratio to allow for accurate alignment.

Although the Crowther criterion is an important measure in the interpretation of tomograms, it assumes that the sample thickness is independent of the tilt angle (i.e. spherical or cylindrical sample geometry is assumed) and that the sample can be fully tilted to $\pm 90°$. In practice most samples in electron microscopy have a limited thickness in the electron beam direction and are quite extended in the x- and y-directions (i.e. slab geometry). Furthermore, The tilt range in Cryo-ET is usually limited to $\pm 70°$ due to the design of the specimen holder, resulting in a wedge-shaped region of missing information in 3D Fourier space, also known as the missing wedge. For the optimal sampling of a slab-type sample geometry, non-equidistant tilting schemes, employing smaller tilt increments at higher tilt angles, have been proposed (Saxton et al., 1984). These are however rarely used, since their benefits are outweighed by the fact that a big portion of the total electron dose is spent on acquiring projections at high tilt angles

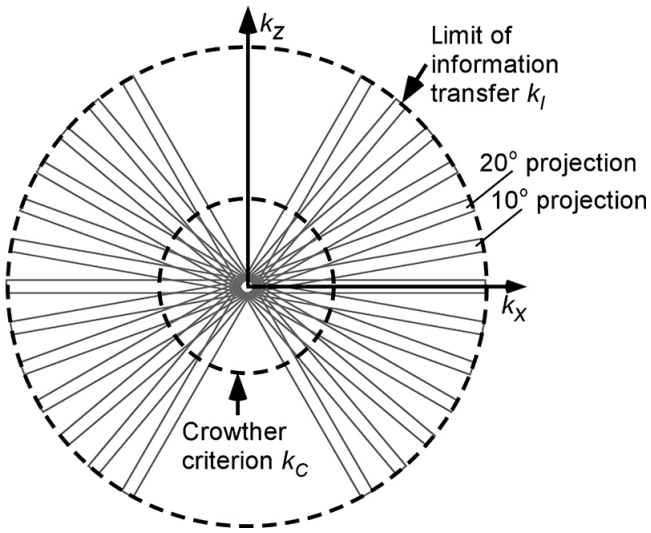

Figure 8: Data sampling in Fourier space. The projection of an object with thickness d corresponds to a central slice of thickness $\frac{1}{d}$ in Fourier space. The three-dimensional information of the specimen (outside of the missing wedge) is therefore gathered homogeneously up to frequency k_c (Crowther criterion) (adapted from (Lučić et al., 2005))

that generally have a very low signal to noise ratio (Mastronarde, 1997). The missing wedge in 3D fourier space introduces elongation in the direction of the electron beam in the 3D reconstruction, which makes the resolution non-isotropic. As a result, certain objects appear elongated in the direction of the electron beam, while others are hardly resolved, depending on their orientation with respect to the tilt axis (Figure 9, left). These limitations have motivated the development of dual-axis tilt series acquisition schemes (Mastronarde, 1997; Penczek et al., 1995) where an additional tilt series is collected after rotating the sample by 90° around the optical axis. This reduces the missing information in fourier space to a pyramid-shaped region and makes the achievable resolution more isotropic (Figure 9, right).

In addition to the factors mentioned above, the resolution in Cryo-ET is further limited by sample radiation damage, that could potentially result in inconsistencies in the projections, and noise. Moreover, inaccuracies in the alignment of the tilt series before reconstruction, additionally contribute to reduction in resolution. Although different

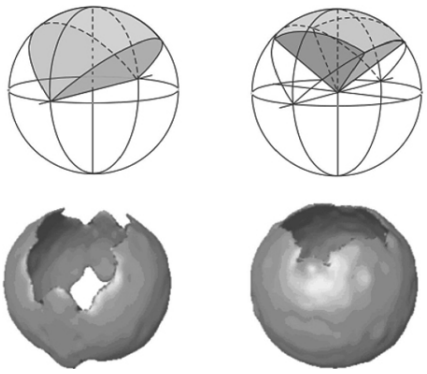

Tilt range	Single	Double
±70°	78%	93%
±60°	67%	84%
±45°	50%	67%

Figure 9: Single- vs. double-axis tilting. The upper illustrations show schematically the regions in Fourier space that remain unsampled because of the limited tilt range. In single-axis tilting (left), there is a "missing wedge", in double-axis tilting (right), a "missing pyramid". The table contains percentages of the Fourier space that are covered for different tilting schemes. The missing information in real space is illustrated below (adapted from (Lučić et al., 2005))

resolution estimates have been proposed (Cardone et al., 2005; Penczek, 2002; Unser et al., 2005), no straightforward validation of the resolution in Cryo-ET is available.

3.3.4 Image Analysis

The large number of structures observed in cryo-tomograms of cells and cellular compartments requires the separation and extraction of the features of interest from the background. This process is generally known as segmentation. While manual segmentation is still widely used in electron tomography, it is prone to errors due to user bias and it is usually characterized by non-reproducibility. Automatic segmentation, on the other hand, is more objective, produces reproducible results and generally performs well when the image complexity is low (Fernandez-Busnadiego et al., 2010; Frangakis and Hegerl, 2002). Due to the very low SNR of cryo-electron tomograms, data denoising and enhancement is often a critical step prior to segmentation. A number of denoising algorithms that aim at increasing the SNR and at enhancing the features of interest in the tomograms have been developed (Frangakis and Forster, 2004). The simples denoising algorithms are usually linear filters and remove the noise as well as the signal. Non-linear filtering algorithms, on the other hand, tend to reduce the noise while pre-

serving the features. Examples of such algorithms are nonlinear anisotropic diffusion (NAD) (Frangakis and Hegerl, 2001; Fernandez and Li, 2003), bilateral filtering (Jiang et al., 2003) and non-local means (Darbon et al., 2008). NAD is especially useful for the visualization of ultrastructural features since it has the potential to enhance features such as filaments and membranes.

3.3.5 Template matching

The visual identification of structures in cryo-tomograms is usually limited to large features that can be easily recognized, such as membranes, cytoskeletal elements, organelles and large molecular complexes such as ribosomes. Furthermore, denoising often removes high-resolution features, which might result in the concealment of particular molecular structures. However, direct visualization is not the only way to identify molecular structures in Cryo-ET. Macromolecular complexes can be detected in tomograms computationally by searching for a reference structure (template) that represents the structure of interest (Figure 10). The templates are usually generated from higher res-

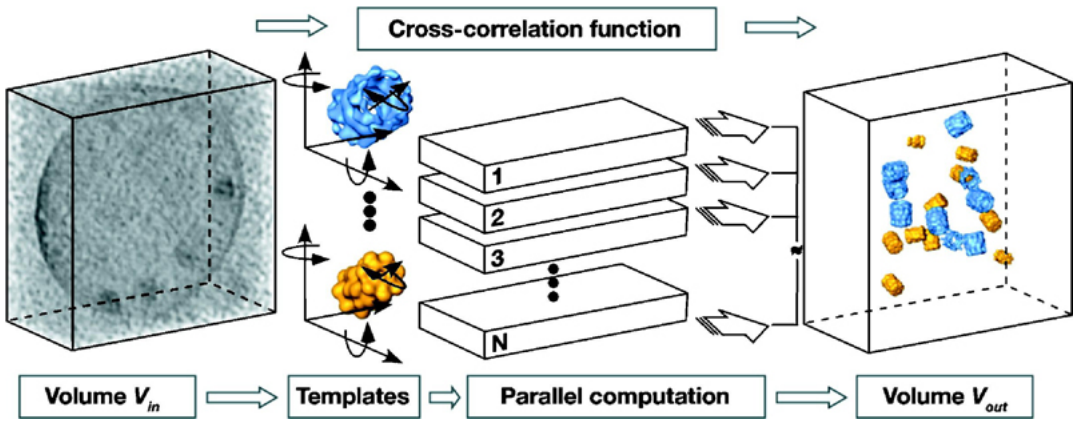

Figure 10: Identification of individual macromolecules in tomographic volumes, based on their structural features. The template-matching approach uses known structures (e.g., obtained from X-ray crystallography or NMR) to search the entire volume of the tomogram systematically for matching patterns by a cross-correlation approach. The search procedure is parallelized to make it computationally feasible (adapted from (Frangakis et al., 2002))

olution structures obtained by single-particle cryo-EM, X-ray crystallography or NMR.

The detection approach most commonly used in Cryo-ET is known as template matching and is basically an adaptation of an earlier algorithm (Roseman, 2000) modified to account for the effects of the missing wedge (Frangakis et al., 2002) and applied to Cryo-ET (Frangakis et al., 2002; Rath et al., 2003). It was shown that template matching is suitable for the identification of macromolecular complexes ranging in size from 500 kDa to 1 MDa with high fidelity (Förster et al., 2005). In addition to location, it can also determine the orientation of target structures.

3.3.6 Subtomogram averaging

Due to the low SNR of cryo-electron tomograms and the effect of the missing wedge, individual macromolecules in a tomogram carry limited information. A structure with a higher resolution can be obtained by averaging 3D volumes containing copies of the same macromolecule extracted from a tomogram (sub-tomograms). Iterative algorithms, similar to the ones used in single-particle cryo-EM, are used for aligning the subtomograms of the randomly oriented copies of the macromolecule and generating an improved structure by averaging (Walz et al., 1997). Medium resolution structures (2-3 nm) of macromolecules obtained by subtomogram averaging can serve as starting models in single-particle cryo-EM (Walz et al., 1997).

3.4 Single-particle cryo-EM

Single-particle cryo-EM is a technique that allows the 3D reconstruction of a structure (typically a macromolecular assembly or a virus) from 2D projection images obtained from a large number of identical copies of the structure at different orientations.

Radiation damage is even more of a concern in single-particle cryo-EM than in Cryo-ET, since one typically aims at obtaining higher-resolved 3D reconstructions. Therefore, in order to minimize radiation damage, the total electron doses are generally kept in the range of 20-30 electrons per $Å^2$.

After micrograph collection, useable images are typically identified by visual inspection and subjected to CTF correction. Individual particles are selected (usually from CTF corrected micrographs) either manually or automatically, with the use of specially designed algorithms (Hohn et al., 2007; Tang et al., 2007).

Once images of individual particles are available they can be classified in 2D according to their structural features using statistical methods, such as principle component analysis (PCA) or multivariate analysis (MVA). Taking advantage of the fact that the noise in the micrographs is predominantly randomly distributed, while the structural features of the particle constant, images belonging to the same class can be averaged to reinforce these structural features. These 2D class averages represent views of the particle in different directions and have an increased SNR compared to the images of the individual particles that comprise them (Figure 11). This classification process is usually iterated using the newly generated class averages as alignment references, which significantly improves the alignment accuracy and allows finer structural details to be resolved.

Just like in Cryo-ET (3.3), the generation of a 3D reconstruction from 2D projection views of the object in single-particle cryo-EM takes advantage of the projection slice theorem (3.3.3). However, unlike in Cryo-ET, the relative orientations of the particles in the projections are not known a priori and need to be determined.

A low resolution 3D model may already be available (from tomography or a similar, already solved structure) and used as an initial 3D reference model. Alternatively, an initial 3D model can be obtained from 2D class averages. The approach typically taken in single-particle cryo-EM to address this problem relies on the fact that the Fourier transforms of any two different projections of the same 3D object share a common line where they intersect in 3D Fourier space. The relative orientations of the particles can

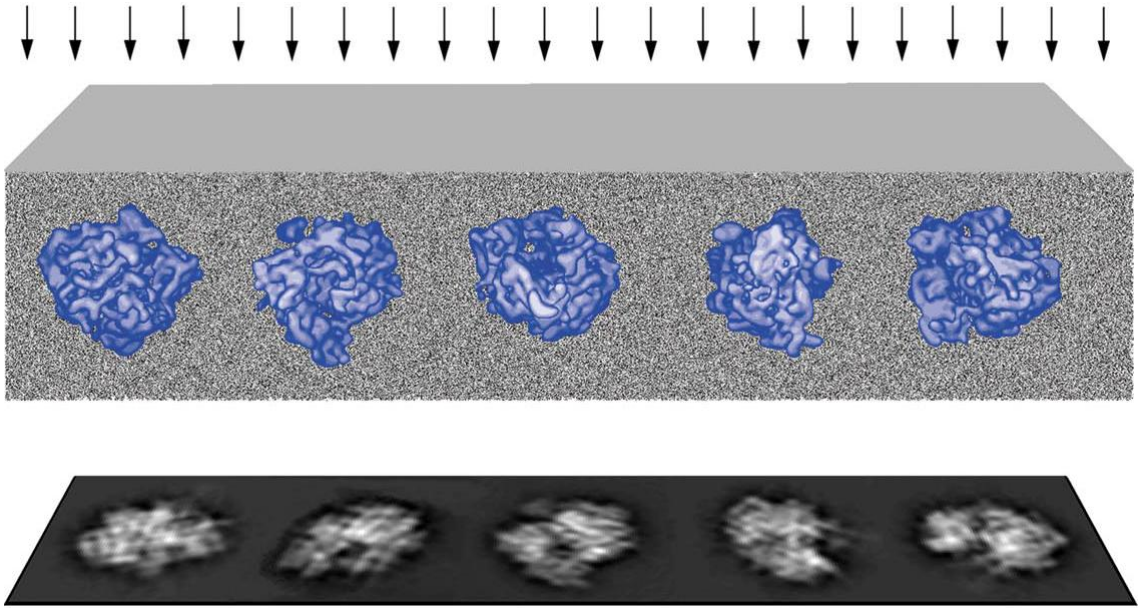

Figure 11: Single-particle cryo-EM data collection schematic. Arrows represent the incident electron beam. Multiple copies of identical molecules are lying in random orientations in a thin layer of vitreous ice. Parallel projections of the particles are obtained at high magnification in the image plane. Projections of particles lying in the same orientation can be found by employing alignment and classification procedures. Adapted from (Frank, 2002)

therefore be determined by identifying such common lines between class averages, which can be done either in Real (Van Heel, 1987) or Fourier space (Crowther et al., 1970a). However, the handedness of the structure can not be determined by this approach and requires some sort of a tilt experiment (e.g. Cryo-ET). The initial model is refined to a higher resolution by projection-matching techniques (Harauz and Ottensmeyer, 1984; Penczek et al., 1994). This is an iterative method where at each iteration the particles are compared with projections of the current model in order to improve their alignment. The new alignment parameters are then used to obtain a refined 3D model.

In case not all particle orientations are well represented in the dataset, a region in Fourier space will be missing and, similar to Cryo-ET, the 3D reconstruction will typically show elongation of features in the direction of the missing angular range (Frank 2002).

A number of software packages implementing the image processing strategies for for single-particle EM analysis outlined above, as well as additional image processing capabilities, have been developed throughout the years, such as EMAN2 (Tang et al., 2007), RELION (Scheres, 2012), XMIPP (Sorzano et al., 2004), SPARX (Hohn et al., 2007) and SPIDER (Shaikh et al., 2008).

Many macromolecules exist in multiple conformations in solution, due to their inherent structural flexibility. In order to obtain 3D reconstructions of different conformations present in the same sample by single particle analysis, it is required that different conformations can be separated and reconstructed separately. While this has been a challenge in the field for a long time, more recently advanced classification techniques have been developed, capable of achieving that task (Scheres et al., 2007; Fischer et al., 2010). The RELION software package (Scheres, 2012) implements a powerful method for classification of single-particle cryo-EM data in 3D based on Maximum Likelihood, that has been used in this work.

Although different resolution measures have been developed in the field of single-particle cryo-EM throughout the years (Penczek, 2010), the Fourier shell correlation (FSC) (Saxton and Baumeister, 1982) is currently the only one in widespread use. It is a function of spatial frequency that measures the normalized cross-correlation coefficients computed between the Fourier transforms of two 3D volumes over shells of equal spatial frequencies in Fourier space and is given by:

$$FSC_{1,2}(r) = \frac{\sum\limits_{r_i \epsilon r} F_1(r_i) \cdot F_2(r_i)^*}{\sqrt{\sum\limits_{r_i \epsilon r} |F_1(r_i)|^2 \cdot \sum\limits_{r_i \epsilon r} |F_2(r_i)|^2}} \tag{14}$$

where r is the radius of the corresponding shell in Fourier space, $F(r_i)$ is the complex structure factor at voxel r_i in Fourier space and $\sum_{r_i \epsilon r}$ is the sum over all Fourier space voxels r_i at radius r. In case 2D projections are compared instead of 3D volumes, the

measure is referred to as Fourier Ring Correlation (FRC).

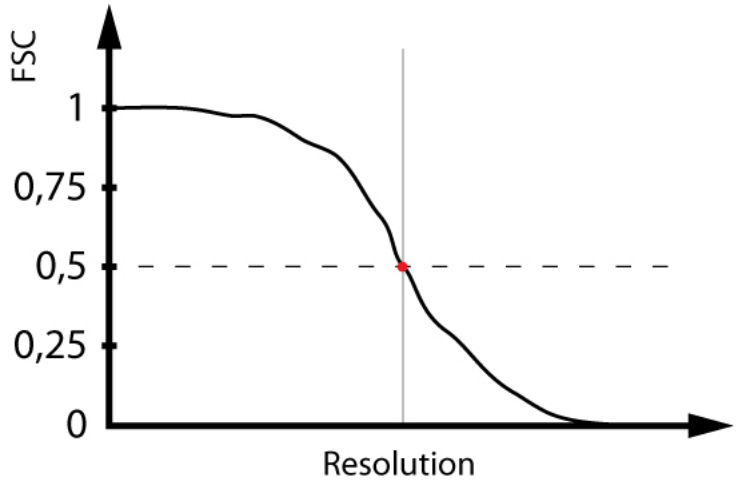

Figure 12: Fourier Shell Correlation (FSC) curve showing resolution as determined by the 0.5 cutoff criterion.

The two 3D volumes that are compared are typically obtained from splitting the dataset into two halves and reconstructing them separately. Most commonly, these half datasets are constructed by splitting the particle images into even and odd, thus this technique is commonly referred to as even-odd test. There are several schools of thought regarding the interpretation of the resolution determined by FSC (van Heel and Schatz, 2005), but most of the time the so-called 0.5 resolution cutoff (i.e. when the correlation coefficient is equal to 0.5) is used (Figure 12) to determine the resolution (Frank, 2006).

4 Aim of this work

One of the aims of this work was to study the native, three-dimensional supramolecular architecture of the PSD by Cryo-electron tomography. To this end, PSD was imaged enclosed within the postsynaptic terminals of synaptosomes, as well as isolated in the PSD fraction. Furthermore, in order to study functional aspects of the PSD structure, PSD of non-stimulated and stimulated synapses were imaged and analyzed.

Another aim was to detect CaMKII, a major postsynaptic protein and key regulator of longterm potentiation (LTP), in these tomograms by template matching. Since a number of structural studies have previously produced highly diverging views of the CaMKII holoenzyme structure and because no structure existed for the activated state of CaMKII, an additional aim of this work was to obtain the structures of both activated and non-active CaMKII by Cryo-EM single particle analysis.

The specific objectives of the study were:

- To analyse the native three-dimensional structure of the postsynaptic density by cryo-electron tomography in resting synapses and synapses stimulated pharmacologically in order to induce rearrangements in their structure.
- To detect CaMKII in its different activation states by template matching in cryo-tomograms of resting synapses and synapses treated pharmacologically in order to induce rearrangements in their structure.
- To determine the structures of both activated and non-activated recombinant mouse CaMKIIα homomultimers by single particle analysis and single particle tomography.

5 Results

This section is organized in two parts. The first part describes the results of cryo-electron tomography of synapses from untreated and pharmacologically treated synaptosomes along with the results of cryo-electron tomography of isolated postsynaptic densities from such synapses. In addition this part describes template matching using models of the CaMKII holoenzyme in its different activation states. The second part focuses on obtaining the structures of both activated and non-activated recombinant mouse CaMKII homomultimers by single particle analysis and single particle tomography.

5.1 The postsynaptic architecture studied by Cryo-ET

The postsynaptic architecture was studied in synapses from rat cerebrocortical synaptosomal fraction as well as in postsynaptic densities isolated from this fraction by utilizing their insolubility in nonionic detergents. The cerebrocortical synaptosomal fraction contains synapses derived from pinched-off nerve terminals held together by the cell adhesion molecules of the synaptic cleft. These detached synapses (synaptosomes) retain most of the biochemical and structural properties of the nerve terminals from which they are derived (Whittaker, 1984). For example, synaptosomes are capable of multiple cycles of neurotransmitter release upon depolarization and are highly amenable to pharmacological manipulations (Whittaker, 1993).

Synaptosomes for this work were prepared using a Percoll gradient procedure shown previously to yield viable synapses (Dunkley et al., 1988), ideal for Cryo-ET examination (Fernandez-Busnadiego et al., 2010). Special attention was given to the rapid homogenization of the brain tissue after decapitation, since previously it has been shown that CaMKII accumulates at the PSD in a time-dependent manner in the minutes after

decapitation (Suzuki et al., 1994).

Vitrified synaptosomes frequently formed thick (> 1 μm) aggregates on the EM grid with the size of these aggregates largely dependent on synaptosomal concentration at the time of plunge freezing. The ideal concentration for plunge freezing was found to be between 0.5 and 0.7 mg/ml of protein. At this concentration synaptosomes still aggregated, but formed smaller aggregates with some thinner areas (< 0.5 μm) in their periphery amenable to Cryo-ET. In addition, thin areas (< 0.5 μm), containing only a few isolated synaptosomes within the holes of the Quantifoil carbon film were often found (Figure 13, A).

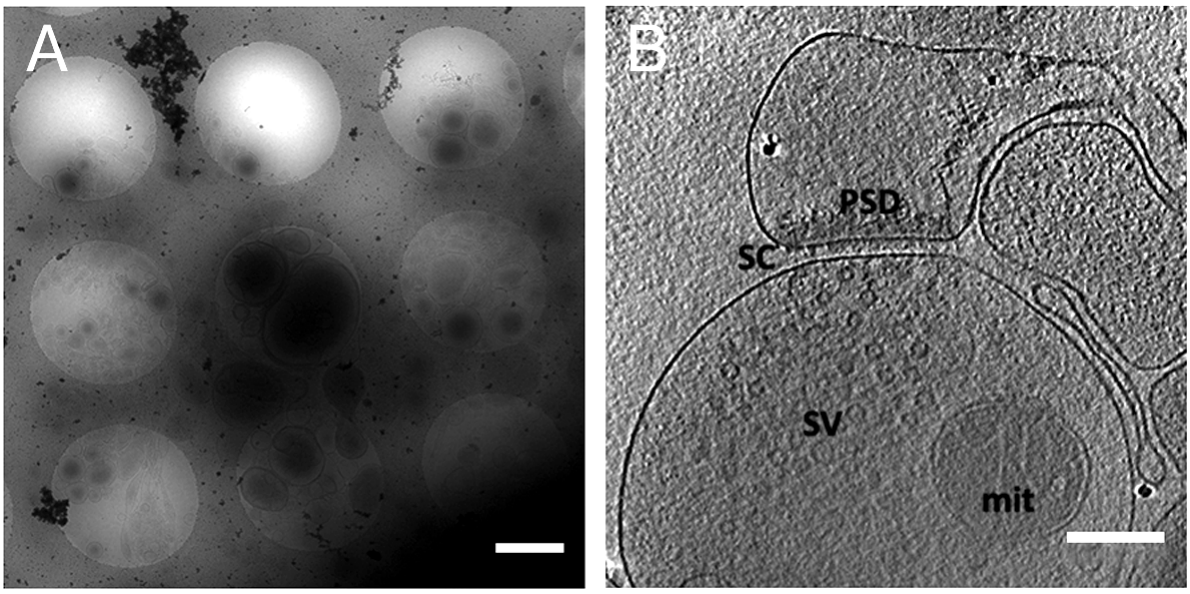

Figure 13: Images of synaptosomes at different magnifications. (A) Overview of synaptosomes on an EM grid. (B) 3.2 nm-thick tomographic slice. Synaptic vesicles (SV), postsynaptic density (PSD), synaptic cleft (SC), mitochondrion (mit). Scale bars: (A) 1000 nm, (B) 200 nm.

Most of the observed structures consisted of sealed presynaptic nerve terminals lacking an adhering postsynaptic terminal. In cases when an attached postsynaptic density was present, some of these postsynaptic densities were found within sealed membranes.

Other structures that could be observed in the synaptosomal fraction included isolated mitochondria, myelin, membranes (both sealed and unsealed) and isolated synaptic vesicles. The synapses selected for tomography were identified by the presence of a vesicle-filled, sealed presynaptic nerve terminal adhering to a sealed postsynaptic terminal, containing a prominent postsynaptic density, and a regular spacing ($\sim$25 nm) between the terminals (synaptic cleft). Such synapses made up only a small fraction of the synaptosomes on the grid and in addition they had to be thin enough (< 0.5 μm) for imaging. Tilting of the specimen to higher angles (ideally to 70°) wasnt always possible due to the proximity of grid bars, ice crystals or neighbouring biological material getting in the way of the electron beam. All these requirements taken together made the searching for suitable spots for tomography a time-consuming endeavour. Tomograms of vitrified synaptosomes were characterized by smooth and continuous membranes and well distributed cytosolic material, with no indications of aggregation or rearrangement, as anticipated for this art of sample preservation (Figure 13, B).

In addition to synaptosomes, isolated postsynaptic densities were also used for studying the postsynaptic architecture by Cryo-ET. Isolated PSDs are the main component of the PSD fraction, which is obtained by a detergent-based extraction from the synaptosomal fraction. Frozen-hydrated isolated PSDs were usually found in clusters on the EM grid and in rare cases in isolation (Figure 14, A). The amount of membrane contamination in the PSD fraction appeared negligible and generally didnt interfere with Cryo-ET of isolated PSDs (Figure 14, A and B). Cryo-ET showed that PSDs have no preferred orientation on the EM grid and while some were found lying flat, forming disk like structures, others lied on their sides and appeared as thin electron-dense sections (Figure 14, B). EM grids of vitrified PSDs had in general thinner ice regions than those of synaptosomes and allowed recording of cryo-tomograms of higher signal-to-noise ratio (SNR). Finding good spots for tomography of PSDs was fairly straightforward.

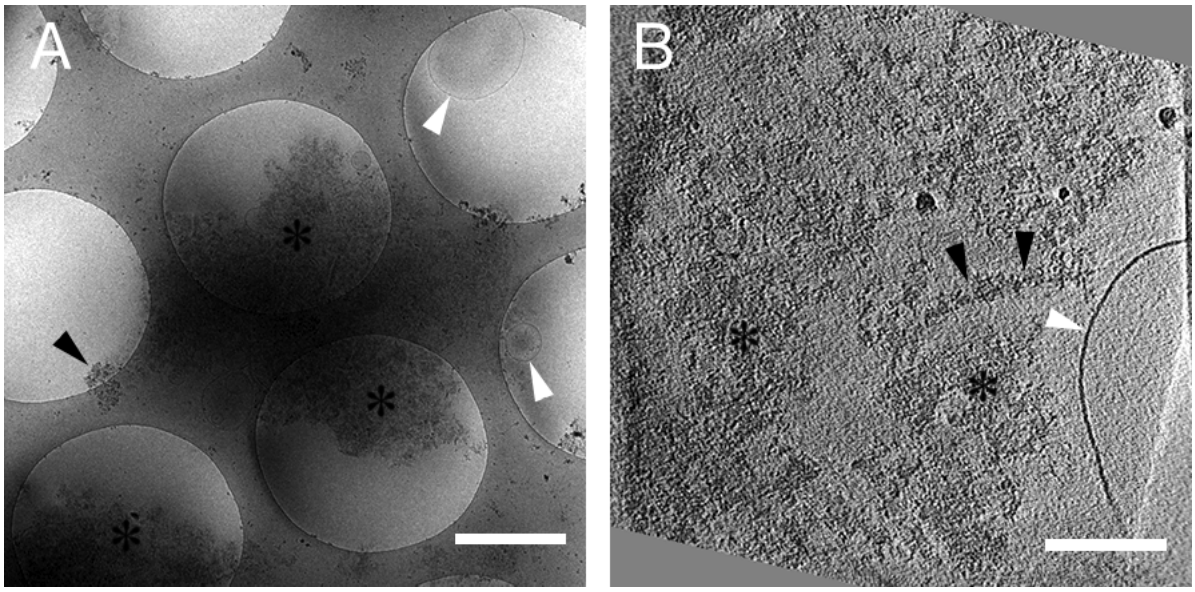

Figure 14: Images of Isolated PSDs at different magnifications. (A) Overview of PSDs on an EM grid. Isolated PSD (black arrowhead), clusters of PSDs (asterisks), undigested membranes (white arrowheads). (B) 1.9 nm-thick tomographic slice of a PSD fraction tomogram. Disc-like PSDs lying flat on the EM grid (asteresks), PSDs lying on their sides (black arrowheads), undigested membrane (white arrowhead). Scale bars: (A) 1000 nm, (B) 200 nm.

5.1.1 Pharmacological stimulation of synaptosomes causes an increase of CaMKII Thr286 autophosphorylation

It has been previously shown that pharmacological NMDAR stimulation in cultured neurons causes CaMKII activation and its subsequent translocation to postsynaptic sites (Shen and Meyer, 1999). This translocation requires CaMKII activation and the subsequent Thr286 autophosphorylation enhances its association with the PSD. In another study pharmacological NMDAR stimulation in cultured neurons and hippocampal slices caused a rapid (1.5 min.) translocation and accumulation of CaMKII to the cytosolic face of PSDs that resulted in an up to 2.1-fold increase in their thickness (Dosemeci et al., 2001). It has been demonstrated that such translocations are the specific result of NMDAR-mediated postsynaptic Ca2+ influx (Thalhammer et al., 2006).

In order to determine if NMDAR stimulation induces activation and translocation of

CaMKII in synaptosomes, we treated synaptosomes with: (i) Glutamate and Glycine (Glu/Gly) and (ii) Glutamate, Glycine and KCl (Glu/Gly/KCl). In both cases, we determined both the total amount of CaMKIIα and the amount of autophosphorylated CaMKIIα by immunoblotting with an antibody that recognizes total CaMKIIα and one that specifically recognizes Thr286-phosphorylated CaMKIIα, respectively. Fluorophore-conjugated secondary antibodies were used for detection, providing a stable quantitative fluorescent signal directly proportional to the amount of protein.

As expected, there was little difference in the total amount of CaMKII between treated and non-treated synaptosomes. Any differences could be attributed to imprecise protein loading. There was a 1.8 fold increase in the amount of Thr286 phosphorylated CaMKIIα in Glu/Gly treated synaptosomes compared to non-treated ones and a 3.4 fold increase in the case of Glu/Gly/KCl treated ones, as determined by densitometry (normalized to total CaMKII) (Figure 15, A).

In order to investigate a possible stimulation induced translocation of CaMKII from distal parts of the postsynaptic terminal to the PSD, we isolated PSD fraction from stimulated and control synaptosomes after synaptosomal stimulation using detergent extraction with Triton X-100 (please refer to section 7). Figure 15 C shows a Coomassie-stained polyacrylamide gel with lanes containing protein from the synaptosomal and PSD fractions. A fairly large subset of protein bands present in the synaptosomal fraction disappeared in the PSD fraction (arrowheads). On the other hand, a number bands were present in the PSD fraction that were either distinct from the synaptosomal fraction or appeared enriched in the PSD fraction (arrows).

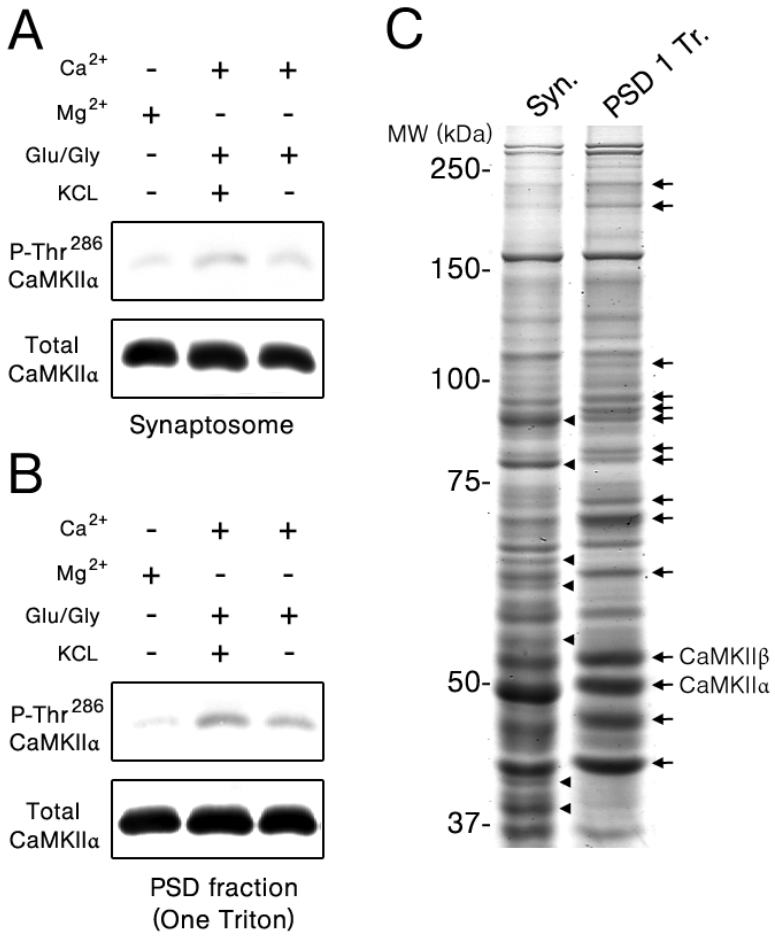

Figure 15: Pharmacologically induced increase in CaMKII phosphorylation in synaptosomes and isolated PSDs. (A) Synaptosomes stimulated with either GLU/GLY or GLU/GLY/KCl were probed with an antibody specific for Thr286-phosphorylated CaMKII (top gel) or an antibody recognizing total CaMKII (bottom gel). GLU/Gly treatment caused a 1.8 fold increase in the concentration of Thr286 phosphorylated CaMKII and Glu/Gly/KCl treatment caused a 3.4 fold increase, as determined by densitometry. Results are representative of two independent assays. (B) PSD fraction from synaptosomes stimulated with either GLU/GLY or GLU/GLY/KCl were probed with an antibody specific for Thr286-phosphorylated CaMKII (top gel) or an antibody recognizing total CaMKII (bottom gel). GLU/Gly treatment caused a 6.1 fold increase in the concentration of Thr286 phosphorylated CaMKII and Glu/Gly/KCl treatment caused a 10.5 fold increase, as determined by densitometry. (C) PSD fraction purification. Coomassie-stained SDS-PAGE gel loaded with synaptosomes (Syn), and PSD 1 Triton fraction. (PSD 1 Tr.). Arrowheads indicate bands not present in the PSD fraction and arrows indicate bands that are either distinct from the synaptosomal fraction or appeared enriched in the PSD fraction. Results are representative of two independent assays.

There was a moderate increase in the amount of total CaMKII in PSD fraction isolated from stimulated synaptosomes (both Glu/Gly and Glu/Gly/KCl) compared to PSD fraction isolated from control synaptosomes, which was indicative of CaMKII translocation to the PSD (Figure 15, B). Furthermore, there was a 6.1 fold increase in the concentration of Thr286 phosphorylated CaMKII in PSDs isolated from Glu/Gly treated synaptosomes, compared to controls and a 10.5 fold increase in the case of PSDs isolated from Glu/Gly/KCl treated ones, as determined by densitometry (Figure 15, B).

Therefore, the stimulation of synaptosomes caused CaMKII Thr286 autophosphorylation and a translocation of CaMKII to the PSD.

5.1.2 Pharmacological stimulation of synaptosomes doesn't induce an increase in the average cross-sectional thickness of PSDs

Here and in the next section, 45 tomograms out of 81 tomograms of synapses from control, Glu/Gly and Glu/Gly/KCl treated synaptosomes (15 tomograms per group) are considered. The PSDs were analysed by quantitative morphometry (please refer to section 7) in order to evaluate differences between the average cross-sectional thickness of their PSDs. PSDs from control, Glu/Gly and Glu/Gly/KCl treated synaptosomes showed a mean average cross-sectional thickness of 49.9 $\pm$7.2 nm, 46.3 $\pm$4.4 nm and 41.7 $\pm$4.3 nm respectively (Figure 16). There were no statistically significant differences between the group means as determined by one-way ANOVA ($p > 0.05$) and therefore neither Glu/Gly or Glu/Gly/KCl treatments seemed to cause a change in the in the average cross-sectional thickness of PSDs in synaptosomes.

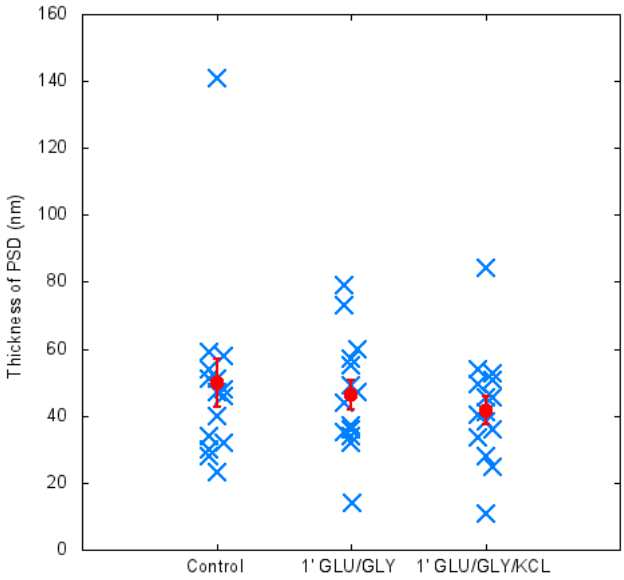

Figure 16: Scatter plot showing measurements of the thickness of PSDs from control and stimulated synaptosomes. Each cross corresponds to a measurement from an individual PSD. 15 PSDs were analyzed in each group. Crosses in individual groups were randomly shifted left or right on the x axis for a better visual representation. Red dots with error bars represent means ± SEM.

5.1.3 The architecture of frozen-hydrated postsynaptic terminals

Postsynaptic terminals ranged in shape and size (200 *nm* to 800 *nm* in diameter) and in most cases could be classified according to the traditional dendritic spine morphological classification (Peters and Kaiserman-Abramof, 1970) as either stubby, thin or mushroom type (Figure 17). The PSD appeared as an electron dense, disk-like shaped structure attached to the postsynaptic membrane and directly apposed to the active zone (Figure 17, A). It had a similar span as the synaptic cleft and its thickness and diameter ranged from 20 nm to 150 nm and 150 nm to 700 nm, respectively. Postsynaptic terminals occasionally contained actin filaments, vesicles or glycogen granules (Figure 17, B). The attached presynaptic terminals typically enclosed a few hundred synaptic vesicles and in some cases contained mitochondria (Figure 17, C).

Small filaments present within the structure of the PSD could be visually detected in

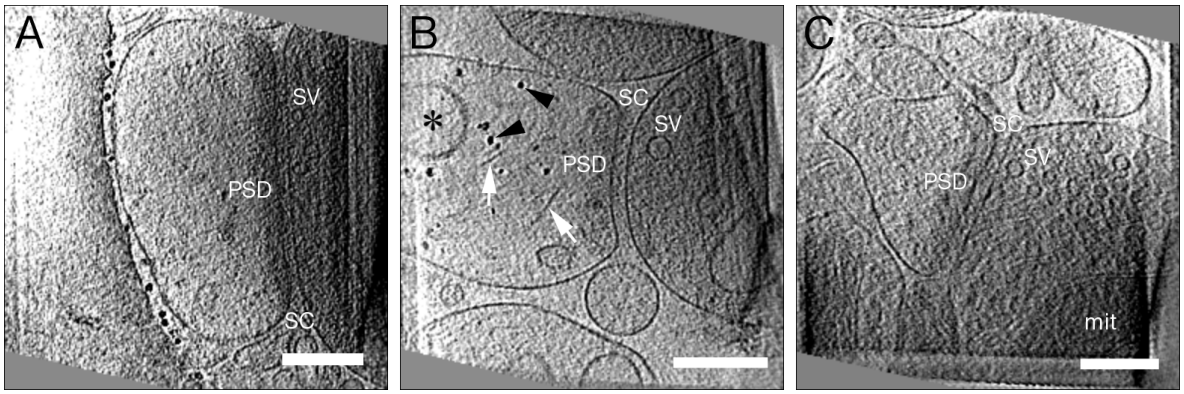

Figure 17: Dendritic spine morphology visualized in tomograms of frozen-hydrated synaptosomes. In panels A and C tomographic slices are 3.7 nm-thick, while in panel B they are 3 nm thick. Synaptic vesicle (SV), synaptic cleft (SC), postsynaptic density (PSD). (A) Mushroom type postsynaptic terminal with a large (800 nm in diameter) bulb. (B) Stubby type postsynaptic terminal with a large (150 nm in diameter) coated vesicle (asterisk), glycogen granules (black arrowheads) and actin fillaments (white arrows). (C) Thin type postsynaptic terminal. Scale bars: 200 nm.

tomograms of synaptosomes. Manual segmentation allowed for a better visualization of the PSD structure and revealed its complex morphology (Figure 18, A). Upon closer inspection, a dense network of filamentous structures oriented perpendicular and parallel to the synaptic cleft could be discerned (Figure 18, B), in agreement with a previous study on high-pressure frozen, dehydrated synapses (Chen et al., 2008).

Pyramid-like protrusions were sometimes seen extending into the cytosol and forming a rather convoluted cytosolic surface of the PSD (Figure 19, C). In some cases such protrusions extended deeper into the cytosol and appeared to enclose areas of empty space within the structure of the PSD (Figure 19, D). Although some PSDs appeared to be homogeneous in thickness and exhibited a somewhat smooth cytoplasmic surface (Figure 18, A; Figure 20, A) occasionally long filamentous structures attached to the PSD and extending up to a few hundred nanometers into the cytosol were present (Figure 19, A, B, D).

Around 20% of the examined postsynaptic terminals contained a dense mesh of actin

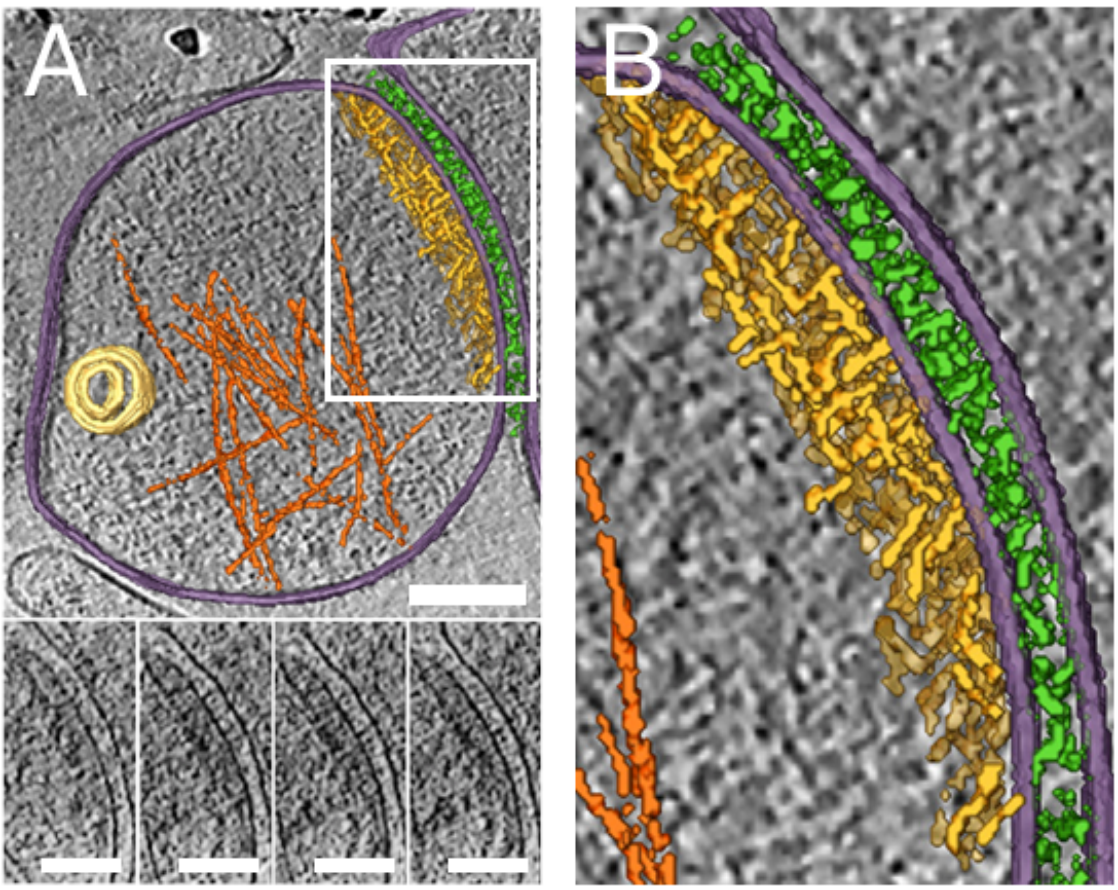

Figure 18: Morphology of PSD in frozen-hydrated synaptosomes. (A) Tomographic slice with overlaying manual segmentation showing synaptic adhesion complexes (green), PSD (gold), postsynaptic actin filaments (orange) and a postsynaptic vesicle (yellow). Insets: raw tomographic data at different z slices. Scale bar: 100 nm. (B) enlarged version of the area marked in A.

filaments that spanned the terminal and appeared to be associated with the PSD (Figure 20 A). Small vesicles (30-50 nm in diameter) were also present in such terminals and sometimes appeared to be associated with the actin filaments, suggesting some role in transport to or from the PSD (Figure 20 B).

Large (80-150 nm in diameter) vesicles, often containing prominent membrane densities and electron dense particles in their lumen, were present in 7 out of 45 examined postsynaptic terminals (Figure 21). One such vesicle was observed in direct contact with

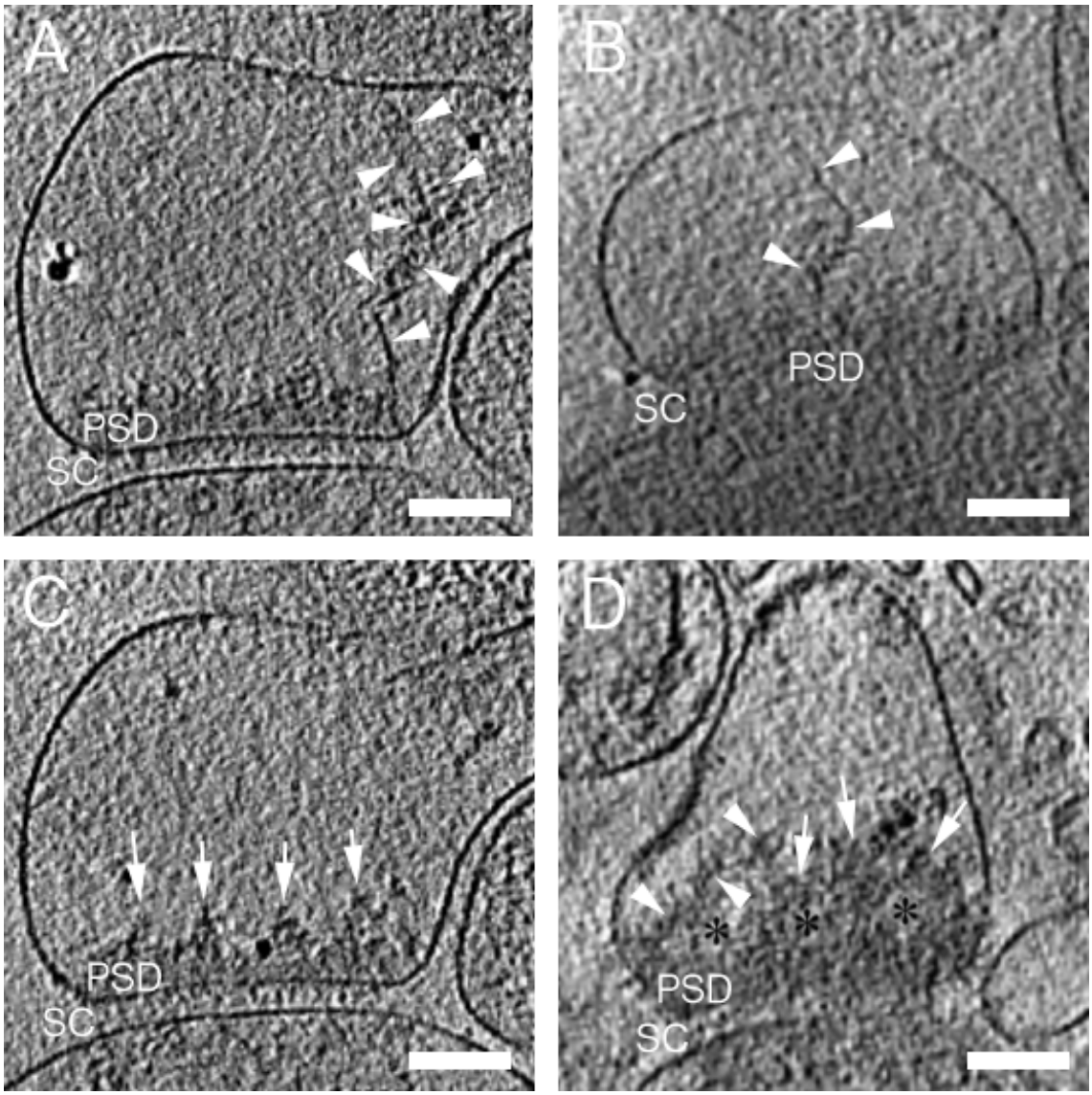

Figure 19: Postsynaptic morphology visualized in tomograms of frozen-hydrated synaptosomes. In all panels tomographic slices are 3.2 nm-thick. Synaptic vesicle (SV), synaptic cleft (SC), postsynaptic density (PSD). (A) and (B) Postsynaptic terminals with filamentous structures attached to the PSD and extending into the cytosol (white arrowheads). (C) Postsynaptic terminal with pyramid-like protrusions extending into the cytosol (white arrows). (D) Postsynaptic terminal with filamentous structures attached to the PSD and extending into the cytosol (white arrowheads) and pyramid-like protrusions extending into the cytosol (white arrows). Scale bars: 100 nm.

the postsynapic membrane in an open neck conformation, creating a continuity between the vesicular lumen and the extracellular space (Figure 21, A).

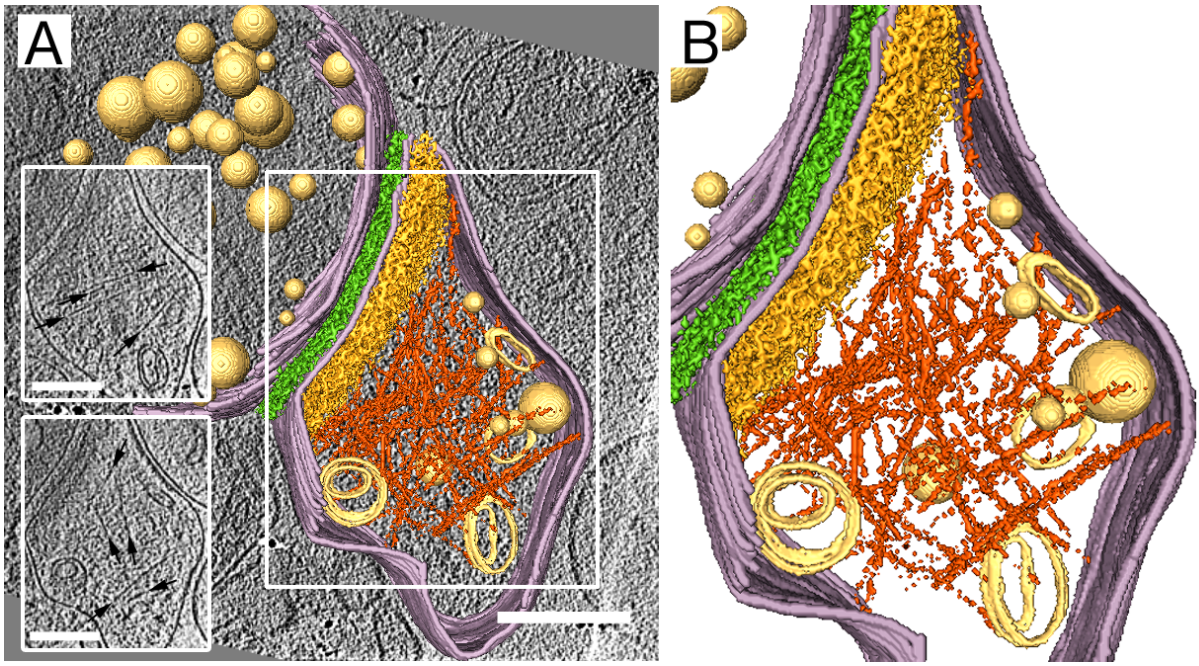

Figure 20: Postsynaptic actin filaments in frozen-hydrated synaptosomes. (A) Tomographic slice with overlaying manual segmentation showing synaptic adhesion complexes (green), PSD (gold), postsynaptic actin filaments (orange), synaptic membranes (lila) and postsynaptic and presynaptic vesicles (yellow). Insets: raw tomographic data at different z slices. Arrows point to actin filaments. Scale bars: 200 nm. (B) enlarged version of the area marked in A.

In most of the observed cases, such vesicles were located in the cytosol of the postsynaptic terminal (Figure 21, A; Figure 17, B). Interestingly, there was also a case where such a vesicle appeared to be associated with the PSD. In the same synapse, electron dense regions were present on the postsynaptic membrane some 200 nm away from the ends of the PSD on the membrane (Figure 21, C). The distances between these electron dense membrane regions and the ends of the PSD on the postsynaptic membrane were surprisingly similar to the distance between the site of direct vesicle membrane contact described above and the PSD ends in that tomogram (Figure 21, A). These observations suggest that these vesicles, together with the electron dense membrane regions, could play a role in trafficking of material to or from the PSD and are consistent with the idea that endo- or exocytotic hot spots occur in postsynaptic sites of neurons, acting as organizing platforms for signalling molecules and capable of undergoing clathrin-independent

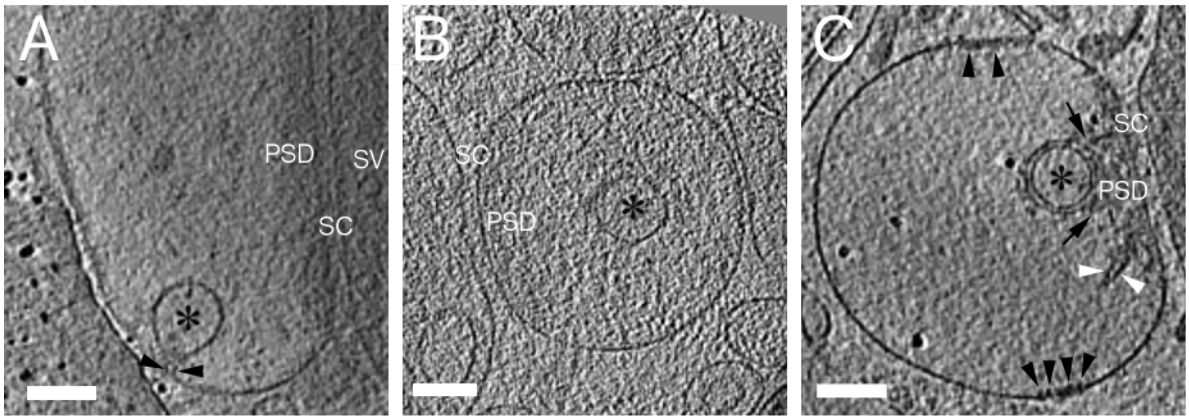

Figure 21: Postsynaptic transport with large vesicles visualized in tomograms of frozen-hydrated synaptosomes. In panels A and C tomographic slices are 3.7 nm-thick, while in panel B they are 3 nm thick. Synaptic vesicle (SV), synaptic cleft (SC), postsynaptic density (PSD). (A) Postsynaptic terminal containing a large (100 nm in diameter) vesicle (asterisk) in direct contact with the postsynaptic membrane in an open neck conformation (black arrowheads). (B) Postsynaptic terminal containing a large (100 nm in diameter) vesicle (asterisk) in its cytosol. (C) Postsynaptic terminal containing electron-dense regions on the postsynaptic membrane (black arrowheads), protrusions on the cytosolic face of the PSD and a large (90 nm in diameter) vesicle (asterisk) associated with the PSD (black arrows). Scale bars: 100 nm.

endocytosis (Suzuki, 2002; Allen et al., 2007). Furthermore it is known that extrasynaptic regions of the postsynaptic membrane (further than 100 nm from the PSD) are enriched in endocytotic proteins (Racz et al., 2004) and metabotropic glutamate receptors (mGluRs) (Baude et al., 1993). Other structures such as multivesicular bodies or endosomes were also present in the examined postsynaptic terminals.

No clear morphological differences could be visually distinguished between postsynaptic terminals of treated and untreated synaptosomes. This data suggests that NMDAR stimulation does not induce any large scale rearrangements in the postynaptic architecture.

5.1.4 Morphology of frozen-hydrated isolated postsynaptic densities

In this section, 12 out of 30 tomograms of PSDs isolated from control and Glu/Gly/KCl treated synaptosomes (5 tomograms per group) are considered. Frozen-hydrated isolated PSDs showed morphological characteristics similar to the ones exhibited by PSDs in synaptosomes. Manual segmentation of Isolated PSDs lying sideways on the EM grid (orientation similar to the one found in synaptosomes) revealed a similar dense network of filamentous structures oriented perpendicular and parallel to the synaptic cleft (Figure 22).

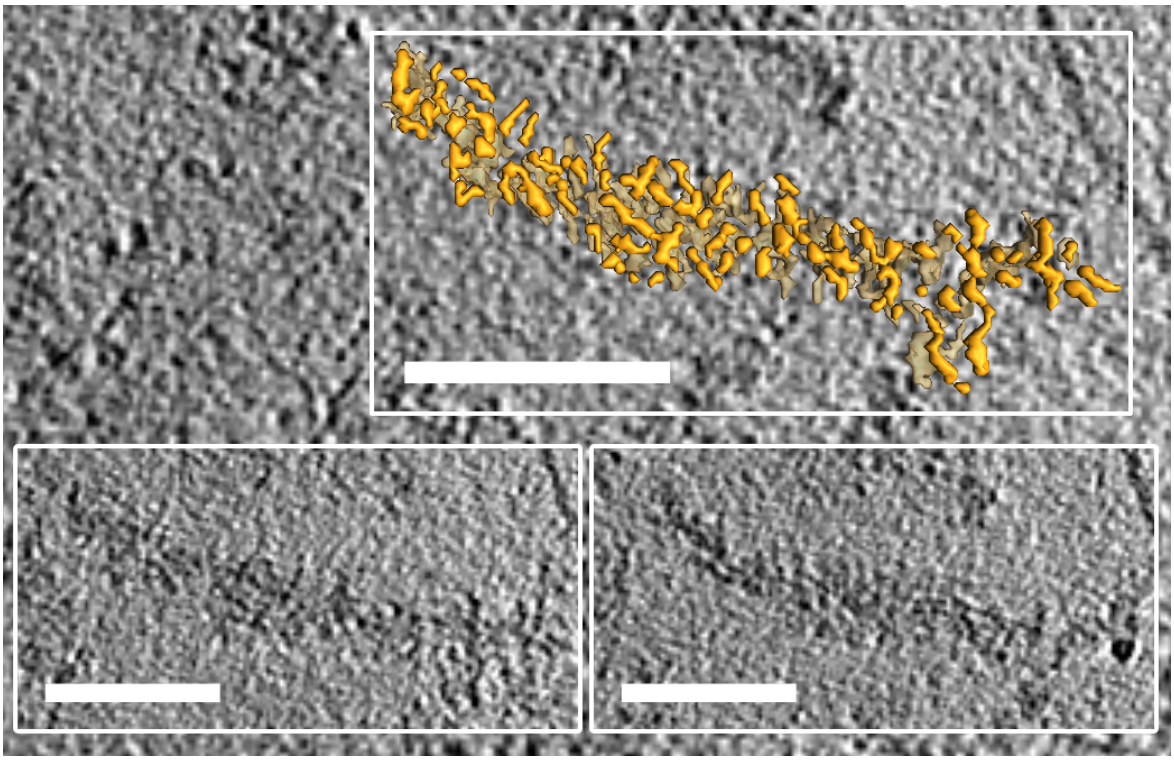

Figure 22: Tomographic slice (1.52 nm) of a PSD fraction tomogram with overlaying manual segmentation showing PSD morphology (yellow). Insets: raw tomographic data at different z slices. Scale bar: 100 nm.

Due to the thinner ice in grids of isolated PSDs and the lack of enclosing postsynaptic membranes the signal-to-noise ratio of the tomograms was superior to the one in tomograms of synaptosomes. This, combined with the fact that some isolated PSDs were lying flat on the grid (an orientation not available in tomograms of synaptosomes)

allowed for a more detailed look into the finer morphology of the PSD. Similar to the structure of PSDs in synaptosomes and consistent with previous observations (Petersen et al., 2003), the majority of isolated PSDs showed two distinct surfaces. One surface was somewhat smooth and planar (Figure 23, left), whereas the other surface was convoluted and showed areas of empty space within the structure of the PSD (Figure 23, right).

Semi-automatic segmentation revealed that the planar surface is continuous and composed of short (5-10 nm) filaments (Figure 24, A left, B left). The convoluted surface, on the other hand, was found to contain longer filaments (20-30 nm) and showed irregular protrusions sticking out of the regular structure formed by the planar surface (Figure 24, A right, B right). This is very similar to the observations on the PSD structure in synaptosomes, strongly suggesting that the planar surface was the cleft surface of the PSD, while the convoluted surface was its cytosolic surface. This was additionally confirmed by examining the curvature at a lateral section through a segmented PSD (Figure 24 C). Looking at lateral sections at different positions through the structure of the PSD revealed that ,similar to synaptosomes, the PSD contains areas of empty space within its structure that appeared to be enclosed by the protrusions on its cytosolic face. The cleft side of the PSD, on the other hand appeared to form a somewhat regular continuous mesh with a rather homogeneous thickness (30-40 nm) (Figure 24 C).

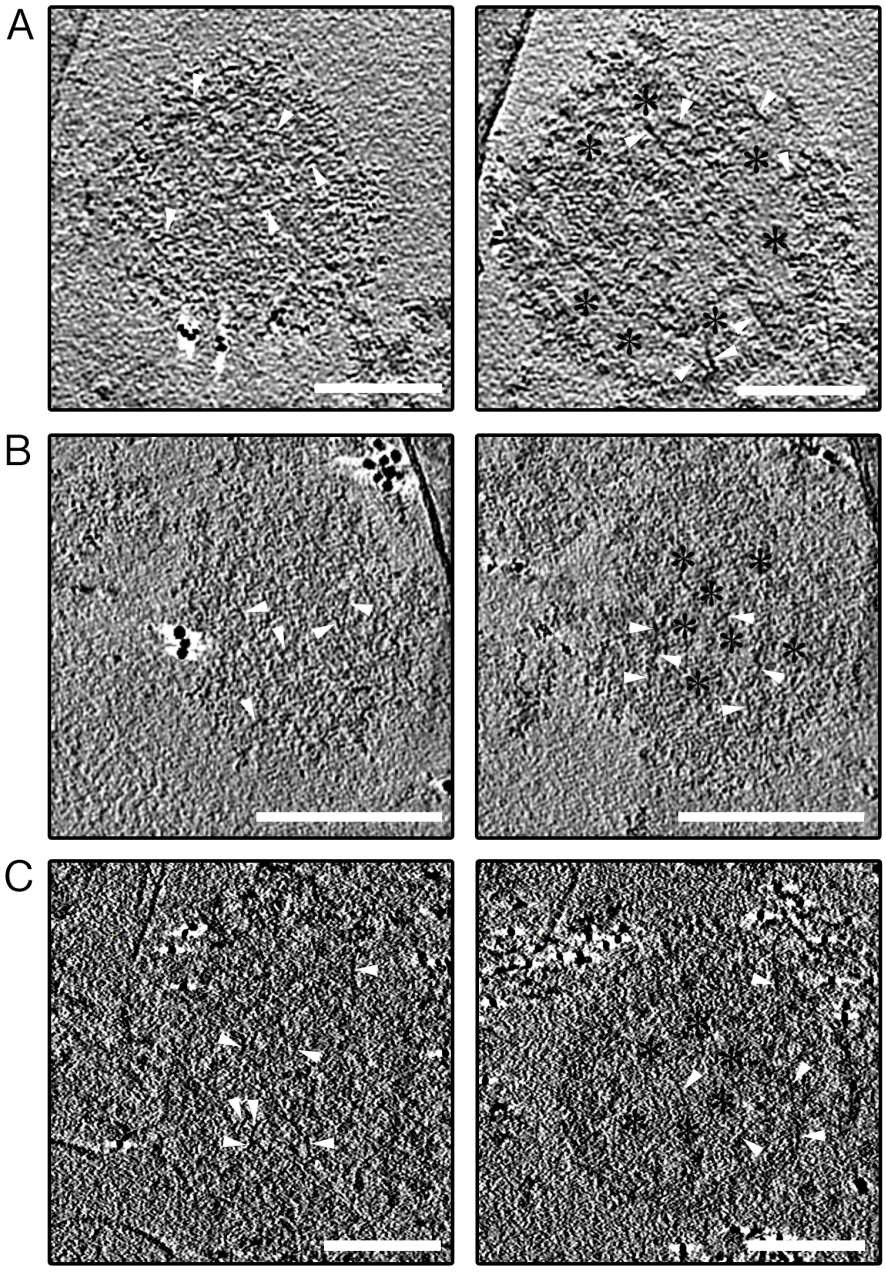

Figure 23: The two distinct surfaces of the PSD. Tomographic slices showing the planar, cleft side (left) and the convoluted, cytosolic side of the PSD (right). White arrowheads point to short (left) and long (right) filaments, while asterisks show empty spaces in the PSD structure. Each row shows two different slices of same tomogram that are 1.16 nm (A), 1.52 nm (B) and 1.68 nm(C) thick. Scale bars: 200 nm.

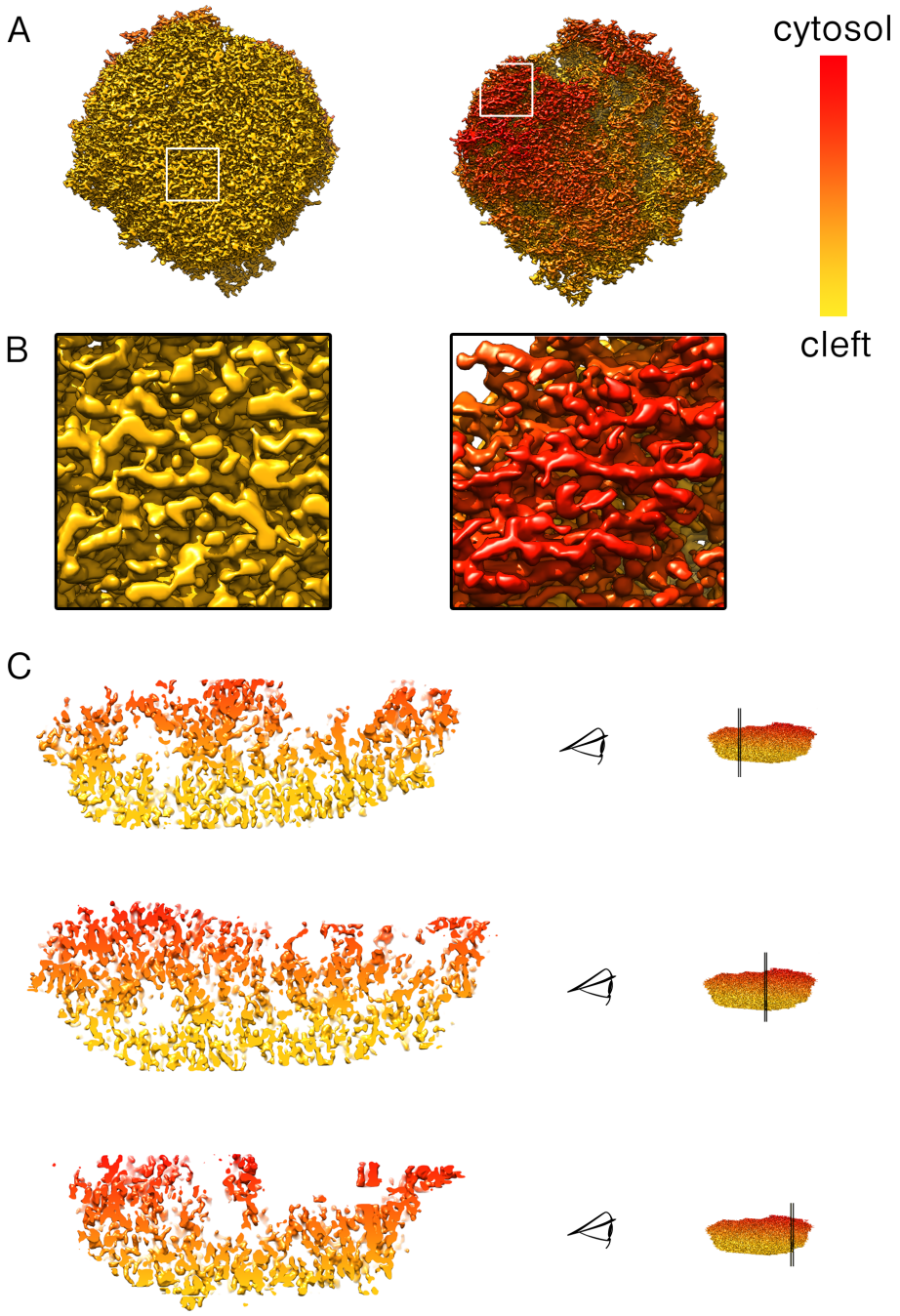

Figure 24: Semi-automatic segmentation of the PSD in Figure 23, A. (A) The planar cleft side (left), the convoluted cytosolic side (middle) and a gradient color bar from yellow (postsynaptic membrane) to red (cytosol). (B) Zoomed-in versions of the boxed regions in A. (C) Lateral sections of 4 slices (left) cut at positions specified by planes through the PSD (right) as seen from the perspective of the eye (middle) looking towards the PSD (right).

Upon closer inspection it becomes apparent that in addition to filamentous structures, the PSD contains globular proteins, some of which are very similar in shape and size (10 nm across) to the CaMKII association domain (Figure 25, A). The protein structures are most abundant in tomographic slices through the convoluted cytosolic surface of the PSD, consistent with earlier observations that CaMKII lies exclusively at the cytoplasmic surface of the PSD, associated with tower-like protrusions (Petersen et al., 2003). Comparison between selected CaMKII-like structures from tomograms of isolated PSDs and boxed CaMKII particles from single particle tomography of purified CaMKII revealed a remarkable resemblance between these structures (Figure 25, B). Reliable visual identification of these molecules in tomograms is however not feasible and requires computational detection methods such as template matching. Similar to PSDs in synaptosomes no clear morphological differences could be detected between isolated PSDs from treated and untreated synaptosomes, which further emphasized the need for template matching for CaMKII.

Very recently, we were able to collect cryo tomograms of isolated PSDs on a TEM equipped with a last generation DDD and a TEM phase plate. These tomograms are characterized by a significantly improved signal-to-noise ratio and resolution, compared to the ones collected on scintilator-coupled CCDs (Figure 26)

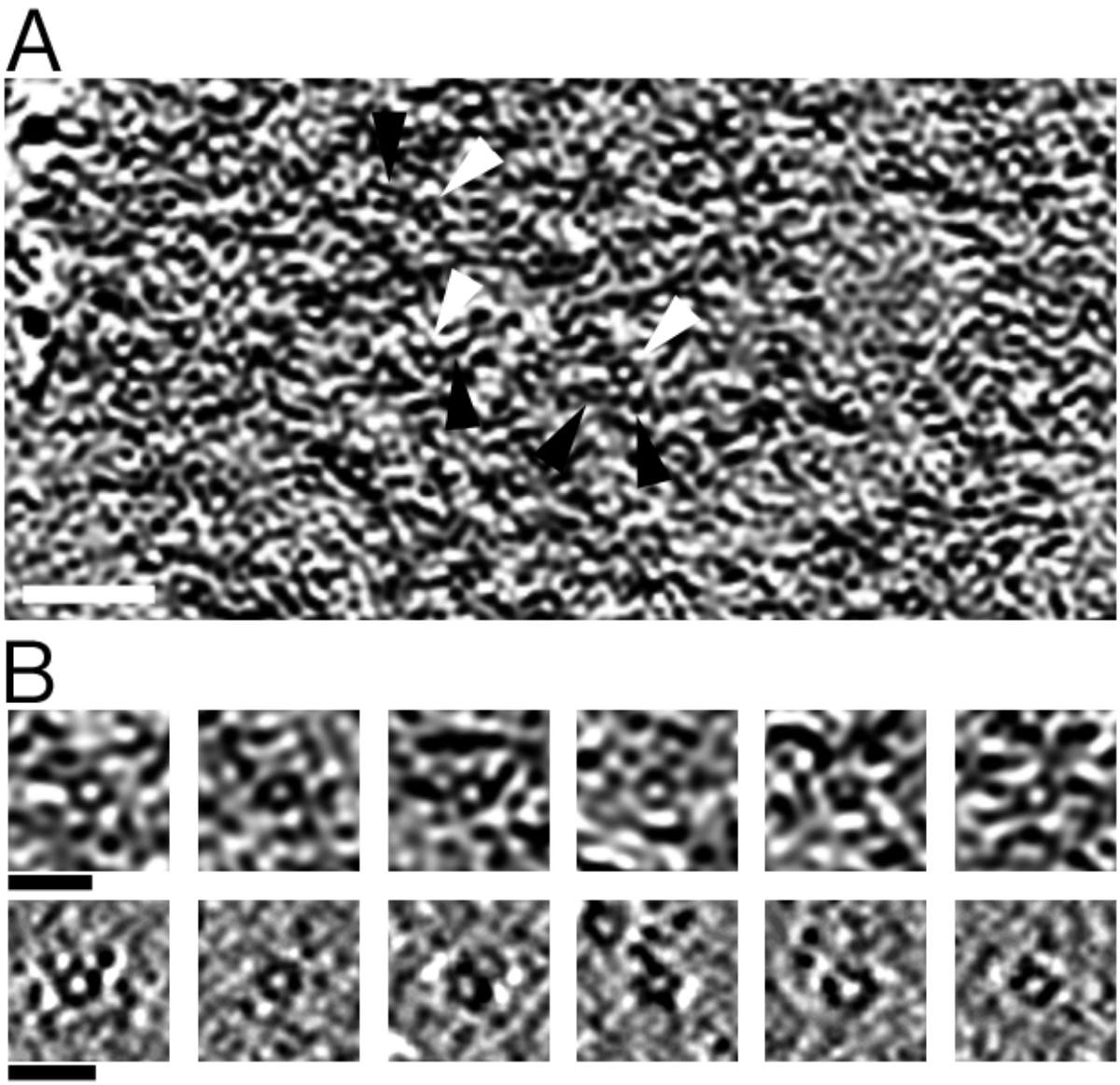

Figure 25: Fine morphology of a frozen hydrated, isolated PSD. (A) Tomographic slice showing the fine morphology of isolated frozen-hydrated PSDs. White arrowheads point to putative CaMKII protein particles and black arrowheads point to short fillaments attached to these particles. Scale bar: 50 nm. (B) CaMKII-like structures in tomographic slices from selected positions of PSD fraction tomograms (top) and tomographic slices from tomograms of purified CaMKII holoenzymes (bottom). Scale bar: 20 nm.

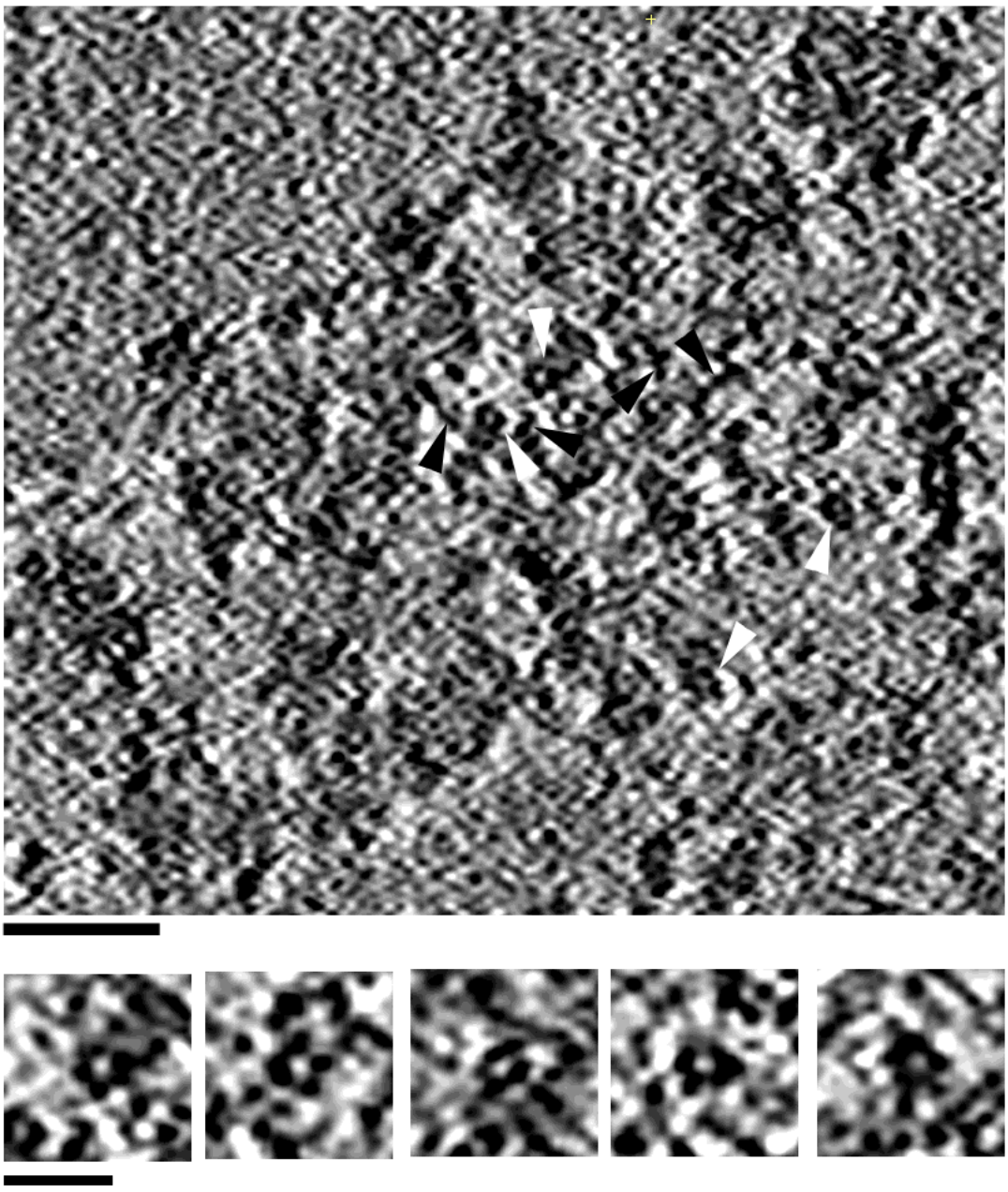

Figure 26: Tomogram of a frozen hydrated isolated PSD collected on a DDD in combination with a TEM phase plate. (upper pannel) Tomographic slice of an isolated frozen-hydrated PSD. White arrowheads point to putative CaMKII protein particles and black arrowheads point to short fillaments within the PSD structure. Scale bar: 50 nm. (lower pannel) CaMKII-like structures in tomographic slices from selected positions of the tomogram in the upper pannel. Scale bar: 20 nm.

5.1.5 Template matching of CaMKII in tomograms of cortical synaptosomes and isolated PSDs

Because CaMKII plays a major role in synaptic signaling, the precise determination of the location of inactive and activated CaMKII within the synapse is of great interest.This could potentially provide important insights about the three dimensional molecular architecture of the PSD and into several fundamental aspects of synaptic function, such as the long-term potentiation

Template matching has the potential to detect the positions and orientations of molecules within their natural environments. However, the application of this method to determine the location of CaMKII within the structure of the PSD in cryotomograms of synaptosomes and isolated postsynaptic densities is not trivial due to the low SNR of cryotomograms, the missing wedge, the non-isotropic resolution in the direction of the beam and the fact that macromolecules are difficult to recognize in a crowded molecular environment (Best et al., 2007). Furthermore an accurate template is required in order for the method to work reliably (Xu et al., 2011).

At the time, there were two CaMKII holoenzyme structures available in the public domain. One was a SAXS based model composed of crystal structures of the CaMKII association domain dodecamer and the kinase domain dimer. In this model, the kinase domains are arranged in a ring coplanar with the midplane of the central association domain (Figure 27, A) (Rosenberg et al., 2005). The other available structure was an X-ray structure of full-length human CaMKIIα construct with a very short CaMKIIβ7 (an alternative splicing variant of human CaMKIIβ) linker region (Chao et al., 2011) and showed a very different architecture, with the kinase domains extending above and below the midplane of the central association domain. In the following, the full-length human CaMKIIα construct with a short CaMKIIβ7 linker region will be referred to as CaMKIIβ7 short linker. While the SAXS based model closely resem-

bled the arrangement seen in a negative stain single particle structure of a full-length mouse CaMKII holoenzyme (Morris and Torok, 2001), the CaMKIIβ7 short linker X-ray structure was rather similar to a Cryo-EM single particle structure of full-length mouse CaMKII holoenzyme (Kolodziej et al., 2000).

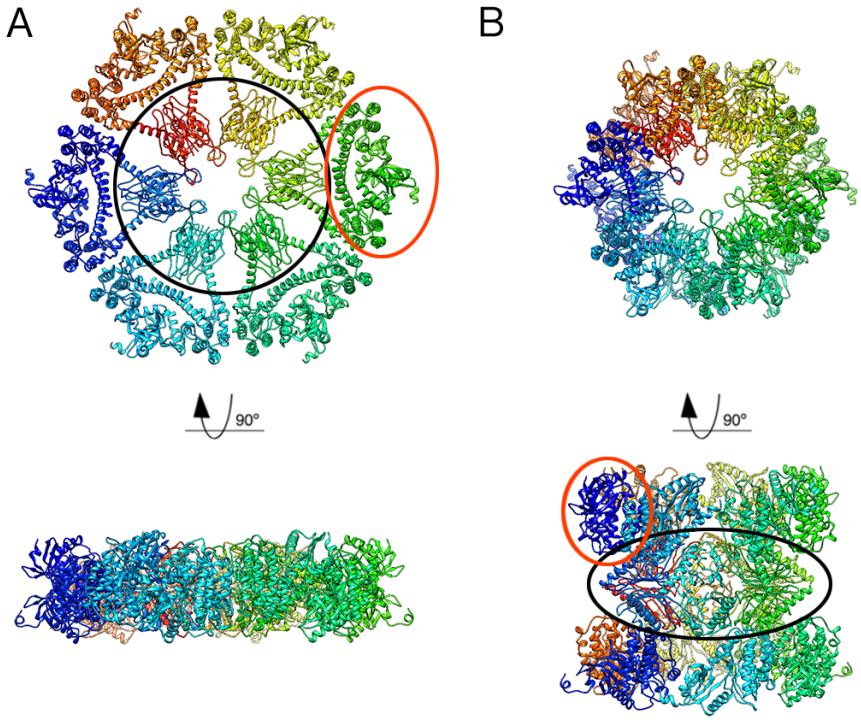

Figure 27: Crystal structure extended model generation. (A) Original crystal structure model with a central association domain encircled in black and kinase domain dimer encircled in red. (B) Modified crystal structure model with a central association domain encircled in black and individual kinase domains (a single kinase domain encircled in red) moved above and below the midplane of the association domain.

In order to explain this discrepancy it was proposed that inactive CaMKII forms tightly packed autoinhibited assemblies that upon activation convert to clusters of loosely tethered independent kinase domains (Rosenberg et al., 2005). Following up on that idea, we used the available holoenzyme model (Rosenberg et al., 2005) and computationally moved the kinase domains above and below the midplane of the central association domain with the idea to create a model of an activated CaMKII holoenzyme. This newly generated model (Figure 27, B) somewhat resembled the cryo-EM single particle struc-

ture of full length mouse CaMKII holoenzyme (Kolodziej et al., 2000). Templates for template matching were created for both structures by calculating the electrostatic potentials by summing the total atomic numbers Z in each volume element. The resulting densities were convoluted with the microscope contrast transfer function calculated for the defocus value used and low-pass filtered. (Figure 28)

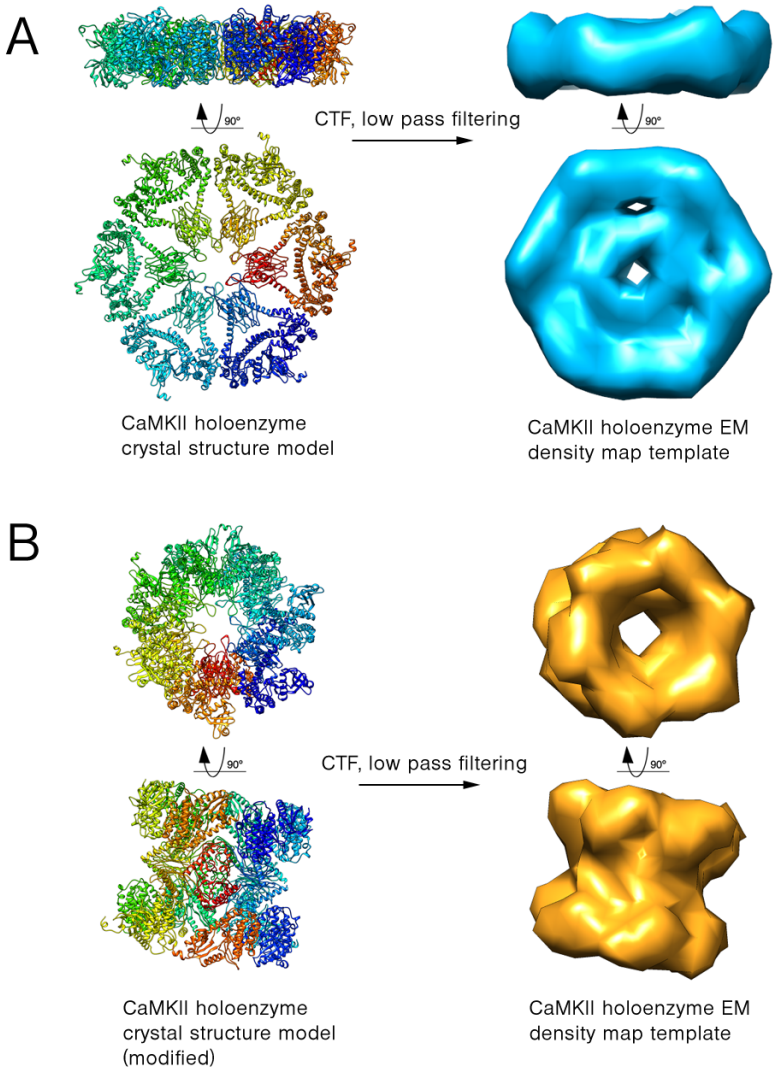

Figure 28: Template generation for template matching. (A) CaMKII crystal structure disk-like model (left) and corresponding template (right). (B) CaMKII crystal structure model with kinase domains displaced above and below the central association domain (left) and and corresponding template (right).

Template matching was performed on 8 tomograms of synaptosomes (4 treated and 4

control) and 6 tomograms of isolated PSDs (3 treated and 3 control) using both templates (Figure 30). As it was the case in previous applications of template matching (Pfeffer et al., 2012), the highest cross-correlation values were obtained for Au markers and membranes. Cross-correlation peaks corresponding to such false-positive matches were discarded and the next 100 were examined for each tomogram. In tomograms of synaptosomes, more than a third of the examined hits in each case detected particles that visually resembled the CaMKII association domain. However, no clear differences in the localization of active and inactive CaMKII could be recognized between tomograms of stimulated and non-stimulated synaptosomes.

In tomograms of isolated PSDs, approximately a quarter of the examined hits in each case detected particles that visually resembled the CaMKII association domain. Similar to tomograms of synaptosomes, no apparent differences in the localization of active and inactive CaMKII within the structure of the PSD could be identified between tomograms of PSDs isolated from stimulated and non-stimulated synaptosomes.

Subtomogram alignment and averaging of the first 100 identified CaMKII particles for each active and inactive state of the holoenzyme in each of the examined tomograms (both synaptosomes and PSD fraction) did not improve the structure of the CaMKII holoenzyme. As this could potentially be a consequence of the low number of averaged particles, we generated larger particle datasets by combining CaMKII particles identified as active or inactive in each tomogram of both synaptosomes and isolated PSDs and performed another round of subtomogram alignment and averaging on the newly generated datasets. This attempt still failed to improve the structure of the CaMKII holoenzyme.

Using structures of the CaMKII holoenzyme that we determined by single particle analysis (please refer to section 5.2), we performed a test round of template matching on

a tomogram of an isolated PSD collected on a first generation DDD (without phase plate) (Figure 29). Tomograms collected on DDDs were generally characterized by a superior visual appearance compared to the ones collected on conventional scintillator-coupled CCDs. Still, no apparent differences in the localization of active and inactive CaMKII within the structure of the PSD could be identified by template matching in that tomogram. Subtomogram alignment and averaging of datasets consisting of the first 100 identified CaMKII particles for each active and inactive state of the holoenzyme, with obvious false positives (e.g. Au fiducial markers) excluded, was in both cases unsuccessful in improving the structure of the CaMKII holoenzyme.

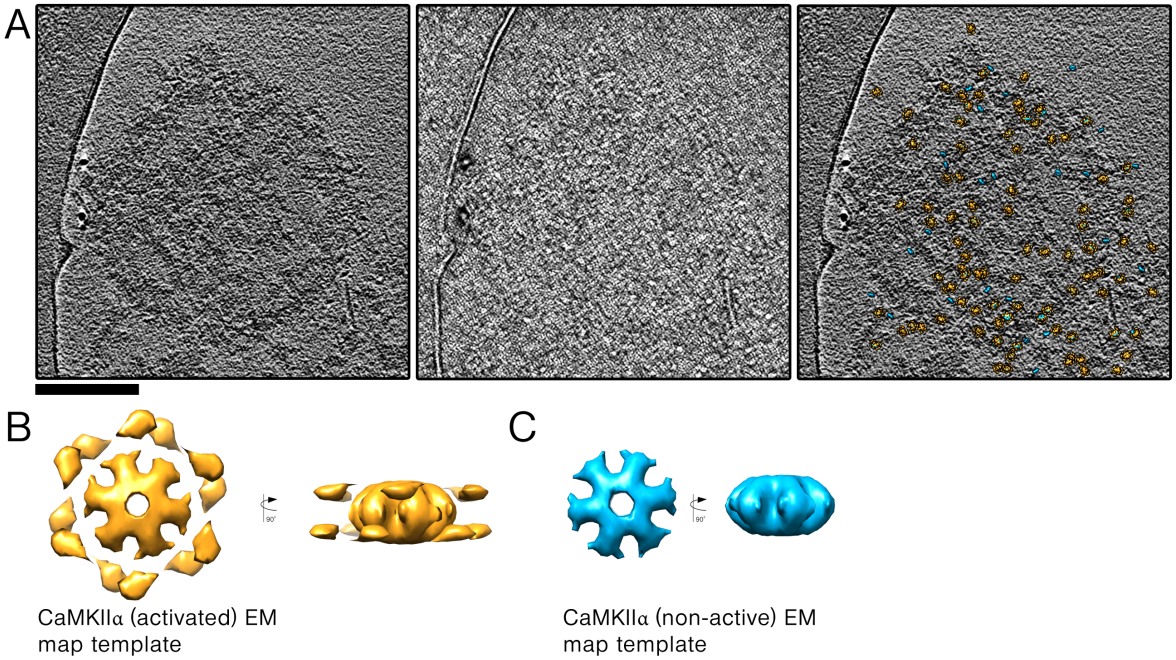

Figure 29: Visualization of template matching CaMKII, performed on a tomogram of an isolated PSD collected on a first generation DDD. (A) Original tomogram(left), cross-correlation volume obtained by template matching (middle) and original tomogram with single particle structures of activated and non-active CaMKIIα according to positions and orientations determined by template matching (right). (B) Single particle structure of activated CaMKIIα. (C) Single particle structure of non-active CaMKIIα. Scale bar: 200 nm.

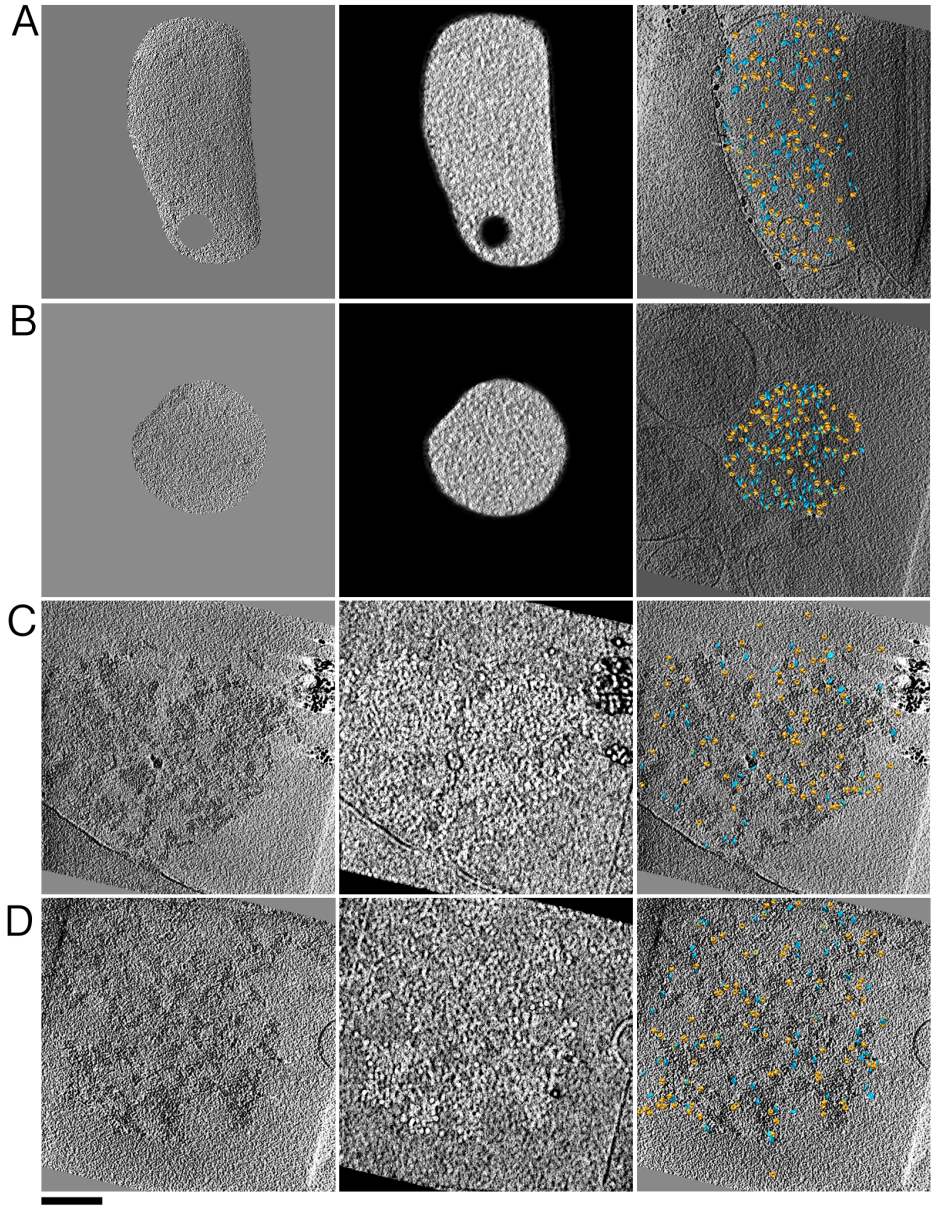

Figure 30: Visualization of template matching CaMKII in tomograms of synaptosomes and isolated PSDs. (A) Glu/Gly/KCl treated synaptosome. (B) control synaptosome. (C) PSD isolated from a Glu/Gly/KCl treated synaptosome. (D) PSD isolated from a control synaptosome. Panels represent original tomograms (left), cross-correlation volume obtained by template matching (middle) and original tomogram with model structures (section) of activated and non-active CaMKII according to positions and orientations determined by template matching (right). NOTE: in the case of tomograms of synaptosomes, everything else except the postsynaptic terminal was masked to aid interpretation. Scale bar: 200 nm.

5.2 Structure of recombinantly expressed mouse CaMKIIα

The structures of both activated and non-active recombinantly expressed CaMKIIα holoenzymes were determined by Single Particle Cryo-EM and by Cryo-ET in combination with sub-tomogram alignment and averaging. Structures obtained by Cryo-ET served as initial references for single particle reconstructions. Single particle datasets were processed using both the EMAN2 and RELION software packages, producing slightly different results. CaMKIIα sample preparation and vitrification for both SPR and Cryo-ET proved to be challenging. A number of problems, discussed within the next subsection, had to be overcome in order to establish a working sample preparation protocol that allowed the generation of EM samples suitable for data collection and processing.

5.2.1 Sample preparation and vitrification

C-terminal FLAG-tag mouse CaMKIIα was cloned into a donor plasmid, transposed into bacmid and transfected into Sf9 cells for expression and purification with the baculovirus expression system by Dennis Zimmermann (Department of Cell Biology, LMU Munich) (please refer to section 7). CaMKIIα FLAG-affinity purification was carried out from 300-350 ml of Sf9 cell suspension culture and typically yielded 20 μM CaMKIIα (approximately corresponding to 1.1 mg/ml) in a final volume of 400-500 μl. (Figure 31).

In total five different protein expression and purification experiments were carried out during the course of this work with the quality of the resulting protein samples varying between the experiments and improving towards the last experiments. After FLAG-affinity purification, protein samples were either kept at $4°C$ or dialyzed into a buffer containing 10% glycerol and snap frozen in LN_2 (intended for long term storage for up to several months at $-80°C$).

Negative stain and vitrified EM samples were initially prepared from dialyzed CaMKIIα

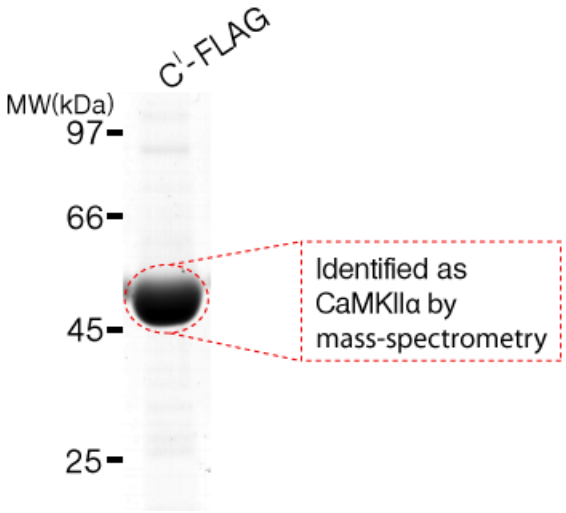

Figure 31: Coomassie stained SDS-gel showing purified C-terminal FLAG-tagged recombinantly expressed mouse CaMKIIα. A prominent protein band at $\sim$ 50 kDa is identified as CaMKIIα by mass-spectrometry. The positions of the molecular size marker are shown on the left.

protein samples containing 10% glycerol. The choice of this preparation had to do with the fact that the protein samples could be stored up to few months at $-80°C$, which allowed for a number of EM experiments to be carried out with a single protein expression and purification. Although micrographs of negatively stained CaMKIIα from such samples often showed relatively well distributed particles (Figure 32, A), micrographs of vitrified samples prepared by conventional manual plunge freezing (please refer to section 7) usually showed big protein aggregates and thick vitreous ice (Figure 32, B). Leaving the diluted protein sample on ice for at least an hour before plunge freezing seemed to disperse the aggregations in some cases, but wasn't a reliable method to get rid of them entirely. (Figure 32, C).

Furthermore the addition of colloidal gold markers to vitrified samples prepared in this way resulted in the formation of gold particle clusters, associated with protein aggregates (Figure 32, D). In an attempt to overcome some of these problems an additional continuous thin layer of carbon was applied to the Lacey carbon EM grids. This method, however, resulted in no significant improvement in either ice thickness or protein ag-

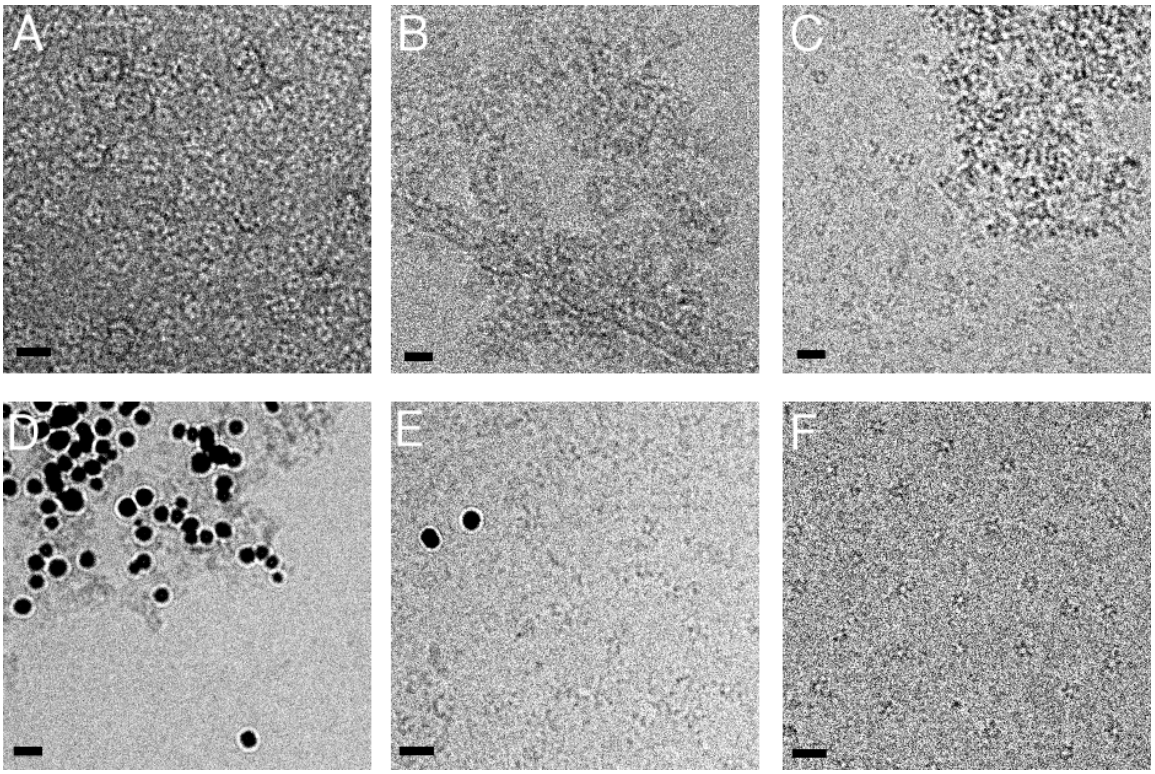

Figure 32: CaMKIIα sample preparation. (A) negative stain micrograph of CaMKII. (B) Micrograph of frozen-hydrated CaMKIIα showing a thick ice region and protein aggregations. (C) Micrograph of frozen-hydrated CaMKIIα after being left for 1h on ice before plunging. (D) Micrograph of frozen-hydrated CaMKIIα with Au fiducial markers showing Au clusters associated with protein aggregates. (E) Micrograph of frozen-hydrated CaMKIIα with Au fiducial markers showing no protein aggregations. (F) Micrograph of frozen-hydrated CaMKIIα showing no protein aggregations. Pixel size: A: 2.78 Å/pix and B,C,D,E,F: 2.21 Å/pix. Scale bars: 20 nm.

gregation and was soon abandoned. The duration of glow discharging was also varied between sample preparations and a duration of 30 sec. was found to be somewhat optimal. Altogether, vitrified EM sample preparation by conventional, manual plunge freezing from dialyzed CaMKIIα protein samples containing 10% glycerol was characterized by a very limited reproducibility and usually suffered from protein aggregation artefacts.

A possible reason for the number of problems encountered with this type of samples could be the fact that the samples had to be washed on the EM grid with either H_2O or buffer right before plunge freezing in order to dilute the glycerol concentration. In

order to exclude that possibility, dialysis, the last step of CaMKII purification, was omitted so CaMKII was kept in elution buffer without glycerol. CaMKII was then vitrified using an FEI Vitrobot^{TM} Mark IV (FEI, Hillsboro, OR). The controlled humidity and temperature environment of the Vitrobot allowed for reproducible sample freezing while the use of a non-dialyzed CaMKIIα protein sample containing no glycerol allowed for the washing steps to be avoided. This not only significantly improved the vitrified EM sample preparation for SPR (Figure 32, F), but also allowed the preparation of reproducible vitrified samples with nicely dispersed colloidal gold markers and no apparent protein aggregations (Figure 32, E). With the purpose of producing samples of activated CaMKIIα, protein samples were stimulated prior to vitrification with Ca^{2+} and Calmodulin, as previously described (Lučić et al., 2008) with minor modifications.

Oana Michalache helped significantly in optimizing the sample vitrification by conventional manual plunge freezing.

5.2.2 CaMKIIα Single Particle Tomography and subtomogram averaging

Cryo-ET was performed on both non-active and activated recombinantly expressed CaMKIIα with the goal of generating a starting reference for single particle reconstruction by sub-tomogram alignment and averaging. Tomographic data acquisition was performed on three different transmission electron microscopes: two operated at 300 kV (Tecnai 'Polara' G^2 F30, FEI; Titan KRIOS, FEI) and one operated at 200 kV (Tecnai F20, FEI). CaMKIIα holoenzymes were hardly visible and difficult to identify in tomograms collected at 300 kV, whereas they were easily recognisable in tomograms collected at 200 keV (Figure 33A,B). Subsequently, only tomograms collected at 200 kV were used for sub-tomogram averaging.

Mere visual comparison between CaMKIIα holoenzymes from tomographic reconstructions of non-active vs. activated CaMKIIα samples revealed striking morphological

differences. While non-active CaMKIIα holoenzymes appeared as globular ring-like structures of $\sim$ 10 nm in diameter with no apparent density around the structure (Figure 33, A), activated CaMKIIα holoenzymes appeared as similar ring-like structures but surrounded by electron-dense protrusions (Figure 33, B). The ring like structures seen in both cases resemble the CaMKIIα central association domain, while the electron-dense protrusions observed in activated CaMKIIα holoenzymes resemble the CaMKIIα kinase domains. Both structures appear similar to the ones observed previously (Kolodziej et al., 2000; Morris and Torok, 2001).

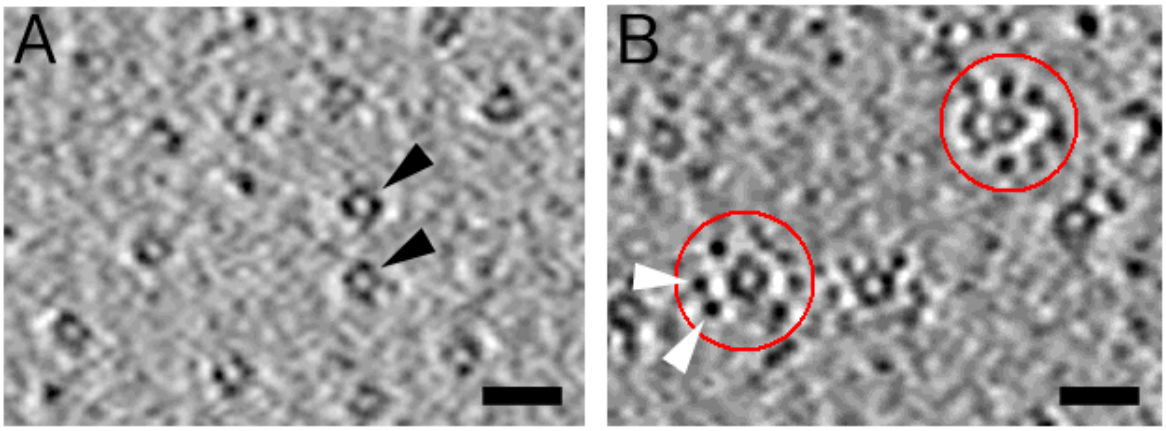

Figure 33: Cryo-ET of non-acive CaMKIIα vs. Cryo-ET of activated CaMKIIα. (A) Tomographic slice (0.89nm thick, -3.5μm defocus) of non-acive CaMKIIα showing CaMKIIα particles clearly visible (black arrowheads). (B) Tomographic slice (0.89nm thick, -3.5μm defocus) of activated CaMKIIα showing CaMKIIα particles clearly visible (red circles) and electron-dense protrusions around the particles (white arrowheads). Scale bar: 20 nm.

A number of tomograms were collected from both non-active and activated CaMKIIα samples at different defocus values, with the exact numbers and conditions summarized in (Table 1).

Boxing of CaMKIIα particles for sub-tomogram alignment and averaging was done in the following way: Initially 259 particles from a single tomogram of non-active CaMKIIα collected at -3.5 μm nominal defocus were boxed manually using the EMAN2 (Tang

Sample	№of experiments	№of tomograms @-3.5 μm	№of tomograms @-5.0μm	№of sub-tomograms @-3.5 μm	№of sub-tomograms @-5.0 μm
non-active CaMKIIα	2	7	13	1832	1146
activated CaMKIIα	2	8	14	1631	3309

Table 1: CaMKIIα tomograms processed for single particle subtomogram averaging

et al., 2007) image processing suite (Figure 34, A). The particles were then translationally aligned and averaged using the real space alignment procedure from the PyTom toolbox (Hrabe et al., 2012) starting from a randomly chosen boxed particle. This procedure yielded a low resolution (∼40 Å) structure of the CaMKIIα holoenzyme (Figure 34, picking B).

This structure then served as a template for template matching, using the PyTom toolbox (Hrabe et al., 2012), that was performed on all the CaMKIIα tomograms. Boxing of particles in this way proved to be very robust method, with high-score cross-correlation template matching peaks typically associated with CaMKIIα holoenzyme particles (Figure 34, C and D). The first few hundred hits were evaluated visually using EMAN2 (Tang et al., 2007) in order to remove false positives such as boxed gold markers and contaminants, producing data sets of sub-tomograms containing CaMKIIα holoenzyme particles (Table 1). In order to generate starting references for single particle analysis, two random sub-tomogram datasets of both non-active and activated CaMKIIα, each originating from a single tomogram collected at -3.5 μm nominal defocus, were aligned and averaged with the spherical harmonics alignment procedure from the PyTom toolbox (Chen et al., 2013) without imposing any symmetry. In both cases a single, randomly chosen sub-tomogram served as a starting reference model for alignment and averaging. This procedure was chosen so that no prior knowledge (neither structure nor symmetry) is used in the generation of the structures. In the case of non-active CaMKIIα,

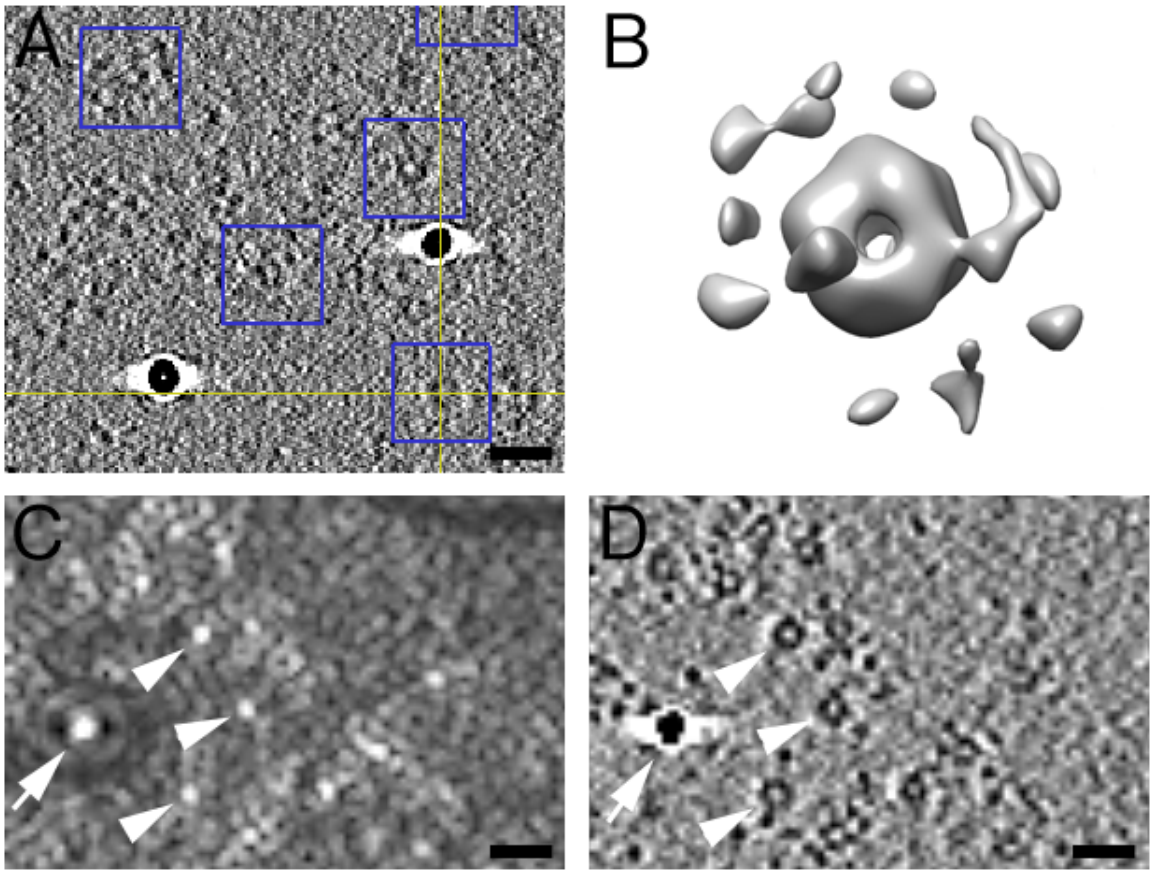

Figure 34: CaMKIIα particle picking for sub-tomogram averaging. (A) Manual particle picking with EMAN2. (B) Sub-tomogram average 259 randomly selected sub-tomograms using a single randomly selected sub-tomogram as an initial reference model. (C) Cross-correlation volume obtained by template matching with the sub-tomogram average in B as template, showing high score cross-correlation peaks for identified CaMKIIα particles (arrowheads) and Au (arrow). (D) Same slice of the original tomogram as the one showed in C with CaMKIIα particles (arrowheads) and Au (arrow). Scale bars: 20 nm.

sub-tomogram averaging and alignment of a dataset consisting of 483 sub-tomograms produced a gear-shaped structure with apparent 6-fold symmetry (Figure 35, A).

This structure resembles the gear-shaped core of the association domain that has been observed previously (Kolodziej et al., 2000; Morris and Torok, 2001) and has similar dimensions (~10 nm in diameter). In the case of activated CaMKIIα, sub-tomogram averaging and alignment of a dataset consisting of 337 sub-tomograms produced a sim-

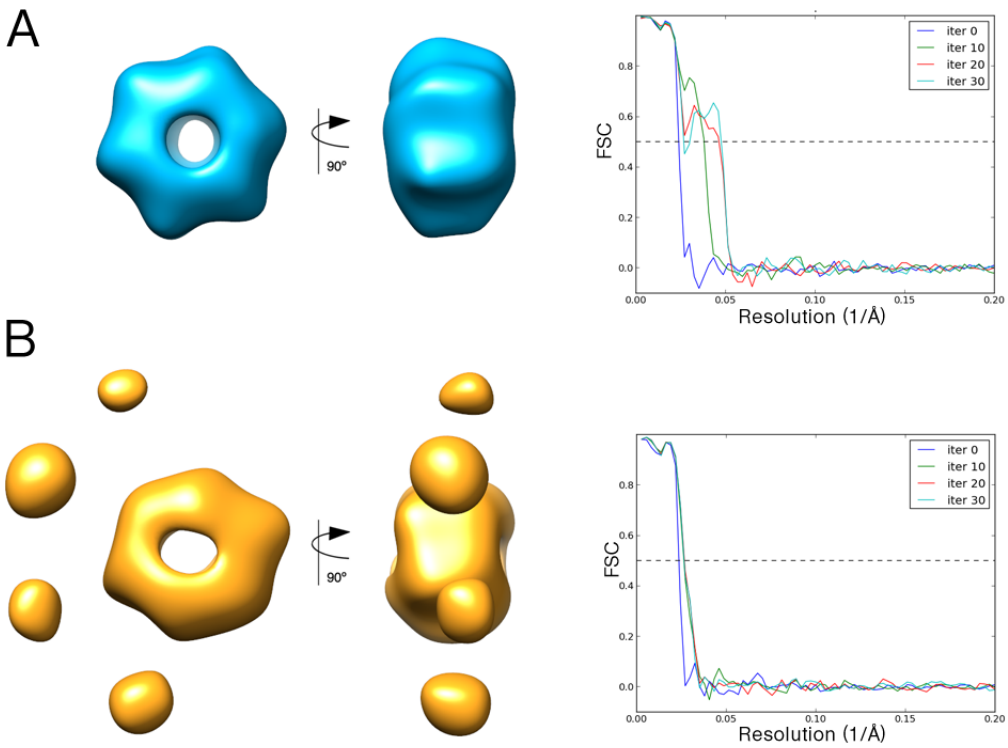

Figure 35: Sub-tomogram averaging - SPA template generation. (A) Isosurface representation of a sub-tomogam average of 483 subtomograms (@ -3.5 μn defocus) of non-active CaMKIIα after 30 averaging iterations. The reported resolution is 34.8 Å as determined by FSC with a 0.5 cutoff. (B) Isosurface representation of a sub-tomogam average of 337 subtomograms (@ -3.5 μn defocus) of activated CaMKIIα after 30 averaging iterations. The reported resolution is 34.8 Å as determined by FSC with a 0.5 cutoff.

ilar gear-shaped structure with apparent 6-fold symmetry, but with additional densities spaced at a somewhat regular distance around the structure (Figure 35, B). These additional densities are similar to the CaMKIIα kinase domains found previously to be associated with foot-like protrusions of the gear-shaped core of the association domain (Kolodziej et al., 2000). Both structures obtained by sub-tomogram averaging and alignment had a resolution of around 34.8 Å, as determined by FSC with a 0.5 cutoff (Figure 35, A and B (FSC curves)).

In an attempt to obtain better resolved structures of both non-active and activated CaMKIIα by sub-tomogram alignment and averaging, the total datasets of sub-tomograms

originating from tomograms collected at -3.5 μm nominal defocus in each case (Table 1) were aligned and averaged using the spherical harmonics alignment procedure from the PyTom toolbox (Chen et al., 2013). However, Both of the resulting reconstructions appeared very noisy (Figure 36 A and B) and their resolutions, as determined by FSC with a 0.5 cutoff, after 20 iterations appeared highly overestimated, reaching 16.1 Å in the case of non-active CaMKIIα and 12.2 Å in the case of activated CaMKIIα (Figure 36, A and B (FSC curves)). The performances of the standard real space alignment and the spherical harmonics alignment procedures from the PyTom toolbox (Hrabe et al., 2012) were compared on a small dataset of 458 activated CaMKIIα sub-tomograms. While the resulting structures were very similar in shape and resolution (40 Å), the spherical harmonics alignment procedure had a drastically shorter execution time and in view of the limited time and computational resources available at the time, sub-tomogram alignment and averaging using the standard real space procedure was not undertaken.

CTF correction was applied to the same dataset of 458 activated CaMKIIα sub-tomograms with the TOMOCTF package (Fernandez et al., 2006) in order to evaluate a potential improvement in resolution. There was a slight improvement in resolution between the non-CTF-corrected average (40.7 Å) and the CTF-corrected average corrected by phase-flipping (40.2 Å), and a further small improvement in resolution was achieved by CTF-correction by Wiener filtering (39.9 Å). These minor improvements in resolution could not justify the use of computationally intensive CTF correction on all the tomographic data and CTF correction was therefore not performed. The effects of different spherical mask sizes on the alignment and the resulting reconstruction were also shown to be negligible.

In order to get an idea about the conformational heterogeneity of the CaMKIIα holoenzymes within the activated CaMKIIα sample, sub-tomogram classification based on constrained principal component analysis (CPCA) in conjunction with k-means cluster-

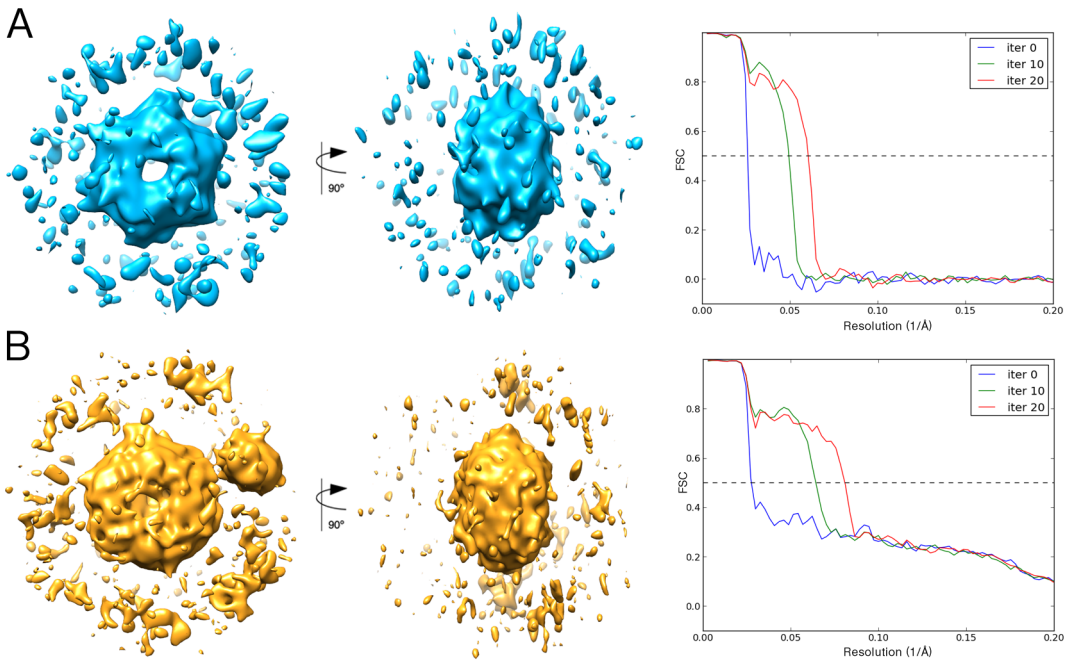

Figure 36: Sub-tomogram averaging of the total dataset of subtomograms collected at @ -3.5 μn defocus. (A) Isosurface representation of a sub-tomogam average of 1832 subtomograms of non-active CaMKIIα after 20 averaging iterations. The reported resolution is 16.1 Å as determined by FSC with a 0.5 cutoff. (B) Isosurface representation of a sub-tomogam average of 1631 subtomograms of activated CaMKIIα after 20 averaging iterations. The reported resolution is 12.1 Å as determined by FSC with a 0.5 cutoff.

ing (Forster et al., 2008) was applied on a dataset of 843 sub-tomograms of activated CaMKIIα (originating from two tomograms collected at -5.0 μm nominal defocus) and the dataset was classified into three classes. The particles in each class were realigned using the reference-free alignment and averaging procedure from the PyTom toolbox (Hrabe et al., 2012). The resulting class averages revealed a high degree of structural heterogeneity within the activated CaMKIIα sample (Figure 37).

This result suggested that classification would be a necessary step for obtaining higher resolved CaMKIIα structures and at the same time provided a possible explanation to our unsuccessful attempt to obtain better resolved structures by averaging a larger dataset of sub-tomograms. However, classifying a larger dataset would demand much higher computational resources than what was available at the time.

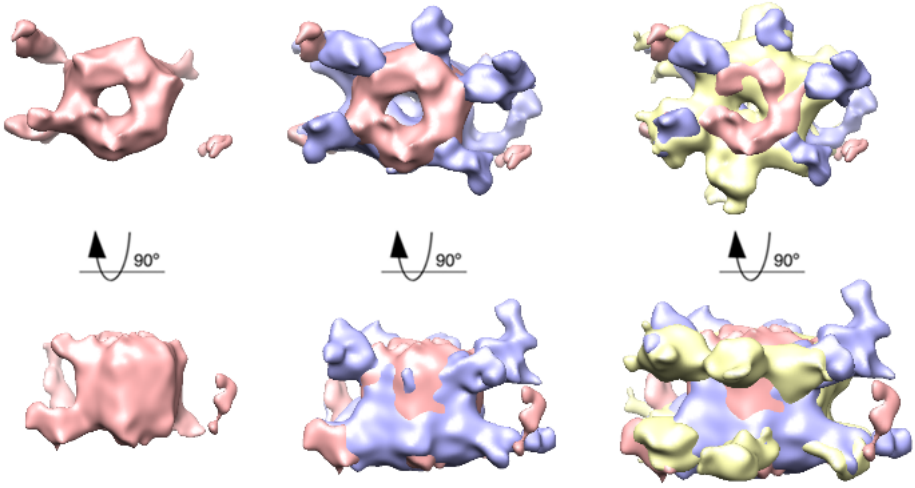

Figure 37: CPCA sub-tomogram classification. Constrained Principle Componen Classification (CPCA) in conjugation with k-means clustering with three classes on a dataset of 843 sub-tomograms (-5μm defocus) of activated CaMKIIα.

5.2.3 CaMKIIα Single Particle Analysis

Micrograph selection and particle picking A total of 12550 micrographs of vitrified non-active and activated CaMKIIα were collected on a TEM operated at 200 kV (Tecnai F20, FEI). 10-15% of the data was recorded by Oana Michalache. Each micrograph was visually evaluated for particle concentration, contamination and ice quality leaving a total of 4247 micrographs selected for further processing. Initially data collection was done at an object pixel size at the specimen level of 2.21 Å/pixel, while later on a decision was taken to increase the magnification at a resulting object pixel size at the specimen level of 1.78 Å/pixel. Initial data collection at object pixel 2.21 Å/pixel was performed only on non-active CaMKIIα, while data collection at object pixel 1.78 Å/pixel was performed on both non-active and activated CaMKIIα. This resulted in the generation of three independent datasets that in the following will be referred to as 2.21 Å/pix non-active, 1.78 Å/pix non-active and 1.78 Å/pix activated dataset, respectively. Selected micrographs were further evaluated in more detail for astigmatism and their spectral signal-to-noise ratio (SSNR) and defocus values were examined using the EMAN2 image processing suite (Tang et al., 2007). This evaluation resulted in a total

of 2749 micrographs that were selected for particle picking with defocus values ranging between -1.5 μm and -3.8 μm.

Initially, particles were picked semi-automatically using the e2boxer utility from the EMAN2 image processing suite (Tang et al., 2007). While this method of particle picking was relatively quick, the boxed particles were often either not centered or not-picked at all. Micrographs of activated CaMKIIα proved to be especially problematic in this respect. This required the additional manual repositioning of wrongly picked particles or the manual picking of additional ones. Taking into account the large number of micrographs that had to be picked, automatic particle picking seemed like a promising method. Automated particle picking was performed in batch mode using the *Gauss* convolution method from the SPARX image processing package (Hohn et al., 2007). This method proved to be very robust in picking well centered non-active and activated CaMKIIα particles automatically (Figure 38, A and B), but as expected picked both particles located in ice and those on the lacey carbon layer.

Therefore each automatically picked micrograph still had to be visually examined. Contaminants and particles on the carbon layer were manually removed using EMAN2 (Tang et al., 2007). The number of selected picked particles for each of the three data sets is summarized in (Table 2). In the case of the 1.78 Å/pix non-active and 1.78 Å/pix activated datasets, an additional selection of the best images was made on the basis of spectral signal-to-noise ratio (SSNR), using the EMAN2 software suite (Table 2).

Single Particle Analysis using EMAN2 Following the EMAN2 single particle processing workflow, automatic fitting of a theoretical CTF function to the experimental CTF function of determined from the particles in each micrograph was performed and results were manually reviewed and adjusted where needed. CTF correction (phase and amplitude correction) was then applied to each micrograph and datasets of non-CTF-corrected, and CTF-corrected boxed particles were generated for each of the three

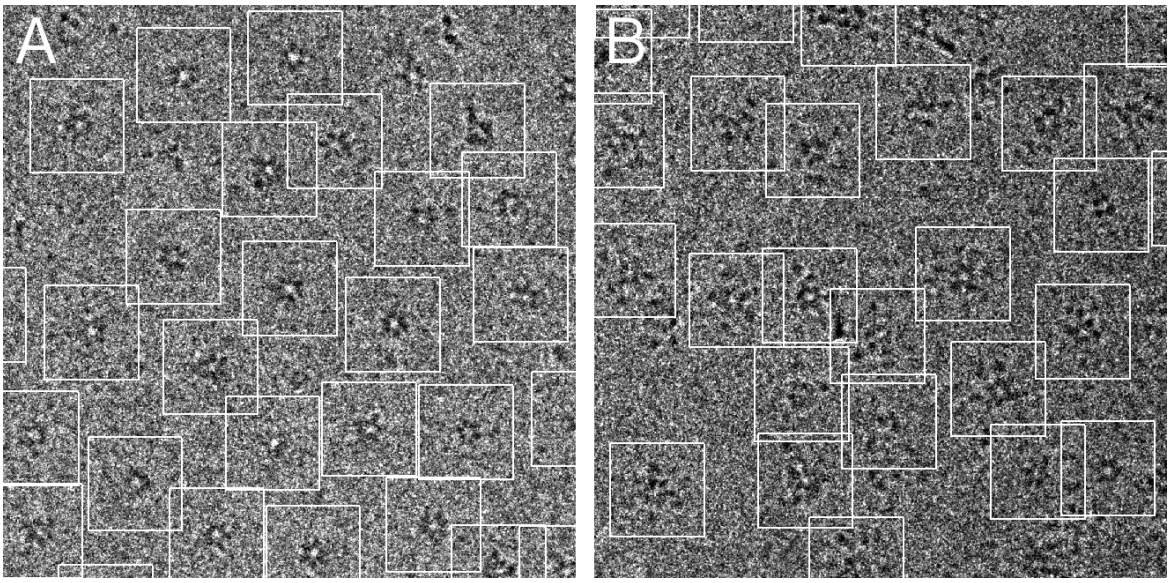

Figure 38: Automatic particle picking with SPARX. (A) A micrograph of non-active CaMKIIα with automatically picked particles (white squares). (B) A micrograph of activated CaMKIIα with automatically picked particles (white squares).

CaMKIIα datasets (2.21 Å/pix non-active, 1.78 Å/pix non-active and 1.78 Å/pix activated).

In the next step, reference free class averages were generated by 2D reference free class-averaging. This step served both as a way to examine the structural heterogeneity of the sample and as a means of removing wrongly picked particles that usually participated in bad classes (Figure 39, first column of each A and B).

Two 2D class-averaging iterations were performed on each dataset, removing bad class averages at each iteration. This resulted in a significant reduction of the total number of particles for each of the three datasets (results summarized in Table 2). Visual inspection of the reference free 2D class averages revealed, similar to the single particle tomographic data in a previous section, a gear-shaped structure with apparent 6-fold symmetry present in both non-active and activated CaMKIIα (Figure 39, last two columns of A and B). This structure again resembles the gear-shaped core of the

№of particles	Single Particle Datasets				
	2.21 Å/pix non-active Total	1.78 Å/pix non-active Total	1.78 Å/pix non-active Best	1.78 Å/pix activated Total	1.78 Å/pix activated Best
Total	119998	231391	83224	244515	214996
2D classicifation-based bad particle removal	58931	217707	80018	237529	207341

Table 2: CaMKIIα picked particles

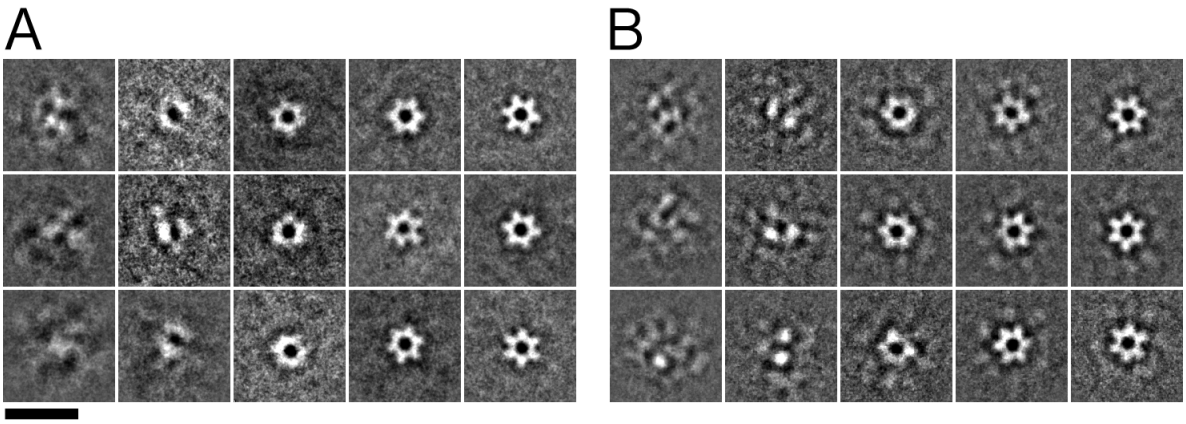

Figure 39: EMAN2 reference-free 2D class averages. (A) 2D class averages of non-active CaMKIIα showing bad class averages (first column), side views (second column), intermediate views (middle column) and top views (last two columns). (B) 2D class averages of activated CaMKIIα showing bad class averages (first column), side views (second column), intermediate views (middle column) and top views (last two columns). Scale bar: 20 nm.

central association domain that has been observed previously (Kolodziej et al., 2000; Morris and Torok, 2001) and has similar dimensions (∼10 nm in diameter). While gear-shaped 6-fold class averages, consisting of CaMKIIα top views, formed the predominant fraction of class averages, classes of side views were also present (Figure 39, second column of each A and B) and consistent with the structures obtained by single-particle tomography. Class averages of what seemed to be intermediate views were also present (Figure 39, middle column of each A and B).

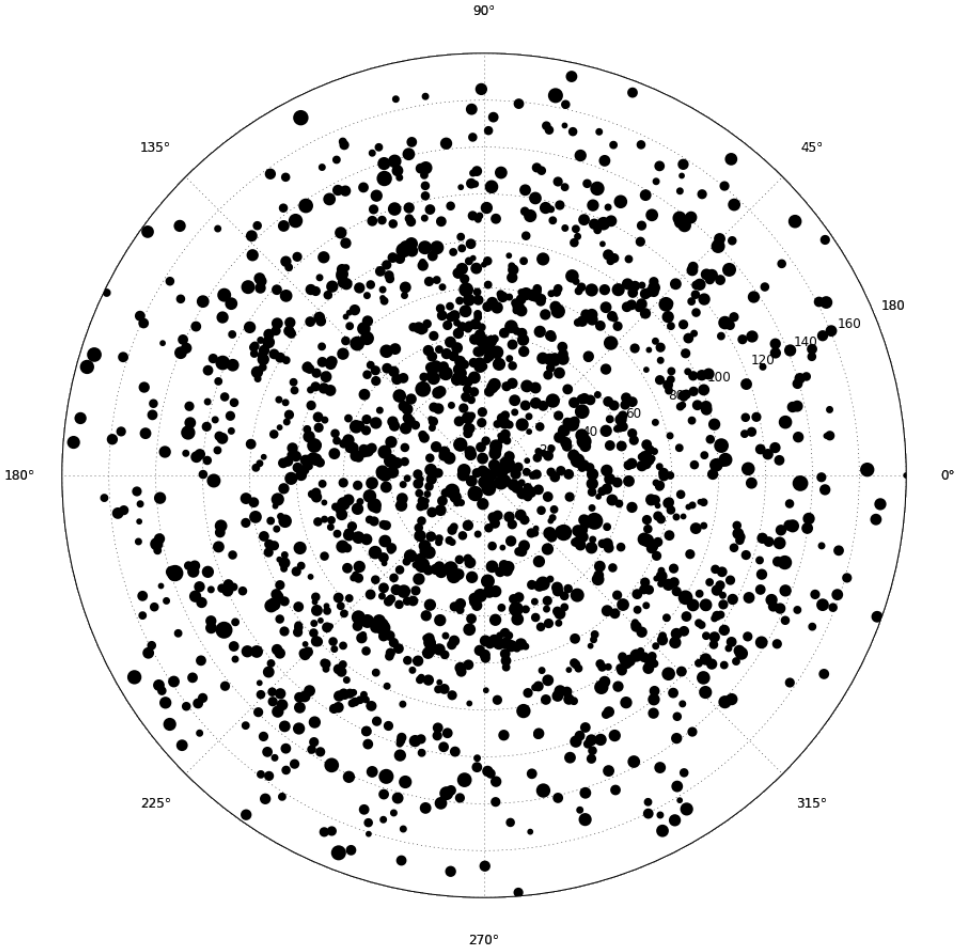

Figure 40: Angular distribution of vitrified CaMKIIα. Angular assignment of a randomly selected subset of 5000 stimulated CaMKIIα particles reconstructed with EMAN2.

Similar to the structures obtained by single-particle tomography, compared to class averages of non-active CaMKIIα, class averages of activated CaMKIIα had additional densities around the central gear-shaped association domain (Figure 39, B). These additional densities were again similar to the CaMKIIα kinase domains found previously to be associated with foot-like protrusions of the gear-shaped core of the association domain (Kolodziej et al., 2000). Since an even angular sampling is a prerequisite for obtaining higher resolution reconstructions, a small dataset of 5000 particles of stimulated CaMKIIα was selected to investigate the angular distribution of the particles within

the sample. This analysis showed a reasonably well distributed views of the holoenzyme within the sample with a slight preference for top views (Figure 40). In order to get an initial idea of the symmetry of the CaMKIIα holoenzyme, 3D refinement with no imposed symmetry was performed using the 2.21 non-active CaMKIIα dataset of 58931 particles and the structure of non-active CaMKIIα generated by single-particle sub-tomogram averaging as an initial reference model.

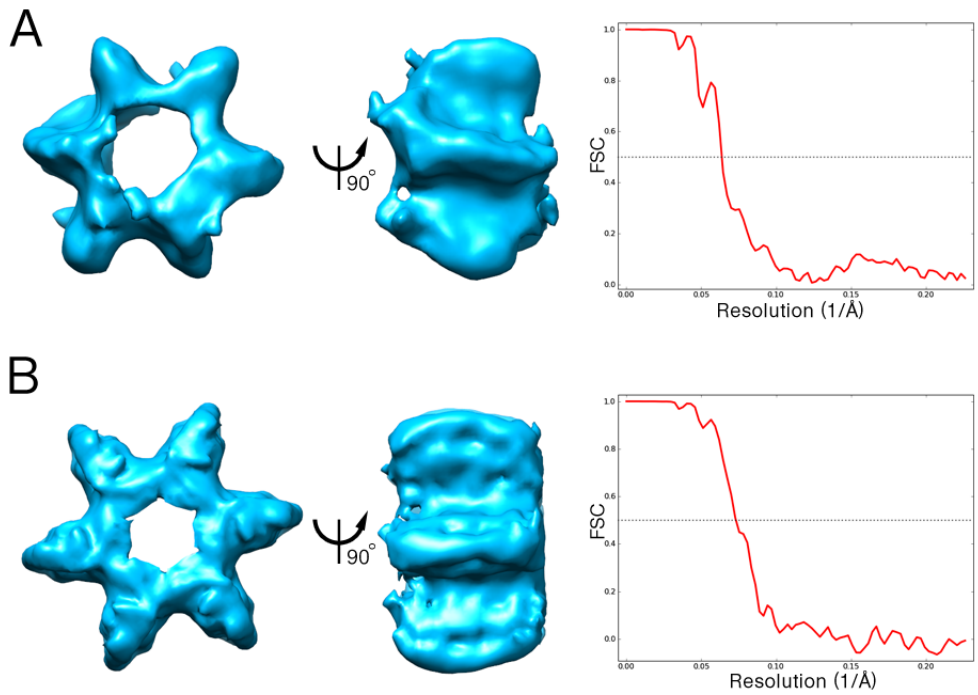

Figure 41: EMAN2 3D refinement of a single non-active CaMKIIα dataset. (A) Isosurface representation of a 3D refinement (No symmetry imposed) with a non-active CaMKIIα (2.21 Å/pix) dataset of 58931 particles, using a non-active CaMKIIα sub-tomogram average as a starting model. The reported resolution is 15.9 Å as determined by FSC with a 0.5 cutoff. (B) Isosurface representation of a 3D refinement (C6 symmetry imposed) with a non-active CaMKIIα (2.21 Å/pix) dataset of 58931 particles, using a non-active CaMKIIα sub-tomogram average as a starting model. The reported resolution is 13.8 Å as determined by FSC with a 0.5 cutoff.

As expected, 3D refinement with no imposed symmetry produced a gear shaped structure with apparent 6-fold symmetry at a resolution of 15.9 Å, as reported by standard FSC even/odd test (Figure 41, A). This observed 6-fold symmetry justified imposing 6-fold symmetry on the reconstruction. 3D refinement with the same dataset and same starting model, but imposing 6-fold (C6) symmetry produced a better resolved structure at a resolution of 13.8 Å, as reported by standard FSC even/odd test (Figure 41, B). This structure actually appeared to have a D6 symmetry (Figure 41, B), in line with previous studies (Kolodziej et al., 2000; Chao et al., 2011), and consequently, D6 symmetry was imposed in following reconstructions. 3D refinement was subsequently performed using all three datasets, imposing D6 symmetry. 3D refinement of the 2.21 non-active CaMKIIα dataset of 58931 particles with the structure of non-active CaMKIIα generated by single-particle sub-tomogram averaging as an initial reference model produced a structure at a resolution of 11.4 Å, as reported by standard FSC even/odd test (Figure 42, A), whereas 3D refinement of the 1.78 non-active CaMKIIα dataset of 80018 particles with the structure of non-active CaMKIIα generated by single-particle sub-tomogram averaging as an initial reference model produced a structure at a resolution of 10.1 Å, as reported by standard FSC even/odd test (Figure 42, B).

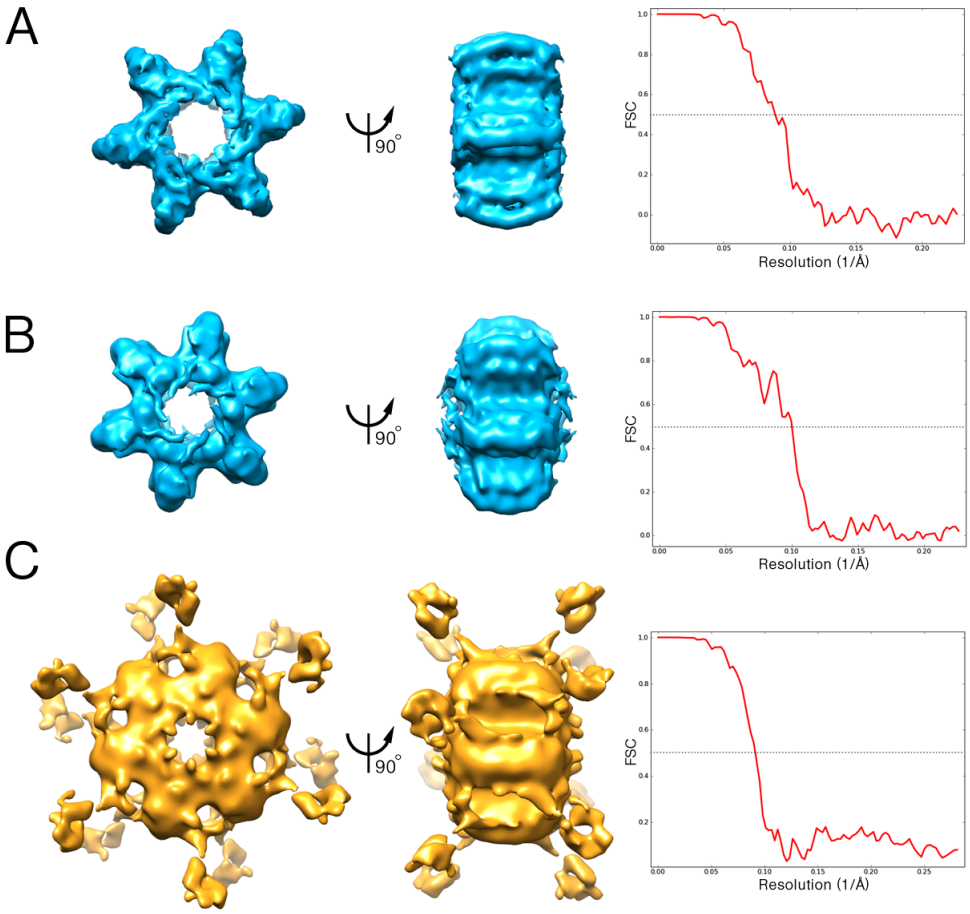

Figure 42: EMAN2 3D refinement (D6 symmetry imposed) of all three CaMKIIα datasets. (A) Isosurface representation of a 3D refinement with a non-active CaMKIIα (2.21 Å/pix) dataset of 58931 particles, using a non-active CaMKIIα sub-tomogram average as a starting model. The reported resolution is 11.4 Å as determined by FSC with a 0.5 cutoff. (B) Isosurface representation of a 3D refinement (D6 symmetry imposed) with a non-active CaMKIIα (1.78 Å/pix) dataset of 80018 particles, using a non-active CaMKIIα sub-tomogram average as a starting model. The reported resolution is 10.1 Å as determined by FSC with a 0.5 cutoff. (C) Isosurface representation of a 3D refinement (D6 symmetry imposed) with a activated CaMKIIα (1.78 Å/pix) dataset of 207341 particles, using an activated CaMKIIα sub-tomogram average as a starting model. The reported resolution is 11.1 Å as determined by FSC with a 0.5 cutoff.

Both structures had a similar appearance and resembled in shape and size the gear-shaped CaMKIIα association domain observed in previous studies (Kolodziej et al., 2000; Chao et al., 2011). Even though the reported resolution of the structure obtained from the 2.21 non-active CaMKIIα dataset was worse than the one obtained from the 1.78 non-active CaMKIIα dataset, it visually appeared somewhat better resolved (Figure 42, A and B).

In contrast to the structures obtained from both non-active CaMKIIα datasets, the structure obtained by 3D refinement of the 1.78 activated CaMKIIα dataset of 207341 particles with the structure of activated CaMKIIα generated by single-particle sub-tomogram averaging as an initial reference model produced a structure at a resolution of 11.1 Å, as reported by standard FSC even/odd test (Figure 42, C), that in addition to the gear-shaped CaMKIIα association domain displayed foot-like protrusions, extending above and below the midplane of the association domain. These protrusions are similar to the CaMKIIα kinase domains found previously to be associated with foot-like protrusions of the gear-shaped core of the association domain (Kolodziej et al., 2000).

In order to exclude the possibility of the reconstructions being influenced by the choice of initial reference model, the initial models were swapped so that a structure of activated CaMKIIα, obtained by single-particle sub-tomogram averaging, was used as an initial reference model in a 3D refinement of an non-active CaMKIIα single particle dataset and vice versa. 3D refinement of the 2.21 non-active CaMKIIα dataset of 58931 particles with the structure of activated CaMKIIα, generated by single-particle sub-tomogram averaging, as an initial reference model produced a structure at a resolution of 12.7 Å, as reported by standard FSC even/odd test (Figure 43, A). Even though activated CaMKIIα was used as an initial model, the resulting structure displayed similar structural features to those of the structure obtained from the same dataset with non-active CaMKIIα used as initial model (Figure 42, A), namely a gear-shaped structure with no

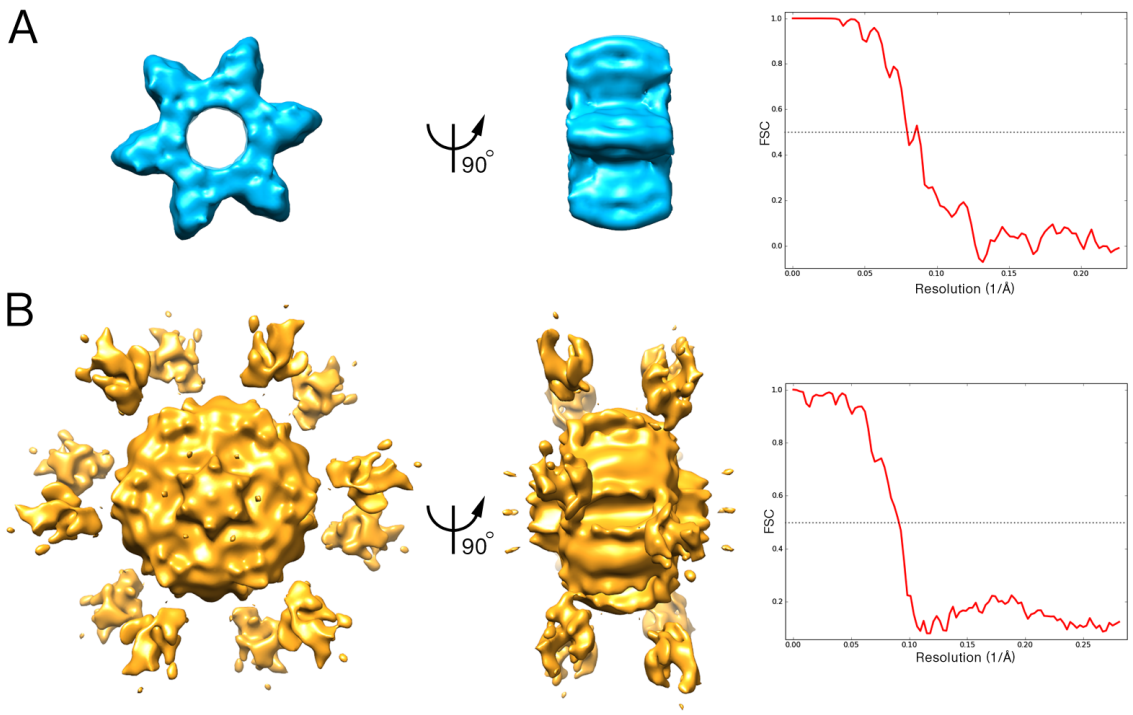

Figure 43: EMAN2 3D refinement with inverted templates. (A) Isosurface representation of a 3D refinement (D6 symmetry imposed) with a non-active CaMKIIα (2.21 Å/pix) dataset of 58931 particles, using an activated CaMKIIα sub-tomogram average as a starting model. The reported resolution is 12.7 Å as determined by FSC with a 0.5 cutoff. (B) Isosurface representation of a 3D refinement (D6 symmetry imposed) with a activated CaMKIIα (1.78 Å/pix) dataset of 207341 particles, using an non-active CaMKIIα sub-tomogram average as a starting model. The reported resolution is 11.1 Å as determined by FSC with a 0.5 cutoff.

protrusions. Similarly, 3D refinement of the 1.78 activated CaMKIIα dataset of 207341 particles with the structure of non-active CaMKIIα, generated by single-particle sub-tomogram averaging, as an initial reference model produced a structure at a resolution of 11.1 Å, as reported by standard FSC even/odd test (Figure 43, B) that displayed similar structural features to those of the structure obtained from the same dataset with activated CaMKIIα used as initial model (Figure 42, C). Both structures displayed foot-like protrusions extending above and below the midplane of the association domain, with the protrusions being closer to the midplane in the case where a non-active CaMKIIα initial model was used. Therefore, the existence of protrusions is not a consequence of a particular choice of the initial model.

All together, these observations indicate that the foot-like protrusions observed for activated CaMKII constitute the main difference between the structures of non-active and activated CaMKIIα. Furthermore, considering that the kinase domains are less well-resolved than the association domains, and that they have similar mass, it is likely that the kinase domains are quite flexible.

Single Particle Analysis using RELION In order to confirm that our results were not influenced by the choice of reconstruction software and in order to get more information about the conformational heterogeneity, single particle analysis was also performed with the RELION software package (Scheres, 2012). In addition to 2D class averaging and 3D refinement capabilities, present in EMAN2, RELION provides an unsupervised 3D classification approach based on maximum-likelihood, which makes it a tool well suited for the classification of structurally heterogeneous data.

Particle coordinates from all three single particles datasets (Table 2, Total), automatically picked with SPARX, as explained in section 5.2.3, were imported into RELION for preprocessing. Since RELION doesnt have its own CTF determination functionality, CTFFIND3 (Mindell and Grigorieff, 2003) was used to estimate CTF parameters for each micrograph, after which particles were extracted and normalized. Judging by the comparison of theoretical and experimental power spectra, CTFFIND3 in general performed better in CTF fitting than EMAN2.

Reference free 2D class averages were generated by RELION's maximum-likelihood based 2D reference-free class-averaging procedure. This step again served both as a way to examine the structural heterogeneity of the sample and as a means of removing wrongly picked particles that usually participated in bad classes (Figure 44, first column of each A and B). The resulting class averages (Figure 44, A and B) looked better resolved compared to the ones generated by EMAN2 (Figure 39, A and B).

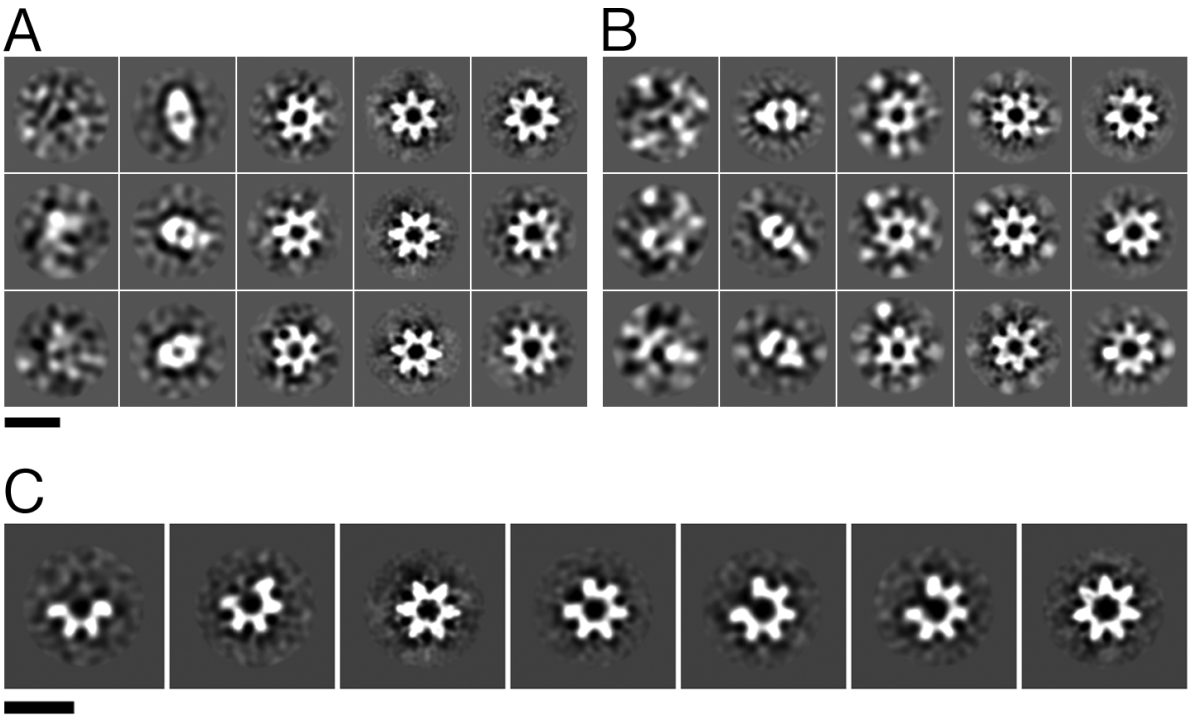

Figure 44: RELION reference-free 2D class averages. (A) 2D class averages of non-active CaMKIIα showing bad class averages (first column), side views (second column), intermediate views (middle column), top views (fourth column) and 7-fold symmetrical top views (last column). (B) 2D class averages of activated CaMKIIα showing bad class averages (first column), side views (second column), intermediate views (middle column), top views (fourth column) and 7-fold symmetrical top views (last column). (C) 2D class averages of intermediate views of the CaMKIIα association domain

Interestingly, while most of the top-view class averages displayed a 6-fold symmetry (Figure 44, 3rd and 4th columns in A and B), some top-view class averages clearly had a 7-fold symmetry (Figure 44, 5th columns in A and B) and were characterized by an increased association domain and central hole diameter, compared to 6-fold symmetrical ones. These 7-fold symmetrical holoenzymes seemingly result from the incorporation of an additional CaMKII subunit into each stacked association domain ring. This observation is quite surprising, since to our knowledge 7-fold symmetrical CaMKII association domains have only been observed in preparations of truncated association domains lacking the kinase domains (Rosenberg et al., 2006). Since no 7-fold class averages were ob-

served in the case of 2D classification done with EMAN2, obtaining 7-fold class averages with RELION was a clear indication that its 2D classification capability was superior and better adept in dealing with datasets displaying a high degree of structural heterogeneity. In addition to 2D class averages of 7-fold symmetrical CaMKIIα association domains, it was possible to identify class averages of different structural states of the association domain (Figure 44, C). The finding that holoenzymes displaying different structural states of their association domain and 7-fold symmetrical holoenzymes are also present in the sample showed that an additional level of structural heterogeneity exists in the data.

Similarly to what was done by EMAN2, two 2D class-averaging iterations were performed on each dataset, removing bad class averages at each iteration. In this case, however, the presence of classes of CaMKII top views displaying a 7-fold symmetry required the further separation of good particles into subsets of particles displaying either 6-fold or 7-fold symmetry alone. This separation was done by sorting-out the 2D class averages displaying a 7-fold symmetry from those displaying a 6-fold symmetry into separate subsets (results summarized in Table 3). Using 2D classification for this separation has the drawback that only top views of CaMKII holoenzymes displaying a 7-fold symmetry are easily identifiable, which could easily leave many side views of 7-fold symmetrical CaMKII holoenzymes in the 6-fold symmetrical subsets. A general 3D processing RELION workflow was established and applied to all three CaMKIIα datasets (2.21 Å/pix non-active, 1.78 Å/pix non-active and 1.78 Å/pix activated) (Figure 45). As the first step 3D classification with no imposed symmetry was performed on all three datasets with the goal of separating 3D classes of 6-fold symmetrical holoenzymes from those of 7-fold symmetrical ones. The fraction of particles identified as 7-fold symmetrical by 2D classification ranged from 2.63% to 11.98% in the different datasets (Table 3) and the number of classes used for 3D classification was chosen accordingly in order to obtain an adequate class oversampling (10-30). For all three datasets, 3D

№of particles	Single Particle Datasets				
	2.21 Å/pix non-active Total	1.78 Å/pix non-active Total	1.78 Å/pix non-active Best	1.78 Å/pix activated Total	1.78 Å/pix activated Best
Total	119998	231391	83224	244515	214996
6-fold/7-fold after 2D classification	68817	-	51787	-	97665
6-fold after 2D classification	60570	-	48248	-	95089
6-fold after 3D classification	55713	-	45173	-	92836
7-fold after 3D classification	8247	-	3539	-	2576

Table 3: CaMKIIα picked particles - RELION

RELION 3D processing workflow

1) 3D Classification of 6-fold/7-fold (after 2D class.) particles (no imposed symmetry):
   Goal: get rid of particles displaying 7-fold symmetry and obtain a dataset consisting of 6-fold symmetrical particles alone (6-fold after 3D class.)

2) 3D Refinement of 6-fold+7-fold (after 2D class.), 6-fold (after 2D class.) and particles identified as having a 6-fold symmetry in Step 1 (6-fold (after 3D class.), imposing a D6 symmetry:
   Goal: identify the "best" 6-fold dataset

3) 3D Classification of "best" dataset identified in Step 2, imposing a D6 symmetry:
   Goal: resolve the heterogeneity within the 6-fold particles

4) 3D Refinement of best classes identified in Step 3:
   Goal: obtain best 3D structure model of CaMKIIα

Figure 45: RELION single particle processing workflow.

classification resulted in a number of classes displaying 6-fold symmetry and a single class displaying a 7-fold symmetry (Figure 46). While in the case of the 2.21 Å/pix non-active dataset, all subunits of the 7-fold symmetrical class were clearly resolved, a single CaMKII subunit of the 7-fold symmetrical class in each of the 1.78 Å/pix datasets displayed a very weak contrast. The percentage of particles switching classes during 3D

classification was monitored in each run. 3D classification iterations were performed until only 5%-10% of the particles were switching classes.

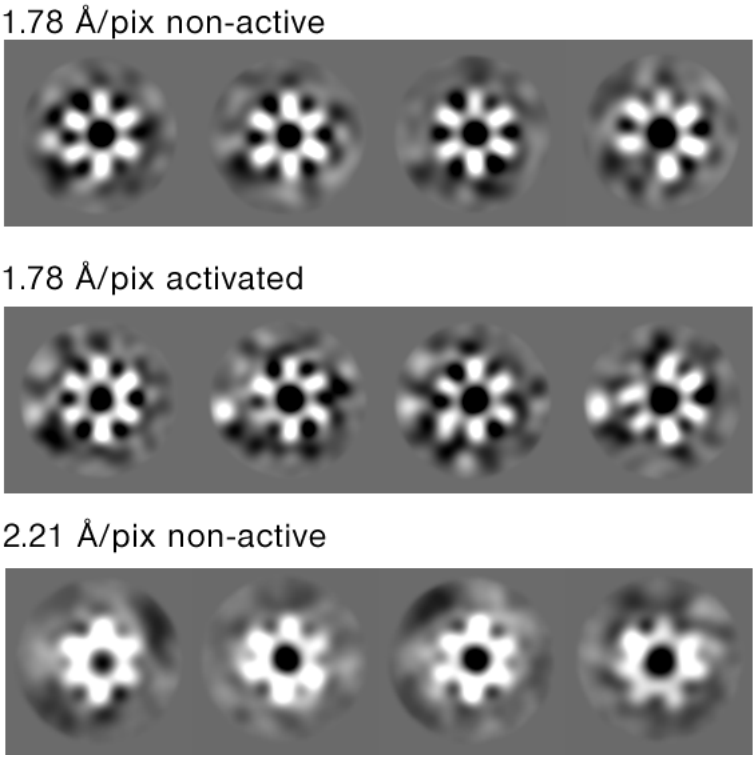

Figure 46: RELION 3D classification with no imposed symmetry. (A) 3D class averages of a non-active CaMKIIα (1.78 Å/pix) dataset consisting of 51787 particles. First three classes show a clear 6-fold symmetry while the class on the right shows a 7-fold symmetry with a single subumit displaying a very weak contrast or missing. (B) 3D class averages of an activated CaMKIIα (1.78 Å/pix) dataset consisting of 97665 particles. First three classes show a clear 6-fold symmetry while the class on the right shows a 7-fold symmetry with a single subumit displaying a very weak contrast. (C) 3D class averages of a non-active CaMKIIα (2.21 Å/pix) dataset consisting of 68817 particles. First three classes show a clear 6-fold symmetry while the class on the right shows a 7-fold symmetry. In all cases equatorial slices are shown.

In order to identify the best dataset for further processing, 3D refinement was performed with all three CaMKIIα datasets (2.21 Å/pix non-active, 1.78 Å/pix non-active and 1.78 Å/pix activated) and for each dataset using the mixed subset of 7-fold and 6-fold symmetrical particles and the two subsets consisting of 6-fold symmetrical particles, identified either by 2D or 3D classification (Table 3). In the cases of both 1.78 Å/pix

datasets, the best-resolved structures were obtained with the subsets consisting of 3D classified, 6-fold symmetrical particles. While these structures were still only slightly better-resolved than the ones obtained with subsets consisting of 2D classified, 6-fold symmetrical particles, they were obtained with a smaller number of particles (Table 3). This was an indication that 3D classification is at least slightly better at separating 6-fold from 7-fold symmetrical particles than 2D classification. Surprisingly, in the case of the 2.21 Å dataset the best-resolved structure was obtained with the mixed subset of 7-fold and 6-fold symmetrical particles (Figure 47).

The subsets from which the best-resolved structures were obtained in each case were subjected to 3D classification with imposed 6-fold symmetry using 10 classes (Figure 48). This step had the goal of further excluding the particles displaying high structural heterogeneity. Different particle subsets were created for each dataset by picking one or combining different classes displaying similar structural features. 3D refinements were performed with each particle subset.

The best resolved structures of non-active and activated CaMKIIα displayed a significant difference between each other (Figure 49, A). Similar to the 3D reconstructions done with EMAN2, the structure of activated CaMKIIα displayed foot-like protrusions extending above and below the midplane of the association domain (Figure 49, A (lower row)), while in the case of non-active CaMKIIα, these protrusions were absent or very faint (Figure 49, A (upper row)).

The resolutions of these structures were 9.6 Å (non-active) and 8.9 Å (activated), as determined by RELION's "gold-standard" FSC (where particles are split in two sets that are then reconstructed completely separately and combined in the final reconstruction iteration). However, the resolution of the em density maps of the best-resolved structures of activated and non-active CaMKIIα could be estimated by visual appearance to

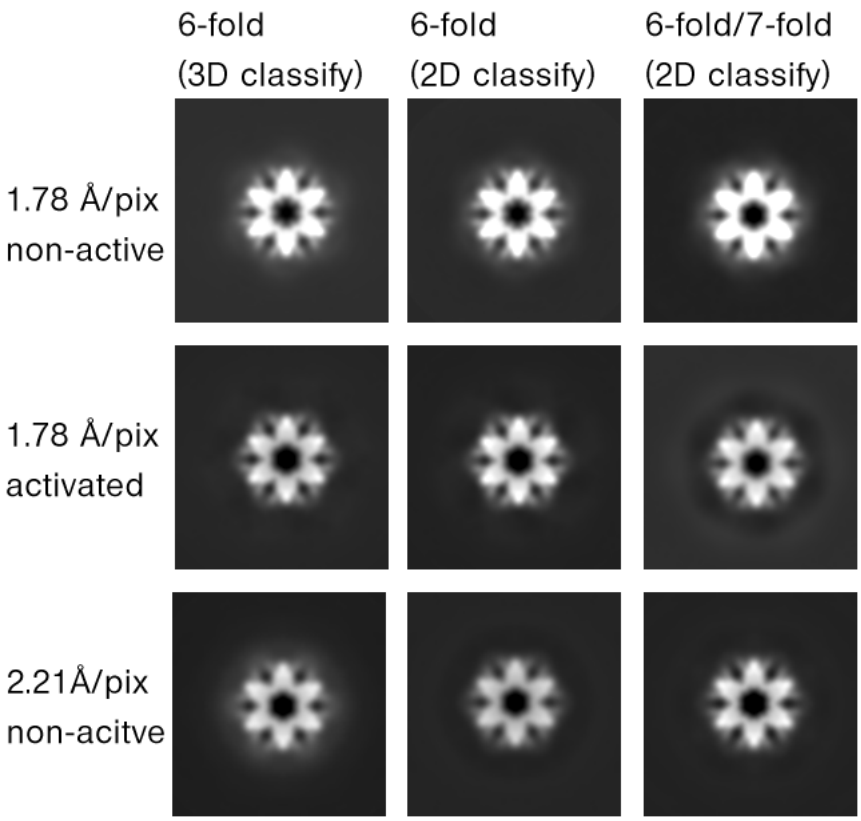

Figure 47: RELION - best dataset identification. 3D refinement with imposed D6 symmetry on the corresponding datasets in Table 3 in order to identify the best dataset for further processing. In all cases equatorial slices are shown.

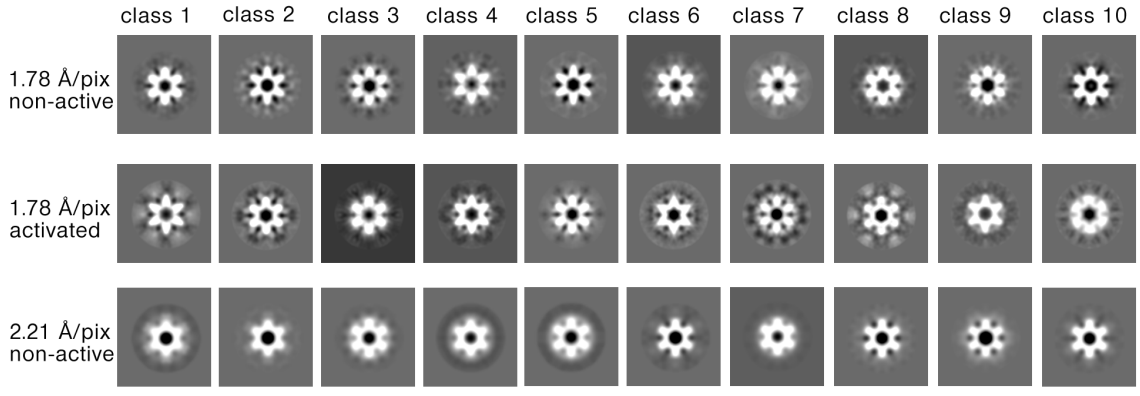

Figure 48: RELION 3D classification with imposed D6 symmetry. 3D classification with the goal of excluding particles displaying high structural henerogeneity. In all cases equatorial slices are shown.

be around 20 Å in both cases (Figure 53). In order to obtain an independent resolution estimate, we proceeded to adapt currently available X-ray crystallography structures.

Recently, X-ray structure of inhibited, full-length human CaMKIIα construct with a very short CaMKIIβ7 (an alternative splicing variant of human CaMKIIβ) linker was published. This X-ray structure has a cylindrical height of approximately 100 Å and a diameter of approximately 150 Å, and will be referred to here as the CaMKIIβ7. The central association domain of this structure is formed by two stacked hexameric rings of association domain subunits and the kinase domains are positioned between two such association domain subunits (Figure 50, A). While the association domain of constructs used here and of the CaMKIIβ7 are essentially the same, their other domains differ. Namely, The CaMKIIα construct used in this work has a 30 residue long linker region while in the CaMKIIβ7 construct, this linker region is basically missing (Figure 51). Due to the missing linker and the inhibited form, the kinase domains of CaMKIIβ7 are tightly packed against the association domain, thus severely reducing their degrees of freedom. As a consequence, part of the regulatory segment, including Thr305 and Thr306 which are located at the calmodulin-binding region, is squeezed between the kinase domain and the association domain, making it somewhat inaccessible to calmodulin (Figure 50, B). Therefore , the linker and the kinase domains of the CaMKIIβ7 X-ray crystal structure and the EM models obtained here are expected to have a very different location.

We computationally removed the residues of the kinase domains from the CaMKIIβ7 structure (residues 1-312), in order to obtain an atomic model of the CaMKIIα association domain. Rigid-body fitting of this structure into the EM density map of activated CaMKIIα, revealed the positions of the alpha helices to which the kinase domains are attached by flexible linkers (Figure 49, B).

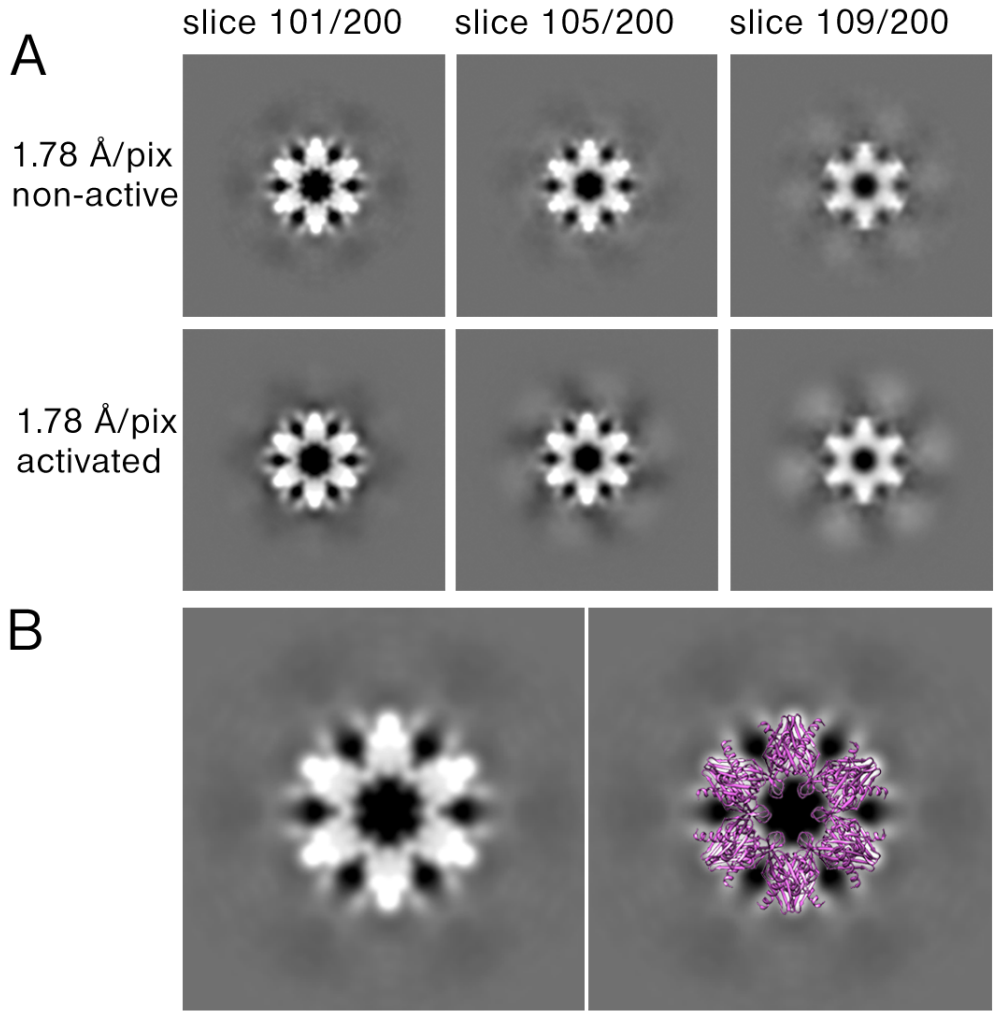

Figure 49: RELION 3D Refinement of the identified best datasets of both active and non-activated CaMKIIα. (A) Comparison between the 3D refinements of the best datasets of non-active and activated CaMKIIα. Three x-y slices through the 3D reconstructions are presented. The structure of activated CaMKIIα shows foot-like protrusions extending above and below the midplain of the association domain. (B) Rigid body fitting of the crystal structure of Human CaMKKIα into the association domain of the best-resolved structure of activated CaMKIIα.

The CaMKIIα construct used in this work and the *C.Elegans* CaMKII share a high degree of sequence similarity ($\sim$70%) and linker regions of comparable size (Figure 51) and are therefore expected to also share a high degree of structural similarity and a similar holoenzyme architecture. An X-ray structure of the kinase and regulatory

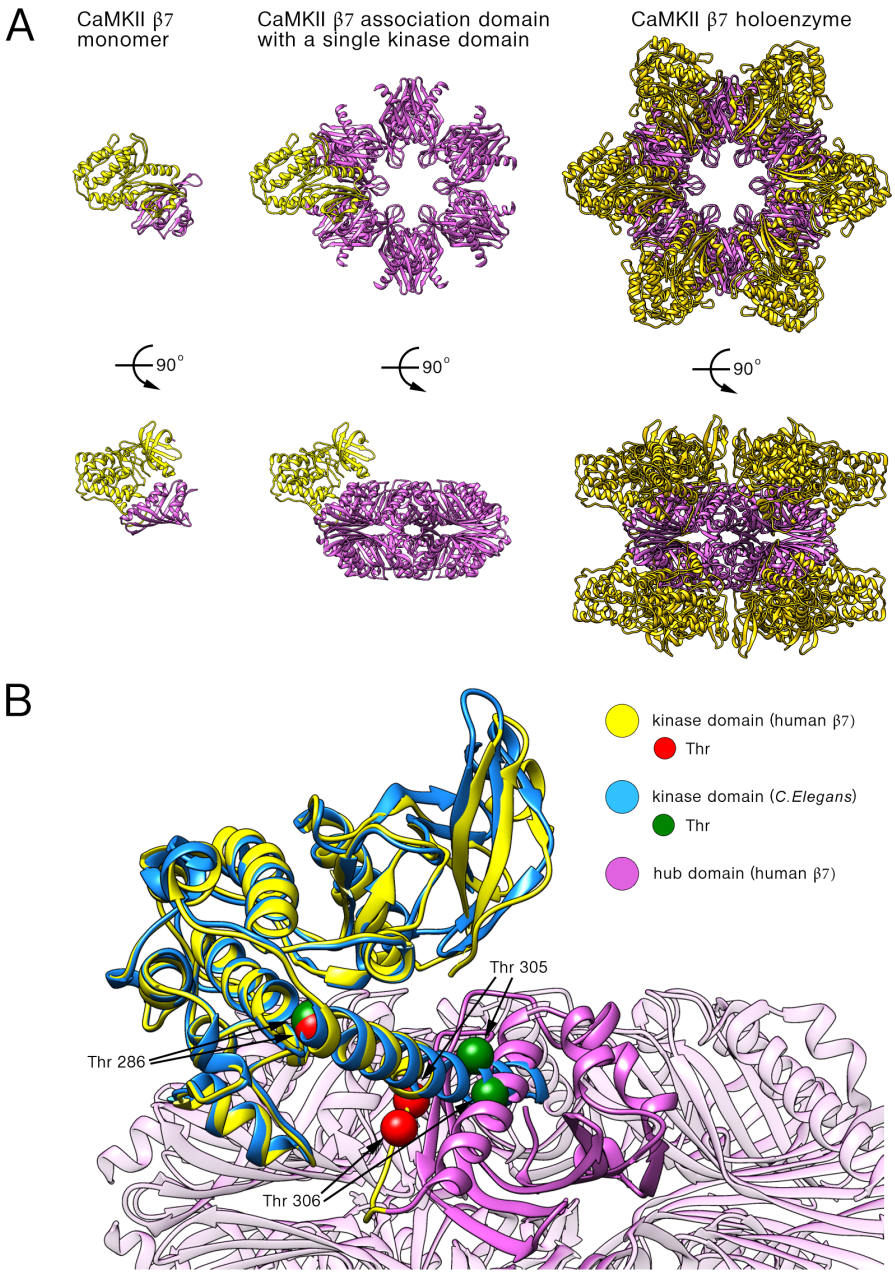

Figure 50: CaMKII holoenzyme architecture. (A) The architecture of the CaMKIIβ7 short linker holoenzyme (pdb id: 3SOA). (B) Superposition of the C.Elegans CaMKII kinase domain (pdb id: 2BDW) over the CaMKIIβ7 short linker kinase domain (pdb id: 3SOA).

domains (residues 1340) of an autoinhibited *C.Elegans* CaMKII has been solved previously (Rosenberg et al., 2005). The crystallized *C.Elegans* fragment is 77% identical in sequence to the corresponding region of the CaMKIIα construct used in this

work. The asymmetric unit of this crystal contained a dimer of CaMKII kinase domains with the long helices of the regulatory segments of each subunit forming a coiled-coil structure (Figure 27, A (encircled in red)). Superimposing the X-ray structure of the *C.Elegans* CaMKII kinase and regulatory domains (single CaMKII kinase domain) over the CaMKIIβ7 kinase domain revealed a good overall correspondence between the two structures, except for the C-terminal region, where a long alpha helix formed by the regulatory segment in the *C.Elegans* structure clashes with an alpha helix of the CaMKIIβ7 short linker association domain (Figure 50, B). Therefore, the kinase and regulatory domains of CaMKIIα have to be positioned further away from the association domain.

Interestingly, this superposition of the two crystal structures indicated that the coiled coil seen in the *C.Elegans* kinase domain dimer crystal structure is incompatible with the structural organization of the CaMKIIβ7 holoenzyme, implying that the CaMKII holoenzyme model suggested previously by the same group and used initially in this study to produce templates for template matching (Rosenberg et al., 2005) (Figure 27) is inaccurate.

Resolution of the reconstructions was estimated by FSC of the em maps with a density simulated from the X-ray structure of the CaMKIIα associated domain (cross-resolution). A soft mask encapsulating the association domain in the em maps was used to ensure that only the association domain is being correlated. In the case of both activated and non-active CaMKIIα structures, cross-resolution gave a resolution estimate of around 20 Å, consistent with the visual impression (Figure 53).

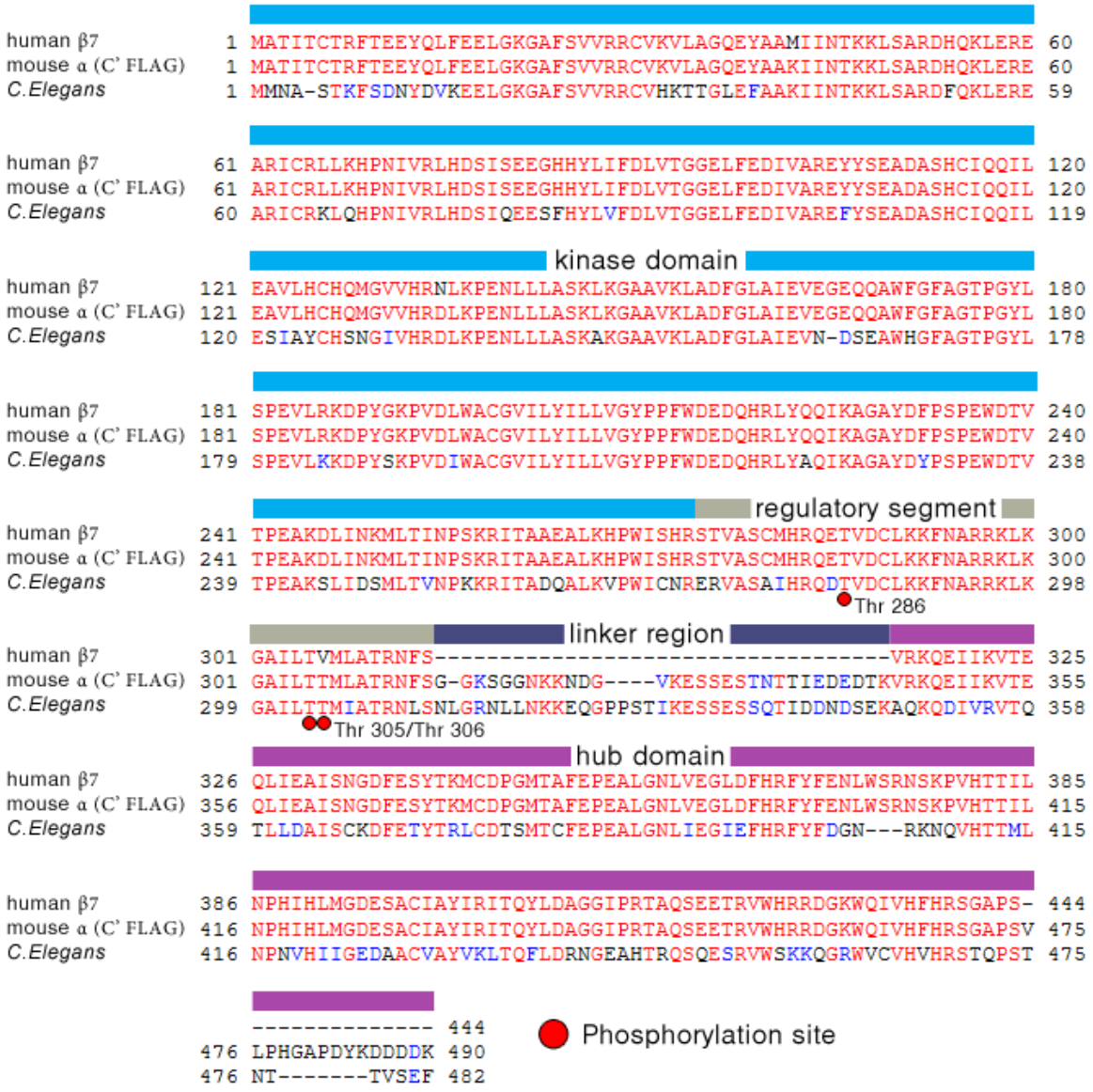

Figure 51: Sequence alignment between *C.Elegans* CaMKII (UNC-43), C-terminal FLAG tag mouse CaMKIIα used in this study and CaMKIIβ7 short linker construct (Chao et al., 2011).

In order to build a pseudo-atomic model of the complete CaMKIIα holoenzyme, we fitted the atomic model of the association domain into the superimposed em density maps of the best-resolved structures of activated and non-active CaMKIIα and positioned the X-ray structure of the *C.Elegans* CaMKII kinase domains within the foot-like protrusions of the em density maps (Figure 52, A). In contrast to the CaMKIIβ7 structure,

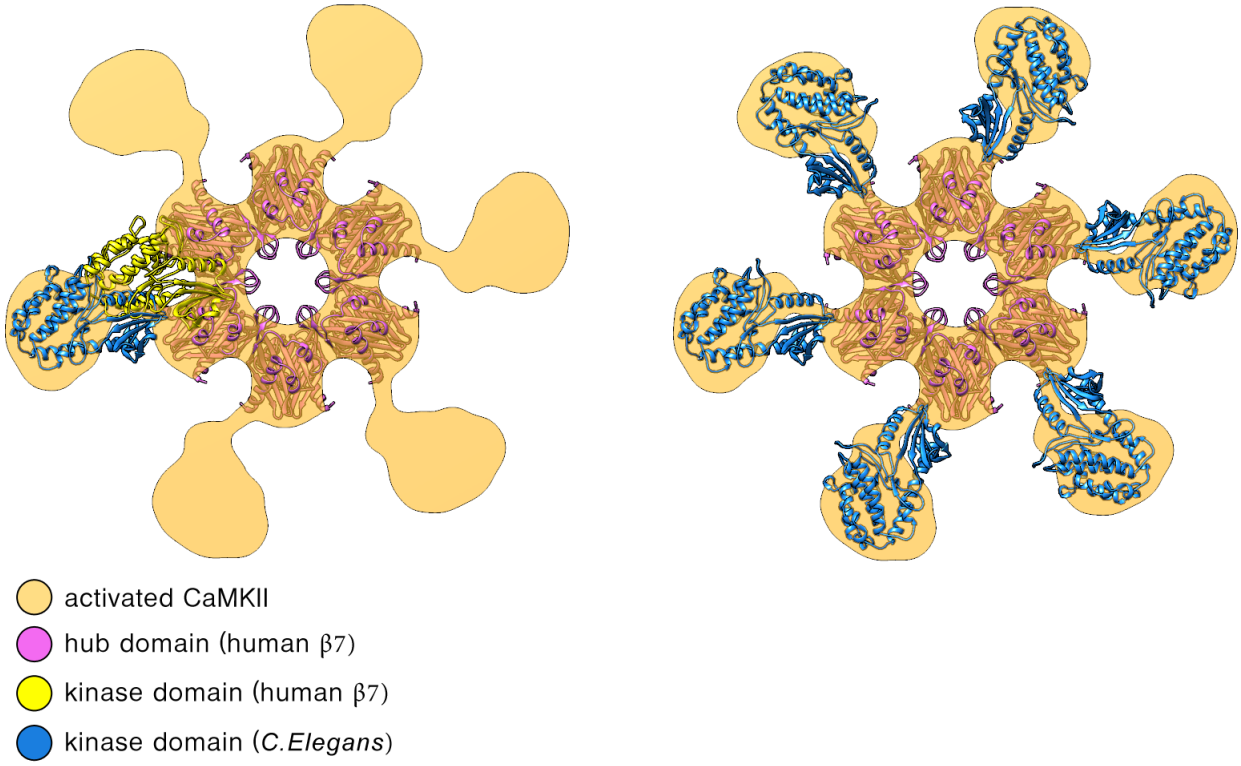

Figure 52: Building a pseudo-atomic model of the CaMKIIα holoenzyme. Positioning the C.Elegans CaMKII kinase domain (pdb id: 2BDW) within the foot-like protrusions of the best-resolved EM density map of activated CaMKIIα in order to generate a model of the CaMKIIα holoenzyme. Only a single slice of the EM density map is shown for simplicity.

which has a diameter of approximately 150 Å, the pseudo-atomic model of the CaMKIIα holoenzyme has a diameter of approximately 200 Å, while the kinase domains in both structures are located at similar elevations above and below the midplane of the association domain (Figure 54).

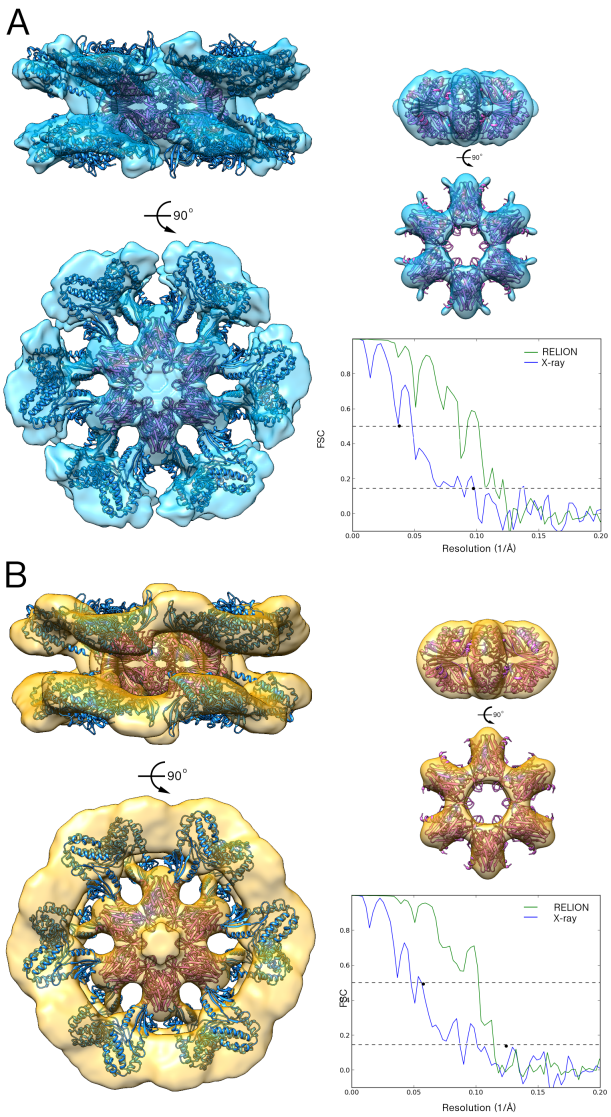

Figure 53: Comparison between the em density maps and the atomic models of CaMKII. (A) left: The newly generated CaMKIIα holoenzyme fitted within the best-resolved EM density map of non-active CaMKIIα. right: CaMKIIα association domain X-ray structure fitted within the best-resolved EM density map of non-active CaMKIIα and FSC curves from RELION's "gold standard" FSC and cross-resolution with the X-ray structure. (B) left: The newly generated CaMKIIα holoenzyme fitted within the best-resolved EM density map of activated CaMKIIα. right: CaMKIIα association domain X-ray structure fitted within the best-resolved EM density map of activated CaMKIIα and FSC curves from RELION's "gold standard" FSC and cross-resolution with the X-ray structure

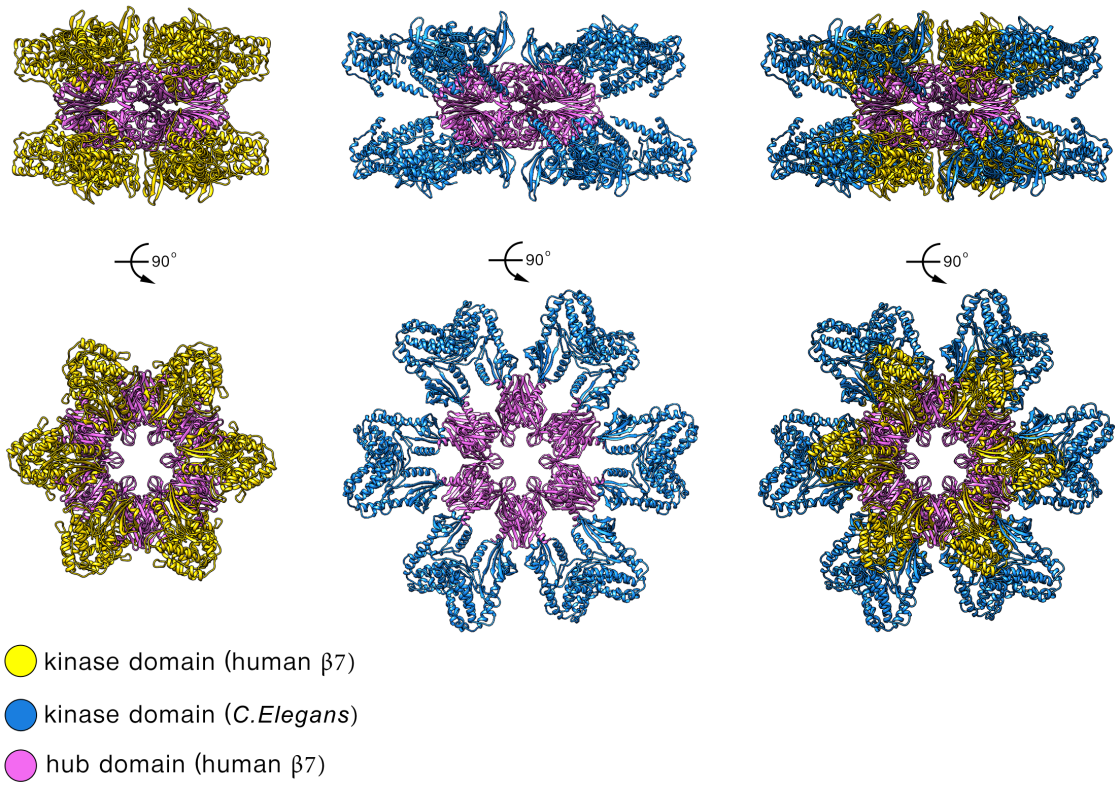

Figure 54: Pseudo-atomic CaMKIIα holoenzyme model. The newly generated CaMKIIα holoenzyme model (center) compared to the X-ray structure of CaMKIIβ7 (left) and a superposition of both structures (right).

6 Discussion

The PSD is a large and complex molecular machine consisting of hundreds of distinct proteins. It clusters neurotransmitter receptors on the postsynaptic membrane and regulates the network of postsynaptic signaling molecules. By doing so it controls the strength of synaptic signaling and plays a major role in synaptic plasticity. Its structure and protein composition are dynamic and can be modified by external stimuli and synaptic activity (Sheng and Hoogenraad, 2007). This makes attempts to describe the structural rearrangements of its components very challenging. One way to gain an understanding on postsynaptic signaling is to unravel the structures and physical interconnections of the proteins in the PSD. Although a number of EM studies (Kharazia and Weinberg, 1997; Racca et al., 2000; Petersen et al., 2003; Chen et al., 2008; Swulius et al., 2010; Chen et al., 2011; Fera et al., 2012) have provided some insights on the postsynaptic structural organization, the use of conventional EM sample preparation techniques in these studies, known to introduce a number of artifacts, poses questions on the extent of structural preservation. Furthermore, the method employed to visualize and quantify proteins in most of these studies was immuno-gold labeling, known to be heavily dependent on antibody efficiency and prone to missing certain internalized epitopes. Therefore, further work is needed to shed light on the precise supramolecular organization of the PSD.

We employed Cryo-EM to study the supramolecular architecture of the PSD and to identify some of the synaptic molecular complexes within its structure. Unlike conventional EM sample preparation techniques that are known to introduce a number of artifacts, vitrification ensures the faithful preservation of biological structures in close to native form and is a prerequisite for studies aiming at molecular resolution. The PSD was imaged both enclosed in the postsynaptic terminal of synaptosomes and isolated

by detergent extraction with Triton X-100 (PSD fraction). While synaptosomes provided a model system where the PSD is in a native-like environment, attached to the postsynaptic membrane and still in contact with the actin cytoskeleton, isolated PSDs offered the unique opportunity of imaging them from an en face view and at a higher resolution. EM grids of vitrified PSDs had in general thinner ice regions than those of synaptosomes and allowed recording of cryo-tomograms of higher signal-to-noise ratio (SNR).

CaMKII was identified as the primary molecular target for detection because of the following reasons: (i) its functional significance as a major regulator of synaptic function and plasticity, (ii) its ability to undergo autophosphorylation and translocation to the PSD in response to synaptic stimulation, (iii) the relatively large size of the holoenzyme it forms (∼650 kDa) and (iv) its high abundance in the PSD.

Because a number of structural studies in the literature have produced highly diverging views of the CaMKII holoenzyme structure and because no structure existed for the activated state of CaMKII, a part of this work was to obtain the structures of both activated and non-active CaMKII by Cryo-EM single particle analysis.

6.1 Pharmacological stimulation of synaptosomes causes CaMKII translocation and increase of Thr286 autophosphorylation

Our first task was to identify a pharmacological treatment that stimulates synaptosomes, affects CaMKII and the PSD in a way that is physiological and that can be detected. We reasoned that such treatment should induce changes in the phosphorylation state of CaMKII and possibly its localization, so that these changes could be detected by template matching with structures of phosphorylated and non-phosphorylated CaMKII.

We applied an NMDAR targeting synaptic stimulation protocol on synaptosomes, based

on a protocol used for the stimulation of cultured neurons (Shen and Meyer, 1999). We showed that NMDAR stimulation of synaptosomes with either Glu/Gly or Glu/Gly/KCl for 60 s can induce a significant increase in the amount of Thr286 phosphorylated CaMKIIα, in line with previous studies on hippocampal slices (Ouyang et al., 1999). This effect was more pronounced in PSD fraction isolated from stimulated and control synaptosomes, suggesting that the stimulation induced translocation of CaMKII from distal parts of the postsynaptic terminal to the PSD, in agreement with previous work on dissociated neuronal cultures (Shen and Meyer, 1999). Additionally, these results suggest that CaMKII activation and translocation are the specific result of NMDAR-mediated postsynaptic Ca^{2+} influx (Thalhammer et al., 2006).

6.2 General Morphology of the PSD

Cryo-ET of stimulated and non-stimulated synaptosomes enabled us to evaluate differences between the average cross-sectional thickness of their PSDs. Increase in the thickness of the PSD has been previously observed as either a result of ischemia (Hu et al., 1998; Martone et al., 1999) or glutamate receptor activation (Kotlyar et al., 1990; Yen et al., 1993). The treatments used in this study were previously shown to induce a rapid (within 1.5 min.) increase in the cross-sectional thickness of the PSD in cultured neurons and hippocampal slices that was shown to be at least in part related to the translocation and accumulation of CaMKII to their cytoplasmic faces (Dosemeci et al., 2001). However, our data showed no statistically significant increase in the cross-sectional thickness of the PSD in synaptosomes upon NMDAR stimulation with either Glu/Gly or Glu/Gly/KCl (Figure 16). Although special attention was given to the rapid homogenization of the brain tissue after decapitation, we can not rule out that transient ischemic conditions could have increased the CaMKII content of the PSD fraction (Suzuki et al., 1994), thus obscuring any additional increase in PSD thickness. Loss of cytosolic components during the synaptosomal preparation could be another factor contributing to the observed discrepancy. These however are unlikely reason, because

we could observe an increase in CaMKII phosphorylation and changes in its localization that require Calmodulin and Ca^{2+}. Another possible explanation is that previous studies relied on chemical fixation and dehydration, which are prone to relocation and aggregation artifacts.

6.3 Architecture of the PSD

We studied the native three-dimensional postsynaptic architecture by Cryo-ET in both pharmacologically stimulated and control synaptosomes, and in PSDs isolated from such synaptosomes.

Isolated PSDs and PSDs visualized within synaptosomes, both stimulated and non-stimulated, showed two distinct surfaces. One surface was rather smooth and planar, while the other was rather convoluted, strongly suggesting that these are the cleft and cytosolic surfaces of the PSD, respectively (Figure 23; Figure 19, C). This is consistent with previous observations employing rotary shadowing EM on isolated PSDs (Petersen et al., 2003). In some cases, different types of long irregular protrusions were observed enclosing areas of empty space within the structure of the PSD (Figure 19, D).

The tomographic data suggest that the core structure of the PSD consists of a mesh-like scaffold consisting of a dense network of filaments, oriented parallel and perpendicular to the synaptic cleft (Figure 18; Figure 22). This is in agreement with previous studies on high-pressure frozen, dehydrated synapses that showed a similar filamentous PSD organization (Chen et al., 2008, 2011). In those studies it was proposed that PSD95 forms vertical filaments which are in contact with horizontal filaments composed of PSD95-binding partners and other scaffolding proteins such as GKAP, Shank and SynGAP, among others. This scaffold seems to serve the role of a foundation on top of which additional PSD components can attach, forming the convoluted appearance of the cytosolic surface of the PSD (Figure 24). The idea of an underlying core scaffold within

the PSD is not new and has been suggested in a number of previous studies (Matus and Taff-Jones, 1978; Gulley and Reese, 1981; Petersen et al., 2003; Swulius et al., 2010).

In addition to the filamentous structure of the PSD core, globular proteins complexes, similar in shape and size to the ring-shaped CaMKII association domain, could be directly visualized in tomograms of isolated PSDs (Figure 25). These structures often displayed short filamentous protrusions attached to what appeared to be the CaMKII association domain and resembled the radially positioned kinase domains of the CaMKII holoenzyme (Figure 25). The structures were most abundant at the cytosolic face of the PSD, consistent with earlier immuno-EM observations (Petersen et al., 2003), which suggest that CaMKII could be one of the major components of the structures forming its convoluted cytosolic face. We also visually identified similar complexes embedded deep into the structure of the PSD. This is in agreement with known CaMKII interaction partners located within the PSD, such as densin-180, α-actinin and the NR2B subunit of the NMDAR (Sheng and Hoogenraad, 2007). This is also consistent with previous attempts to visually detect CaMKII at EM tomograms of negatively stained isolated PSDs (Fera et al., 2012), suggesting that approximately half of the identified CaMKII molecules lie at the cytoplasmic surface of the PSD, while the rest are scattered throughout its thickness.

6.4 Comparison of synaptosomal and PSD fractions

One could possibly argue that detergent extracted PSD fraction is not the best choice of a models system for studying the PSD architecture, since the PSDs are removed from their native cellular environment and some of their components might be lost and structural features changed during detergent extraction. While this is an important concern, we have chosen an isolation protocol based on mild detergent extraction that has been shown to maintain most of the PSDs protein components (Cho et al., 1992). Additionally, biochemical studies have shown different types of enzymatic activity present in the

PSD fraction, indicating that its components are functional proteins (Cotman et al., 1974; Kelly et al., 1985). Synaptosomes, on the other hand, provide a more physiological model system for the study of the PSD architecture, since the PSD is enclosed in the postsynaptic terminal and attached to the postsynaptic membrane within the closed membrane compartment of the postsynaptic terminal.

Here, we provided a direct comparison bewtween the structures of cryo-preserved PSDs from PSD fraction and synaptosomes. There were no obvious differences between the PSDs derived from the two preparations and they showed very similar morphological characteristics. This result argues against preparation artifacts and suggests that the two preparations are complementary for the study of the PSD architecture by Ctyo-ET. Although it has been shown that CaMKII is difficult to separate from the PSD (Kennedy, 1997), the possibility of a loss of PSD components during PSD fraction preparation cannot be excluded. From the EM perspective, the PSD fraction is better suited for imaging, because it is thinner, which enables higher resolution reconstructions to be obtained. Furthermore, since finding good spots for tomography is a fairly straightforward process, the PSD fraction is better suited for automated (batch) tomography applications.

Therfore, it might be beneficial for further studies to use both preparations: isolated PSDs to yield higher throughput and resolution and synaptosomes to confirm results obtained using isolated PSDs.

6.5 Detecting CaMKII in tomograms of synaptosomes and isolated PSDs by template matching

One of the goals of this work was to detect CaMKII molecules in both active and inactive states in tomograms of synaptosomes and isolated PSDs by template matching. So far, this technique has been shown to work for structures with strong inherent contrast,

such as ribosomes, but is quite challenging for identifying proteins. The rule of thumb is that template matching is feasible only in case the molecule of interest can be visually identified within the tomogram (personal communication with Dr. Friedrich Förster).

We applied template matching to tomograms of stimulated and non-stimulated synaptosomes using crystal structure models of both active and inactive CaMKII holoenzymes as templates. Particles that were detected, visually resembled the CaMKII association domain. However, no clear differences in the localization of active and inactive CaMKII could be recognized between the two sets of tomograms. Similar results were obtained in the case where template matching was performed on tomograms of isolated PSDs from stimulated and non-stimulated synaptosomes. While particles that visually resembled the CaMKII association domain could be detected, no apparent differences in the localization of active and inactive CaMKII within the structure of the PSD could be identified between tomograms of PSDs isolated from stimulated and non-stimulated synaptosomes. Here, It is important to point out that in both cases, template matching was done on a limited set of tomograms and the obtained results might not be truly representative. Furthermore, this outcome could be a consequence of the fact that the used templates were obtained from crystal structure models of the holoenzyme that is somewhat different from the one present in our sample, and so might not be adequate for the faithful detection of the molecules. Indeed, previous studies pointed out the need for an accurate template for the reliable performance of the method (Xu et al., 2011). This stressed the need for obtaining reliable structures of the CaMKII holoenzyme in both its active and inactive states by single particle analysis. Additionally, it has been shown previously that the inherent detector noise of CCD cameras is a major limitation for template matching in cryo-tomograms (Beck et al., 2009).

Using structures of the CaMKII holoenzyme in both its active and inactive states that we obtained by single particle analysis, we performed a test round of template matching on

one tomogram of an isolated PSD collected on a first generation DDD. Tomograms that were collected on DDDs were generally characterized by a superior visual appearance compared to the ones collected on conventional scintillator-coupled CCDs. However, no apparent differences in the localization of active and inactive CaMKII within the structure of the PSD could be identified by template matching in that tomogram. Subtomogram alignment and averaging of datasets consisting of the best hits obtained for active and inactive CaMKII, was in both cases unsuccessful in improving the resolution of the CaMKII holoenzyme. Judging from this analysis, it appears that at the current resolution level and at the current number of particles, we are unable to distinguish between the structures of activated and non-active CaMKII. This could probably be achieved by processing larger number of datasets of tomograms and would most probably require subtomogram classification. In addition, it might be beneficial to concentrate on the stimulation induced relocalization of CaMKII in synaptosomes, because a change in distribution is easier to recognize than a fairly small difference between activated and non-active CaMKII structures.

Moreover, new technological developments such as DDDs and TEM phase plates have recently become available at our department and alone, but especially in combination, allow a significant improvement in the obtainable resolution in Cryo-ET. We were able to obtain a number of tomograms of isolated PSDs collected on microscopes equipped with second generation of DDDs and TEM phase plates, which still need to be processed and would potentially allow for more reliable detection of activated and non-active CaMKII in cryo-tomograms.

6.6 Structures of activated and non-active recombinantly expressed mouse CaMKIIα

Because of the importance of CaMKII and the lack of adequate structure, we proceeded to solve its three-dimensional structure by a combination of sub-tomogram averaging

and single particle analysis. Mouse CaMKIIα was recombinantly expressed in insect cells for purification by Dennis Zimmermann (Department of Cell Biology, LMU Munich). Purification was initially done by Dennis Zimmermann, while at later stages we obtained the necessary expertise. We optimized sample handling, CaMKII activation and vitrification for both tomography and single particle analysis. These proved to be quite different because CaMKII behaved differently in the presence of Au fiducial markers. Using a relatively small subset of sub-tomograms of purified CaMKII, we obtained three-dimensional structures of the two states of the holoenzyme. Even though no symmetry was imposed, the structures revealed striking morphological differences. While both reconstructions showed a structure that resembled the six-fold symmetric, gear-shaped core of the association domain of the holoenzyme that has been observed previously (Kolodziej et al., 2000; Morris and Torok, 2001), the reconstruction of activated CaMKIIα showed additional densities spaced at somewhat regular distance around the structure, comparable to the CaMKIIα kinase domains shown previously to be associated with foot-like protrusions of the gear-shaped core of the association domain (Kolodziej et al., 2000). Both of the obtained reconstructions had a resolution of around 35 Å.

While reasonably sized datasets of sub-tomograms were collected for both states of the holoenzyme (Table 1), we were unable to obtain reliable higher resolution reconstructions using larger subsets of particles, due to computational limitations. Namely, computational resources available at the time were insufficient to allow the real-space subtomogram alignment and averaging of larger subsets of subtomograms (several thousands) that we had. Attempts to average particles using faster, spherical harmonics based alignment procedures resulted in overfitted structures with highly overestimated resolution estimates (Figure 36). This could be possibly explained by a high degree of structural heterogeneity of the CaMKIIα holoenzyme that prevented the accurate alignment and averaging of particles.

For single particle analysis, three independent datasets were collected amounting to a total of around 600 000 picked particles. Two of the datasets were collected from non-active CaMKIIα at different pixel sizes and one was collected from activated CaMKIIα (Table 2). In order to eliminate initial model bias, the structures obtained from sub-tomogram averaging were used as initial models in all single particle reconstructions. Single particle analysis was done with both the EMAN2 and RELION software packages, producing slightly diverging results. As expected, top-view reference-free 2D class averages obtained with the EMAN2 software package displayed a gear-shaped structure with apparent six-fold symmetry. Compared to class averages of non-active CaMKIIα, class averages of activated CaMKIIα had additional densities around the central gear-shaped association domain (Figure 39). 3D refinement using the EMAN2 software package with no imposed symmetry produced a gear shaped structure with apparent six-fold symmetry at a resolution of 15.9 Å (FSC at 0.5 between two sets) (Figure 41, A). This justified imposing a six-fold (C6) symmetry on the reconstruction, which resulted in a structure with slightly improved resolution (13.8 Å) and an apparent D6 symmetry (Figure 41, B). Therefore a D6 symmetry was imposed on all subsequent reconstructions in order to improve their resolution. Further 3D refinement was performed using all three datasets with D6 symmetry imposed. While the reconstructions obtained from both non-active CaMKIIα datasets showed structures that resembled in shape and size the gear-shaped CaMKIIα association domain, the reconstruction obtained from the activated CaMKIIα dataset also displayed foot-like protrusions, extending above and below the midplane of the association domain (Figure 42).

In order to exclude the possibility of the reconstructions being influenced by the choice of initial reference model, the initial models were swapped so that a structure of activated CaMKIIα, obtained by single-particle sub-tomogram averaging, was used as an initial reference model in a 3D refinement of an non-active CaMKIIα single particle dataset

and vice versa. This had a negligible effect on the general structural features of the reconstructions and showed that they are not biased by the choice of an initial model (Figure 43).

Due to the high degree of structural heterogeneity of the CaMKIIα holoenzyme, as indicated by sub-tomogram classification, we also performed single particle analysis using the RELION software package. RELION provides an unsupervised 3D classification procedure, based on maximum-likelihood, which makes it well suited for the classification of structurally heterogeneous data. In addition, performing single particle analysis with different software packages was a way to verify that our results were not biased by the choice of software.

While most of the top-view RELION reference-free 2D class averages displayed a 6-fold symmetry (Figure 44, A and B (fourth row)), some (2-12 %) of the the top-view class averages clearly had a 7-fold symmetry (Figure 44, A and B (fifth row)). To our knowledge,this is the first time that a full-length CaMKIIα holoenzyme has been observed to form 7-fold symmetric assemblies. Up to now such 7-fold symmetrical CaMKIIα association domains have only been observed in preparations of truncated association domains lacking the kinase domains and it has been even speculated that tetradecameric forms of the full length holoenzyme are not likely to exist (Rosenberg et al., 2006). Additionally, RELION's superior reference-free 2D classification procedure made it possible to identify class averages of different structural states of the association domain, which provided a clue to the process of interconverting between dodecameric and tetradecameric forms of the holoenzyme (Figure 44, C). These class averages suggest a model of tetradecameric assembly in which the dodecameric association domain opens up, forming a C-shaped ring with a gap that becomes increasingly larger and eventually large enough to incorporate a seventh association domain into each stacked association domain ring (Figure 44, C). A recent theoretical model of CaMKII subunit exchange, assuming holoenzyme as-

sembly from vertical association domain dimers, speculates that the CaMKII association domain within a holoenzyme, independent of being activated or not, would normally undergo fluctuations that convert it from a closed double-ring form to an open C-shaped form with a gap between two adjacent vertical dimers that can be large enough to incorporate a vertical association domain dimer (Stratton et al., 2014).

The finding that 7-fold symmetrical holoenzymes and different structural states of the association domain are also present in the sample added an additional level of structural heterogeneity to the one already identified by sub-tomogram classification. In order to extract more homogeneous particle datasets for 3D refinement, we employed both 2D classification and 3D classification with no imposed symmetry, which resulted in the generation of different subsets of particles (Table 3). 3D refinement was performed on all subsets (Figure 47). In order to resolve conformational heterogeneity of the 6-fold symmetrical particles, subsets corresponding to the best-resolved structures were obtained and then subjected to a further 3D classification with a D6 symmetry imposed. Final particle subsets were created by taking one ore more classes displaying similar structural features and they were used for 3D refinements.

Similar to the EMAN2 results, the best resolved structures of non-active and activated CaMKIIα displayed a notable difference between each other (Figure 49, A). While both structures formed dodecameric complexes with gear-shaped, $\sim$10 nm in diameter, CaMKIIα association domain, as observed in previous studies (Kolodziej et al., 2000; Chao et al., 2011), the structure of activated CaMKIIα showed foot-like protrusions extending above and below the midplane, similar to the kinase domains found previously to be associated with such protrusions (Kolodziej et al., 2000).

The extended kinase domains visualized in activated CaMKIIα are likely due to the activation and inherent flexibility of kinase domains. In contrast to a recent X-ray structure

of inhibited full-length human CaMKIIα construct with a very short CaMKIIβ7 (an alternative splicing variant of human CaMKIIβ) linker region (Chao et al., 2011), the kinase domains in the structure of activated CaMKIIα are positioned further away from the central association domain (Figure 52). This comes at no surprise, since not only was the 30 AA long linker region of CaMKIIα missing in the above mentioned X-ray structure (Figure 51), but the enzyme was also inhibited, resulting in the kinase domains being immobilized on top of the central association domain. Although this undoubtedly has aided crystallization, it is uncertain if this structure can be considered physiological. Furthermore, this holoenzyme structure is incompatible with an X-ray structure of the autoinhibited CaMKII kinase domain dimer determined previously by the same group (Rosenberg et al., 2005).

Rigid body fitting of the X-ray structure of the CaMKIIα association domain within the em density maps generated by RELION revealed the positions of the alpha helices to which the kinase domains are attached via flexible linkers (Figure 49, B). RELION's reported resolution estimates ("gold standard" FSC) for the activated and non-activate CaMKIIα reconstructions were 8.9 Å and 9.6 Å, respectively. They appear highly over-estimated, considering the visual appearance of the em density maps that gave the impression of around 20 Å (Figure 53). Cross-resolution (at 0.5 level) of the association domain region of each of the em maps with the X-ray structure of the CaMKIIα associated domain gave an estimate of around 20 Å in both cases, consistent with the visual impression.

Rings of density around the central association domain of non-active CaMKIIα, where the kinase domains are expected to be located, could be seen at lower thresholds. These were similar but weaker than the ones observed in activated CaMKIIα at the same threshold (Figure 53). The obtained em density maps allowed for a pseudo atomic model of the CaMKIIα holoenzyme to be built using the X-ray structure of the CaMKIIα as-

sociated domain (pdb id: 3SOA) and the X-ray structure of the autoinhibited CaMKII kinase domain (pdb id: 2BDW) (Figure 54). While this model could not be confirmed, it is based on structural data and is most likely closer to the real structure of the holoenzyme than any of the previous models

The structural heterogeneity of the CaMKIIα holoenzyme that we observed was likely due to the variance in the location of the kinase domains, which is made possible by the flexible linker region. Even if one assumes that each kinase domain has only two discrete conformational states, one hexameric ring alone (a half of a CaMKII holoenzyme) has 14 different conformations (Lučić et al., 2008). This high degree of conformational flexibility is probably one of the major factors that prevented us from reaching sub-nanometer resolution.

6.7 Outlook

For decades, the conventional way to visualize and quantify proteins in cellular EM has relied on immuno-gold labeling. This technique is however susceptible to problems arising from epitope availability and location and depends heavily on antibody efficiency. Being able to directly visualize CaMKII close to vitrified, frozen-hydrated samples, opens new opportunities for unraveling the structural arrangement of proteins within the PSD. Furthermore, advanced pattern recognition methods, such as template matching are capable of predicting the orientation of molecules within the PSD and therefore have to potential to provide a view on the three dimensional molecular interactions that hold the structure together.

Several morphological features were recognized in the PSD structure, but no clear differences could be visually discerned between PSDs from pharmacologically treated and control synaptosomes. While this could be possibly due to potential sample preparation related artifacts, it is also likely that these differences are quite subtle and identifying

them would require template matching combined with quantitative statistical analysis. Judging from our results, it appears that the reliable detection of CaMKII by template matching will require tomograms of higher resolution than the one currently possible with the state of the art scintilator-coupled CCDs. New technological developments such as DDDs and TEM phase plates allow a significant improvement in the obtainable resolution in Cryo-ET and in the future will be instrumental for the reliable application of template matching. Classification of larger datasets of sub-tomograms extracted by template matching from such tomograms would eventually allow the reliable detection of activated and non-active CaMKII. Due to the extremely high degree of structural heterogeneity of the CaMKII holoenzyme identified in this study, larger single particle datasets (in the order of a million particles) would be required to obtain a better understanding of the different conformations that the holoenzyme undergoes. Single particle tomography could actually prove to be a tool better suited for that task, especially with tomograms collected on microscopes equipped a DDD and a TEM phase plate.

7 Materials and Methods

7.1 Sample Preparation

7.1.1 Synaptosomal preparation

Cerebro-cortical synaptosomes were prepared from (6-8 weeks old) male Wistar rats as described previously (Dunkley et al., 1988; Millan et al., 2002) and in accordance with the guidelines of the Max-Planck-Institute of Biochemistry. The animals were anesthetized with chloroform, followed by decapitation and extraction of the cerebral cortex. The cortex was then homogenized in 9 ml of ice-cold homogenization buffer (HB: 0.32 M sucrose and 50 mM EDTA, 1 tablet of Complete mini EDTA-free protease inhibitor cocktail (Roche) per 10 ml, pH 7.4) using a glass-Teflon homogenizer with up to 7 gentle strokes at 700 rpm and centrifuged afterwards at 4°C for 2 min. at 2,000 g in an SS-34 rotor (Sorvall). The pellet (P1) was separated from the supernatant (S1), resuspended in HB and centrifuged at 4°C for another 2 min. at 2,000 g. The supernatant (S1′) was separated from the pellet (P1′), combined with S1 and centrifuged at 9,500 g for 12 min. at 4°C in an SS-34 rotor. The supernatant (S2) was removed and the synaptosome-enriched pellet (P2) was resuspended in 1 ml of HB and layered on top of a three-step (3%, 10%, and 23%) Percoll (GE Healthcare) gradient in HB. The gradient was centrifuged at 25,000 g for 6 min. at 4°C in an 75 Ti rotor (Beckman). Synaptosomes were recovered with a Pasteur pipette at the interface of 10% and 23% Percoll and diluted to a final volume of 50 ml in Hepes-buffered medium (HBM; 140 mM NaCl, 5 mM KCl, 5 mM NaHCO3, 1.2 mM Na2HPO4, 10 mM glucose, 10 mM Hepes, pH 7.4). Percoll was washed by centrifugation for at 22,000 g for 10 min. in an SS-34 rotor (Sorvall) and the pellet was resuspended in HBM buffer supplemented by either 1.8 mM CaCl2 alone or by 1.2 mM CaCl2 and 1 mM MgCl2 (see section Pharmacological Stimulation of Synaptosomes). Synaptosomes were diluted to ∼0.7 mg/ml

protein concentration, as determined by Protein UV, and incubated for 60 min. at 37°C before either vitrification or pharmacological stimulation. All steps were performed at 4°C (Figure 55).

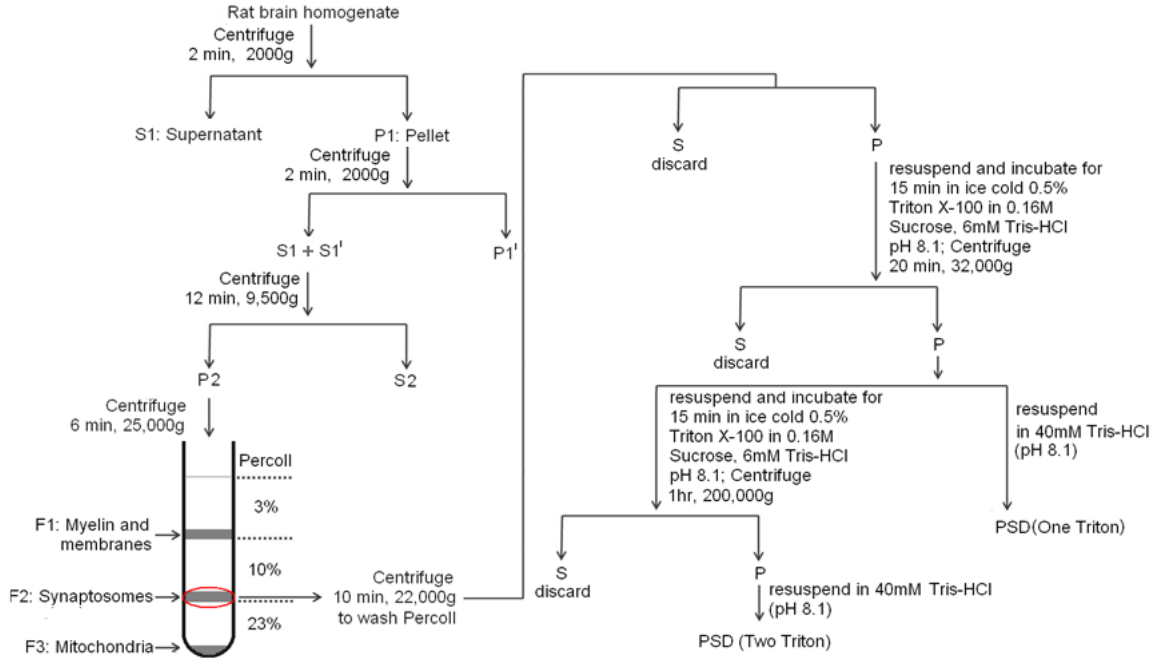

Figure 55: Synaptosomal and PSD fraction preparation.

7.1.2 PSD fraction preparation

PSD fraction was prepared from synaptosomes as described previously (Cho et al., 1992). In brief, synaptosomes were incubated for 15 min. in ice-cold 0.5% Triton X-100 solution (0.5% Triton X-100, 0.16M sucrose, 6mM Tris-HCl, pH 8.1) and then centrifuged at 32,000 g for 20 min. at 4°C in an 75 Ti rotor (Beckman-Coulter) to obtain the PSD (One Triton) pellet. This pellet was resuspended and incubated a second time in 0.5% Triton X-100 solution (0.5% Triton X-100, 0.16M sucrose, 6mM Tris-HCl, pH 8.1), then centrifuged at 200,000 x g for 1 hr to obtain the PSD (Two Triton) pellet. Both pellets were resuspended in 40 mM Tris-HCl (pH 8.1). Protein concentrations were determined by Protein UV. All steps were performed at 4°C (Figure 55).

7.1.3 FLAG-tag affinity purification of CaMKIIα

CaMKIIα FLAG-tag affinity purification was performed according to the protocol established by Dennis Zimmermann (LMU Munich). Sf9 cells from suspension culture, transfected with a recombinant bacmid DNA encoding a C-terminal FLAG-tagged mouse CaMKIIα, were harvested by centrifugation at 2,000 g for 15 min. at 4°C. The pelleted cells were resuspended in approx. 7.5% vol. (of initial cell suspension volume) Brickey Buffer (BB) 1X and homogenized by hand in a 50 ml glass homogenizer for 5 min. on ice. The homogenate was centrifuged at 24,000 g for 20 min. at 4°C in a 42.1 rotor (Beckman-Coulter). The supernatant was separated and mixed with 3% vol. (of lysis solution volume) anti-FLAG agarose resin (Anti-FLAG M2® Affinity Gel). The mixture was then incubated by rotating for 90 min. at 4°C and subsequently applied onto a PolyPrep® chromatography column (equilibrated beforehand with 2 ml of BB 1X). The anti-FLAG resin on the column was washed 3 to 4 times with 2 ml of Wash Buffer (WB) 1X accompanied by a constant stirring of the suspension with a glass rod and making sure the resin is at all times covered in buffer. Before protein elution, 1.5% vol. (of lysis suspension volume) of Elution Buffer (EB) was applied to the the column and left to incubate for 30 min. at 4°C, accompanied by frequent stirring with a glass rod. The protein was eluted by gently applying air pressure to the unsealed column with an air-ball. In order to make part of the purified CaMKIIα suitable for long-term storage (@ -80°C), some samples were dialyzed for 90 min. at 4°C into 500 ml Dialysis Buffer (DB: containing 10% glycerol) in a Slide-A-Lyzer® dialysis cassettes (0.5 - 3 ml capacity, 10 kDa molecular weight cut-off) immediately after elution.

7.1.4 Pharmacological Stimulation of Synaptosomes

Synaptosomes were stimulated pharmacologically by incubating them for 1 min. with either (i) Glutamate and Glycine (Glu 300 μM/Gly 300 μM) or (ii) Glutamate, Glycine and KCl (Glu 300 μM / Gly 300 μM / KCl 30 μM). Stimulated synaptosomes were either immediately vitrified or the reaction was stopped with a stop solution (SS) for

biochemical analysis.

7.1.5 CaMKIIα phosphorylation (activation) assay

In addition to non-active CaMKIIα samples, phosphorylated (activated) CaMKIIα samples were also prepared for both single particle cryo-EM and cryo-ET. Two reaction mixtures having the following compositions were prepared:

- CaMKII mixture: 1 μM CaMKIIα, 40 mM HEPES (pH 7.5), 150 mM KCl
- Saline-ATP-Cam mixture: 40 mM HEPES (pH 7.5), 1.4 mM $CaCl_2$, 2mM $MgCl_2$, 0.2 mM ATP, 150 mM KCl, 20 μM Calmodulin (CaM), 2 mM DTT

The assay was started by mixing equal volumes of the mixtures in an eppendorf tube and letting the reaction to proceed for 1 min. by holding the tube at the bottom with fingers to keep it warm, while pipetting up and down continuously. The samples were vitrified immediately after the reaction.

7.1.6 Vitrification

In the case of samples intended for Cryo-ET, a 4 μl drop of BSA-coated 10 nm colloidal gold (Aurion®) was pipetted on a glow-discharged, holey carbon (either copper or molybdenum) EM grid (Quantifoil) and allowed to dry at room temperature. A 4 μl drop of either synaptosomal suspension, PSD fraction or purified CaMKIIα was pipetted on the grid, blotted with filter paper and plunged into liquid ethane. This step was done either with an in-house made manual plunge freezing device or an FEI Vitrobot Mark IV (FEI, Eindhoven, Netherlands). For samples intended for single particle Cryo-EM, the gold deposition step was omitted and in cases where the abovementioned manual plunge freezing device was used for vitrification, the grids were washed twice with either Buffer or ddH_2O before blotting and plunge-freezing. Vitrified grids were stored in LN_2 before imaging in the TEM.

7.1.7 Negative stain

Lacey Carbon Copper Grids (Plano GmbH, Wetzlar, Germany) were coated with a thin carbon film and glow-discharged for 30 sec. A 4 μl drop of sample was pipetted on a teflon film and the grid was placed on top of the drop and incubated for 1 to 2 min. at room temperature. The grid was then transferred twice to drops of ddH_2O for washing and subsequently stained with 2% uranyl acetate for 1 min.

7.2 Electron Microscopy

7.2.1 Cryo-ET

Tilt series were collected in low-dose mode (Koster et al., 1997) on five different field emission gun-equipped transmission electron microscopes:

1. FEI Tecnai F20 transmission electron microscope (FEI, Eindhoven, Netherlands) operated at 200 kV. Equipped with an FEI Eagle 4k x 4k charged-coupled device camera (FEI, Eindhoven, Netherlands).

2. FEI Tecnai F20 transmission electron microscope (FEI, Eindhoven, Netherlands) operated at 200 kV. Equipped with a phase plate and an FEI Eagle 4k x 4k charged-coupled device camera (FEI, Eindhoven, Netherlands).

3. Philips CM300 transmission electron microscope (FEI, Eindhoven, Netherlands) operated at 300 kV. Equipped with a Gatan Image Filter (Gatan, Inc.) operated in the zero-loss mode and a Gatan MegaScan 2k x 2k charged-coupled device camera (Gatan, Inc.).

4. 2x FEI Tecnai Polara F30 G^2 transmission electron microscopes (FEI, Eindhoven, Netherlands) operated at 300 kV. Equipped with a Gatan Image Filter (Gatan, Inc.) operated in the zero-loss mode and a Gatan MegaScan 2k x 2k charged-coupled device camera (Gatan, Inc.).

5. FEI Titan Krios transmission electron microscope (FEI, Eindhoven, Netherlands) operated at 300 kV. Equipped with an FEI Falcon 4k x 4k Direct Detection Device (FEI, Eindhoven, Netherlands).

All microscopes were equipped with a computerized goniometer cryostage capable of tilting the sample up to ±70° degrees while keeping it at all times at LN2 temperatures. Tilt series were typically recorded in the range -64° to 64° with 2° angular increment with either FEI tomography software (version 4) or Serial-EM (Mastronarde, 2005). A number of magnifications and defocus settings were used, summarized in Table (tomograms). The total electron dose in all tomograms was kept below 100 $e^-/Å^2$. Nanogold beads were used as fiducial markers for tomogram alignment and three dimensional reconstructions were computed by weighted back-projection. Tomogram alignment and reconstruction were done using TOM toolbox (Nickell et al., 2005) and IMOD (Kremer et al., 1996).

7.2.2 Cryo-ET image processing and analysis

Segmentation Segmentation of structures present in tomograms was done both manually and semi-automatically. Manual segmentation was done with the Amira 3D software platform (FEI, Eindhoven, Netherlands) by manually outlining features of interest in x-y slices. Semi-automatic segmentation was done using both the Amira 3D software platform (FEI, Eindhoven, Netherlands) and Chimera (Pettersen et al., 2004) in the following way:

1. The tomogram was loaded in Amira and the threshold tool was used to select all the pixels within a certain grey-scale range.

2. The Structure of interest was then segmented by outlining structures of interest based on the selected pixels in step 1) and an Amira mesh was saved.

3. The Amira mesh was then loaded in Chimera and the "hide dust" tool was used to remove subsets of connected voxels below a certain size.

Morphometry The average thickness of a PSD was measured in the following way. The area enclosed by the PSD was selected in consecutive tomographic slices using the Amira Amira 3D software platform (FEI, Eindhoven, Netherlands), while the postsynaptic membrane enclosing it in each of these slices was traced separately. The volume of the PSD, calculated by summing the voxels from separate slices, was then divided by the area of the PSD-enclosing postsynaptic membrane to derive an average thickness for each PSD. Results are expressed as mean ± SEM. Control and stimulated groups were compared for thickness by One-way ANOVA (SPSS, IBM)

Template matching Template matching was performed with the PyTOM software package (Chen et al., 2013) on tomographic volumes reconstructed with a binning factor of 2. For generating templates from X-ray structures the gray-scale values of individual voxels were determined according to the sum of atomic numbers of atoms contained in those voxels. The resulting densities were convoluted with the microscope contrast transfer function, calculated for the defocus value used and sampled to the relevant voxel size. Templates generated by Single Particle Analysis and Sub-tomogram averaging were simply scaled to the relevant voxel size.

Sub-tomogram extraction, alignment, averaging and classification Sub-tomograms of activated and non-active CaMKIIα were extracted by template matching using a template generated from 259 manually boxed particles from a single tomogram of non-active CaMKIIα, collected at a defocus of -3.5 μm that were translationally aligned and averaged using the real space alignment procedure from the PyTOM software package (Hrabe et al., 2012) using a randomly selected boxed particle as a starting reference. Template matching hits were evaluated visually with the EMAN2 image processing suite (Tang et al., 2007) and false positives, such as boxed colloidal gold markers and contaminants, were excluded. Sub-tomogram alignment and averaging was performed on unbinned extracted sub-tomograms with either the real space alignment procedure from the PyTOM software package (Hrabe et al., 2012) or the FRM (Spherical Harmonics-

Based Fast Rotational Matching) alignment procedure from the same software package (Chen et al., 2013). Sub-tomogram classification was done based on constrained principal component analysis (CPCA) in conjugation with k-means clustering as described in (Forster et al., 2008).

CTF Correction CTF determination and correction of tilt series was carried out with the TOMOCTF software package (Fernandez et al., 2006).

7.2.3 Negative-stain EM

Electron micrographs of negatively stained CaMKIIα samples were acquired on a Philips CM200 transmission electron microscope (Philips, Eindhoven, Netherlands) operated at 160 kV and equipped with a Tietz 4k 4k charged-coupled device camera (TVIPS, Gauting, Germany). Micrographs were acquired at a magnification of 54 000x, resulting in an object pixel size at the specimen level of 2.78 Å. The nominal defocus of the micrographs ranged between -2 to -3 μm.

7.2.4 Single Particle Cryo-EM

Electron micrographs of frozen-hydrated CaMKIIα samples were acquired on an FEI Tecnai F20 transmission electron microscope (FEI, Eindhoven, Netherlands) operated at 200 kV and equipped with an FEI Eagle 4k 4k charged-coupled device camera (FEI, Eindhoven, Netherlands). The final electron dose in each micrograph was between 15 20 $e^-/Å^2$. Micrographs of non-active CaMKIIα were acquired at both 67 873x and 84 270x magnifications, resulting in object pixel sizes at the specimen level of 2.21 Å/pixel and 1.78 Å/pixel respectively, while micrographs of activated CaMKIIα were acquired at a magnification of 84 270x, resulting in an object pixel size at the specimen level of 1.78 Å/pixel. This resulted in the generation of three different data sets. The nominal defocus of the micrographs ranged between -1.5 to -3.8 μm.

7.2.5 Single Particle Cryo-EM Image processing

Micrograph selection and particle picking A total of 12500 micrographs of activated and non-active CaMKIIα were visually evaluated for particle concentration and ice quality and 4247 micrographs were selected for further, detailed evaluation of astigmatism, drift, spectral signal-to-noise ratio (SSNR) and defocus, which was performed with the EMAN2 software suite (Tang et al., 2007). After this evaluation, 2749 micrographs with defocus values ranging between -1.5 μm and -3.8 μm were selected for particle picking. Since data collection for non-active CaMKIIα was done at two different object pixel sizes (2.21 Å/pixel and 1.78 Å/pixel) and data collection for activated CaMKIIα was done at single object pixel size (1.78 Å/pixel), three independent single particle datasets were generated that are here referred to as 2.21 Å/pix non-active, 1.78 Å/pix non-active and 1.78 Å/pix activated dataset, respectively. Particle picking was performed automatically using the Gauss convolution method from the SPARX software package (Hohn et al., 2007). Each automatically picked micrograph was visually examined using the EMAN2 image processing suite (Tang et al., 2007) and picked false positives, such as contaminants or particles on the carbon layer, were manually removed. Picked particles for different datasets are summarized in (Table 2). In the case of 1.78 Å/pix non-active and 1.78 Å/pix activated datasets, an additional particle selection of the best images was made on the basis of spectral signal-to-noise ratio (SSNR), using the EMAN2 software suite (Table 2).

Image processing with EMAN2 For CTF correction, an automatic fitting of a theoretical CTF function to the experimental CTF function determined from the particles in each micrograph was performed using *ctfit.* and the results were manually reviewed and adjusted where needed. Phase flipping was applied to all particles. In a next step, reference-free 2D class averages were generated for all three datasets and particles that did not contribute to well defined class averages were removed. Two rounds of reference-free 2D classifications were performed followed by the removal of particles after each

round. The particles kept after 2D classification-based bad particle removal and used for three-dimensional reconstructions are summarized in (Table 2). In order to avoid initial model bias, initial models from single particle sub-tomogram averaging were used for all three-dimensional reconstructions. Models, along with the phase-flipped particles, were processed with e2refine. In this iterative refinement scheme, particle orientations were initially determined by comparing them to projections of the initial model with a 5° angular step. Particles with near-identical orientations were classified and aligned to the reference projections with the "refine" aligner using Fourier Ring Correlation similarity metric with SSNR weighting. Three rounds of iterative 2D class averaging was performed, keeping the best 85% (according to the similarity metric) in 2D class averages. Class averages were reconstructed in Fourier space and the newly generated 3D structure was used in the next cycle of refinement. Generally, 10 to 15 such refinement iterations were performed in each case and the obtained reconstructions were used as initial models for final reconstructions that were done with with projections of the initial model with a 1.5° angular step. Three-dimensional reconstructions were initially generated with no imposed symmetry and after it was concluded that the structure of the CaMKIIα holoenzyme exhibits a D6 symmetry this symmetry was imposed throughout the reconstruction process. Resolution of reconstructions was estimated by a standard FSC even/odd test (*e2eotest*). This routine separates all particles into two sets and uses the angular assignments obtained at the last iteration to make two models, which are then compared by FSC and the resolution is determined at 0.5 level.

Image processing with RELION This section describes Image processing for single particle analysis with the RELION software package (Scheres, 2012). Particle coordinates of picked particles from all three datasets (Table 2) were imported into RELION for preprocessing. CTFFIND3 (Mindell and Grigorieff, 2003) was used to estimate CTF parameters for each micrograph, after which particles were extracted and normalized. Reference free class averages were generated for all three datasets by RELION's maximum likelihood-based 2D reference-free class-averaging procedure. In contrast to the

results of 2D classification performed with EMAN2, top views of particles displaying a 7-fold symmetry were identified, which required the further separation of good particles into separate subsets. Similar to the image processing procedure performed with EMAN2, particles that did not contribute to well defined class averages were removed. Two rounds of reference-free 2D classifications were performed followed by the removal of particles after each round. Maximum likelihood-based 3D classification with no imposed symmetry was also performed on all three datasets with the goal of separating 3D classes of 6-fold symmetrical holoenzymes from those of 7-fold symmetrical ones. The subsets of particles identified as having a 6-fold symmetry by 3D classification together with the subsets of particles kept after 2D classification-based bad particle removal are summarized in Table 3. In order to avoid initial model bias, initial models from single particle sub-tomogram averaging were used for all three-dimensional reconstructions. D6 symmetry was imposed In all reconstructions. Since particle images are masked with a soft circular mask in RELION, a mask diameter of 250 Å was selected. Since RELION's 3D refinement procedure automatically modifies reconstructions parameters as it converges, specific choice of initial parameters had no influence on the final reconstructions.

Resolution of reconstructions was estimated by RELION's gold standard method. In this method, particles are separated into two sets at the very beginning, and the two completely independent structures are reconstructed. The resolution is determined at 0.143 level. The resolution was also estimated by calculating the FSC of the reconstructions with a density simulated from the X-ray structure of the CaMKIIα associated domain (cross-resolution). In this case FSC at 0.5 level was used.

7.3 Proteinbiochemistry

7.3.1 SDS-PAGE

Denaturing discontinuous polyacrylamide gel electrophoresis (Laemmli, 1970) was used to separate protein samples. The acrylamide concentration was 7.5% and 4% for the separation and stacking gels, respectively. Samples were mixed with 20% volumes of sample buffer and boiled at $95°C$ for 5 min. before being loaded onto the gel. Electrophoretic separation was performed in two steps, initially at 90 V for ∼30 min. and then at 140 V for ∼60 min. After separation, gels were either washed in western blot transfer buffer or incubated in Coomassie staining solution for ∼20 min. with constant shaking. Destaining was done with 2% acetic acid until all bands were clearly seen.

7.3.2 Western Blotting

Following SDS-PAGE separation, proteins were transferred from the polyacrylamide gel to a PVDF membrane by wet transfer for 2 h @ 35 V. Before assembling the blotting sandwich, PVDF membrane (Millipore) were activated by soaking them in methanol for ∼1 min. Following activation, PVDF membranes were soaked in water for 15 min. and then in transfer buffer for 30 min. Before detection, membranes were blocked overnight at $4°C$ in 5% BSA TTBS and washed afterwards with TTBS. Membranes were incubated overnight at $4°C$ in 1% BSA TTBS containing primary antibodies diluted to 1:1000. After incubation with the primary antibody, membranes were washed in three washes of TTBS, 10 min. each and then incubated for 1h at room temperature in 1% BSA TTBS containing fluorophore-conjugated secondary antibody (Alexa Fluor® 488). Membranes were then washed in three washes of TTBS, 10 min. each and then rinsed in TBS. Detection was performed with a fluorescent image analyzer (Fujifilm FLA-3000) using an excitation laser with a wavelength of 473 nm.

7.3.3 Chemicals

Acetic acid	Merck
Ammonium persulfate (APS)	Merck
Bromphenol blue	Serva
Comassie Brilliant Blue G 250	Serva
Disodium phosphate (Na_2HPO_4)	Sigma
1,4-Dithiothreitol (DTT)	Merck
Ethylenediaminetetraacetic acid (EDTA)	Merck
Ethanol p.a.	Merck
Glucose	Sigma
Glycerol 86-88%	Sigma
Glycine	Sigma
Hepes	Serva
Magnesium chloride ($MgCl_2$)	Serva
Methanol p.a.	Merck
Percoll ®	Sigma
Potassium chloride (KCl)	Sigma
Sodium bicarbonate ($NaHCO_3$)	Serva
Sodium chloride (NaCl)	Serva
Sodium dodecyl sulfate (SDS)	Bio-Rad
Sucrose	Sigma
N,N,N',N'-Tetramethylethylendiamin (TEMED)	Sigma
Tris-HCl (Tris)	Sigma
Triton X-100	Serva
Tween 20®	Serva

7.3.4 Standards

Precision Plus Protein^{TM} Dual Color - BIO-RAD

7.3.5 Buffers and Solutions

Buffers for FLAG-tag affinity purification of CaMKIIα

Elution Buffer (EB)
40 mM Hepes, pH 7.5
500 mM NaCl
1 mM EGTA
8% FLAG Peptides [5μg/μl]

Dialysis Buffer (DB)
10 mM Hepes, pH 7.5
150 mM KCl
0.1 mM EGTA
10% Glycerol

Brickey Buffer (BB)
10 mM Tris-HCl, pH 7.5
1 mM EGTA
1 mM EDTA
2.5% (v/v) Betaine
1 Tablet/50ml Protease Inhibitor (EDTA-free, Roche)

Wash Buffer (WB)
40 mM Hepes, pH 7.5
100 mM NaCl
1 mM EGTA

Buffers and solutions for Synaptosomal and PSD fraction preparation

0.5% Triton X-100 solution
0.5% (v/v) Triton X-100
0.16 M Sucrose
6 mM Tris-HCl, pH 8.1

Sucrose Solution (5x)
0.25 M EDTA
1.60 M Sucrose

Homogenization buffer (HB)
50 mM EDTA
0.32 M Sucrose
1 Tablet/10ml Protease Inhibitor (EDTA-free, Roche)

Hepes-buffered medium (HBM) (10x)
1.40 M NaCl
50 mM KCl
50 mM $NaHCO_3$
12 mM Na_2HPO_4
10 mM $MgCl_2$
100 mM Glucose
1 M Hepes, pH 7.4

Percoll 3%
3% (v/v) Percoll
20% (v/v) Sucrose Solution (5x)

Percoll 10%
10% (v/v) Percoll
20% (v/v) Sucrose Solution (5x)

Percoll 23%
10% (v/v) Percoll
20% (v/v) Sucrose Solution (5x)

Buffers for SDS-PAGE and Western Blot

Sample Buffer, SDS-PAGE (5X)
250 mM Tris-HCl, pH 6.8
10% (w/v) SDS
50% (w/v) Glycerol
0.02% (w/v) Bromphenol Blue
addition of 50 mM DTT before use

APS Solution
10% (w/v) APS in Water

Cathode buffer, SDS-PAGE
100 mM Tris-HCl
100 mM Glycine
0.1 % (w/v) SDS

Coomassie Brilliant Blue Solution
0.25% (w/v) Commassie Brilliant Blue R-250
50% (v/v) Methanol
10% (v/v) Glacial Acetic acid

Transfer buffer (10x)
250 mM Tris
1.92 M Glycine

Tris-Buffered Saline (TBS)
0.5 M Tris-HCl
1.55 M NaCl

Tween Tris-Buffered Saline (TTBS)
10% (v/v) TBS
0.1% (v/v) Tween 20®

7.3.6 Antibodies

Antibody Name	Type	Isotype/host	Company, Location
Anti-total CaMKII (6G9), monoclonal	Primary	IgG1/Mouse	Thermo Scientific, Bonn
Anti-Phospho (Thr286)-CaMKII (22B1), monoclonal	Primary	IgG1/Mouse	Thermo Scientific, Bonn
Anti-Mouse Alexa Fluor® 488	Secondary	IgG/Goat	Thermo Scientific, Bonn

7.3.7 Protein identification by mass spectrometry

The identity of expressed CaMKIIα was confirmed by mass spectrometry analysis. Liquid chromatography tandem mass spectrometry (LC-MS/MS) was performed by the Core Facility at the MPI of Biochemistry from in-gel-digested protein bands.

8 Appendix

Sample	number of experiments	number of tomograms	pixel size	defocus	Microscope	Camera	Voltage	Phase Plate
Synaptosome (control)	8	9	6.8 Å/pix	-10.0 µm	Philips CM 300	CCD	300 kV	NO
		14	6.6 Å/pix	-10.0 µm	FEI Tecnai 'Polara' F30	CCD	300kV	NO
		5	3.8 Å/pix	-7.0 µm	FEI Tecnai 'Polara' F30	CCD	300kV	NO
		8	4.7 Å/pix	-7.0 µm	FEI Tecnai 'Polara' F30	CCD	300kV	NO
		5	4.7 Å/pix	-5.0 µm	FEI Tecnai 'Polara' F30	CCD	300kV	NO
Synaptosome (Glu/Gly)	3	3	6.6 Å/pix	-7.0 µm	FEI Tecnai 'Polara' F30	CCD	300kV	NO
		8	4.7 Å/pix	-5.0 µm	FEI Tecnai 'Polara' F30	CCD	300kV	NO
		5	4.7 Å/pix	-7.0 µm	FEI Tecnai 'Polara' F30	CCD	300kV	NO
Synaptosome (Glu/Gly/KCl)	4	19	4.7 Å/pix	-7.0 µm	FEI Tecnai 'Polara' F30	CCD	300kV	NO
		5	4.7 Å/pix	-5.0 µm	FEI Tecnai 'Polara' F30	CCD	300kV	NO
Synaptosome TOTAL	-	81	-	-	-	-		-

Table 4: Tomograms of synaptosomes: Total dataset

Sample	number of experiments	number of tomograms	pixel size	defocus	Microscope	Camera	Voltage	Phase Plate
PSD fraction (control)	4	7	4.7 Å/pix	-6.0 µm	FEI Tecnai 'Polara' F30	CCD	300kV	NO
		2	3.8 Å/pix	-4.0 µm	FEI Tecnai 'Polara' F30	CCD	300kV	NO
		3	4.6 Å/pix	-4.0 µm	FEI Titan Krios	DDD	300kV	NO
		4	4.2 Å/pix	-500 nm	FEI Tecnai F20	CCD	200kV	YES
		2	4.2 Å/pix	-500 nm	FEI Titan Krios	DDD	300kV	YES
PSD fraction (Glu/Gly/KCl)	2	7	2.9 Å/pix	-4.0 µm	FEI Titan Krios	DDD	300kV	NO
		5	4.2 Å/pix	-500 nm	FEI Tecnai F20	CCD	200kV	YES
PSD fraction TOTAL	-	30	-	-	-	-		-

Table 5: Tomograms of PSD fraction: Total dataset

Sample	number of experiments	number of tomograms	pixel size	defocus	Microscope	Camera	Voltage	Phase Plate
CaMKIIα (non-active)	4	7	3.8 Å/pix	-7.0 µm	FEI Tecnai 'Polara' F30	CCD	300kV	NO
		18	2.9 Å/pix	-4.0 µm	FEI Titan Krios	DDD	300kV	NO
		7	2.2 Å/pix	-3.5 µm	FEI Tecnai F20	CCD	200kV	NO
		13	2.2 Å/pix	-5.0 µm	FEI Tecnai F20	CCD	200kV	NO
CaMKIIα activated	2	8	2.2 Å/pix	-3.5 µm	FEI Tecnai F20	CCD	200kV	NO
		14	2.2 Å/pix	-5.0 µm	FEI Tecnai F20	CCD	200kV	NO
CaMKIIα TOTAL	-	67	-	-	-	-	-	-

Table 6: Tomograms of CaMKIIα: Total dataset

9 Abbreviations

2D	two-dimensional
3D	three-dimensional
Å	Ångström
$°C$	Degree Celsius
CaMKII	Calcium/Calmodulin dependent protein kinase II
CCD	Charged Coupled Device
CPCA	Constrained Principal Component Analysis
Cryo-ET	Cryo Electron Tomography
Cryo-EM	Cryo Electron Microscopy
CTF	Contrast Transfer Function
DDD	Direct Detection Device
EM	Electron Microscopy
ET	Electron Tomography
FEG	Field Emission Gun
g	Nominal Gravitational Acceleration
Glu	Glutamate
Gly	Glycine
KCl	Potassium chloride
kDa	Kilo Dalton
kV	Kilo Volts
keV	Kilo Electron Volts
LaB_6	Lanthanum Hexaboride
min.	minutes
M	Molar
mM	Millimolar
μM	Micromolar
ml	millilitre
μl	microlitre

PDB	Protein Data Bank
pix	pixel
SNR	Signal-to-Noise Ratio
SDS	sodium dodecyl sulfate
SDS-PAGE	SDS-polyacrylamide gel electrophoresis
TEM	Transmission Electron Microscope
TBS	Tris-buffered saline
TTBS	Tween Tris-buffered saline
V	volts
v/v	volume/volume
w/v	weight/volume

10 Bibliography

J. A. Allen, R. A. Halverson-Tamboli, and M. M. Rasenick. Lipid raft microdomains and neurotransmitter signalling. *Nat. Rev. Neurosci.*, 8(2):128–140, Feb 2007.

F. Amat, F. Moussavi, L. R. Comolli, G. Elidan, K. H. Downing, and M. Horowitz. Markov random field based automatic image alignment for electron tomography. *J. Struct. Biol.*, 161(3):260–275, Mar 2008.

T. S. Baker and R. Henderson. Electron cryomicroscopy of biological macromolecules. *International Tables for Crystallography*, F:593–614, 2012.

M. K. Baron, T. M. Boeckers, B. Vaida, S. Faham, M. Gingery, M. R. Sawaya, D. Salyer, E. D. Gundelfinger, and J. U. Bowie. An architectural framework that may lie at the core of the postsynaptic density. *Science*, 311(5760):531–535, Jan 2006.

A. Barria, D. Muller, V. Derkach, L. C. Griffith, and T. R. Soderling. Regulatory phosphorylation of AMPA-type glutamate receptors by CaM-KII during long-term potentiation. *Science*, 276(5321):2042–2045, Jun 1997.

A. Baude, Z. Nusser, J. D. Roberts, E. Mulvihill, R. A. McIlhinney, and P. Somogyi. The metabotropic glutamate receptor (mGluR1 alpha) is concentrated at perisynaptic membrane of neuronal subpopulations as detected by immunogold reaction. *Neuron*, 11(4):771–787, Oct 1993.

K. U. Bayer, P. De Koninck, A. S. Leonard, J. W. Hell, and H. Schulman. Interaction with the NMDA receptor locks CaMKII in an active conformation. *Nature*, 411(6839): 801–805, Jun 2001.

M. Beck, J. A. Malmstrom, V. Lange, A. Schmidt, E. W. Deutsch, and R. Aebersold. Visual proteomics of the human pathogen Leptospira interrogans. *Nat. Methods*, 6 (11):817–823, Nov 2009.

C. Best, S. Nickell, and W. Baumeister. Localization of protein complexes by pattern recognition. *Methods Cell Biol.*, 79:615–638, 2007.

S. Brenner and R.W. Horne. A negative staining method for high resolution electron microscopy of viruses. *Biochimica et Biophysica Acta*, 34(0):103–110, 1959. ISSN 0006-3002.

G. Cardone, K. Grunewald, and A. C. Steven. A resolution criterion for electron tomography based on cross-validation. *J. Struct. Biol.*, 151(2):117–129, Aug 2005.

L. H. Chao, M. M. Stratton, I. H. Lee, O. S. Rosenberg, J. Levitz, D. J. Mandell, T. Kortemme, J. T. Groves, H. Schulman, and J. Kuriyan. A mechanism for tunable autoinhibition in the structure of a human Ca2+/calmodulin- dependent kinase II holoenzyme. *Cell*, 146(5):732–745, Sep 2011.

X. Chen, L. Vinade, R. D. Leapman, J. D. Petersen, T. Nakagawa, T. M. Phillips, M. Sheng, and T. S. Reese. Mass of the postsynaptic density and enumeration of three key molecules. *Proc. Natl. Acad. Sci. U.S.A.*, 102(32):11551–11556, Aug 2005.

X. Chen, C. Winters, R. Azzam, X. Li, J. A. Galbraith, R. D. Leapman, and T. S. Reese. Organization of the core structure of the postsynaptic density. *Proc. Natl. Acad. Sci. U.S.A.*, 105(11):4453–4458, Mar 2008.

X. Chen, C. D. Nelson, X. Li, C. A. Winters, R. Azzam, A. A. Sousa, R. D. Leapman, H. Gainer, M. Sheng, and T. S. Reese. PSD-95 is required to sustain the molecular organization of the postsynaptic density. *J. Neurosci.*, 31(17):6329–6338, Apr 2011.

Y. Chen, S. Pfeffer, T. Hrabe, J. M. Schuller, and F. Forster. Fast and accurate reference-free alignment of subtomograms. *J. Struct. Biol.*, 182(3):235–245, Jun 2013.

D. Cheng, C. C. Hoogenraad, J. Rush, E. Ramm, M. A. Schlager, D. M. Duong, P. Xu, S. R. Wijayawardana, J. Hanfelt, T. Nakagawa, M. Sheng, and J. Peng. Relative and absolute quantification of postsynaptic density proteome isolated from rat forebrain and cerebellum. *Mol. Cell Proteomics*, 5(6):1158–1170, Jun 2006.

K. O. Cho, C. A. Hunt, and M. B. Kennedy. The rat brain postsynaptic density fraction contains a homolog of the Drosophila discs-large tumor suppressor protein. *Neuron*, 9(5):929–942, Nov 1992.

K. S. Christopherson, N. T. Sweeney, S. E. Craven, R. Kang, A. e. l. D. El-Husseini, and D. S. Bredt. Lipid- and protein-mediated multimerization of PSD-95: implications for receptor clustering and assembly of synaptic protein networks. *J. Cell. Sci.*, 116 (Pt 15):3213–3219, Aug 2003.

R. J. Colbran. Inactivation of Ca2+/calmodulin-dependent protein kinase II by basal autophosphorylation. *J. Biol. Chem.*, 268(10):7163–7170, Apr 1993.

R. J. Colbran. Targeting of calcium/calmodulin-dependent protein kinase II. *Biochem. J.*, 378(Pt 1):1–16, Feb 2004.

C. W. Cotman, G. Banker, L. Churchill, and D. Taylor. Isolation of postsynaptic densities from rat brain. *J. Cell Biol.*, 63(2 Pt 1):441–455, Nov 1974.

R. A. Crowther, L. A. Amos, J. T. Finch, D. J. De Rosier, and A. Klug. Three dimensional reconstructions of spherical viruses by fourier synthesis from electron micrographs. *Nature*, 226(5244):421–425, May 1970a.

R. A. Crowther, D. J. DeRosier, and A. Klug. The reconstruction of a three-dimensional structure from projections and its application to electron microscopy. *Proceedings of the Royal Society of London. Series A, Mathematical and Physical Sciences*, 317 (1530):pp. 319–340, 1970b.

R Danev and K Nagayama. Transmission electron microscopy with zernike phase plate. *Ultramicroscopy*, 88(4):243 – 252, 2001. ISSN 0304-3991.

R Danev and K Nagayama. Chapter fourteen - phase plates for transmission electron microscopy. In Grant J. Jensen, editor, *Cryo-EM Part A Sample Preparation and Data Collection*, volume 481 of *Methods in Enzymology*, pages 343 – 369. Academic Press, 2010.

J. Darbon, A. Cunha, T. F. Chan, S. Osher, and G. J. Jensen. Fast nonlocal filtering applied to electron cryomicroscopy. In *Biomedical Imaging: From Nano to Macro, 2008. ISBI 2008. 5th IEEE International Symposium on*, pages 1331–1334. IEEE, 2008.

T. Daud, J. R. Janesick, K. Evans, and T Elliott. Charge-coupled-device response to electron beam energies of less than 1 keV up to 20 keV. *Optical Engineering*, 26: 686–691, August 1987.

P. De Koninck and H. Schulman. Sensitivity of CaM kinase II to the frequency of Ca2+ oscillations. *Science*, 279(5348):227–230, Jan 1998.

E. D. P. De Robertis. Fine structure of synapses in the central nervous system. *Proc. Intern. Congr. Neuropathol.*, 4th, Munich:35–38, 1962.

D. J. De Rosier and A. Klug. Reconstruction of three dimensional structures from electron micrographs. *Nature*, 217(5124):130–134, Jan 1968.

K. Dierksen, D. Typke, R. Hegerl, A.J. Koster, and W. Baumeister. Towards automatic electron tomography. *Ultramicroscopy*, 40(1):71–87, 1992.

K. Dierksen, D. Typke, R. Hegerl, J. Walz, E. Sackmann, and W. Baumeister. Three-dimensional structure of lipid vesicles embedded in vitreous ice and investigated by automated electron tomography. *Biophysical journal*, 68(4):1416–1422, 1995.

A. Dosemeci, J. H. Tao-Cheng, L. Vinade, C. A. Winters, L. Pozzo-Miller, and T. S. Reese. Glutamate-induced transient modification of the postsynaptic density. *Proc. Natl. Acad. Sci. U.S.A.*, 98(18):10428–10432, Aug 2001.

K. H. Downing and R. M. Glaeser. Restoration of weak phase-contrast images recorded with a high degree of defocus: the twin image problem associated with ctf correction. *Ultramicroscopy*, 108(9):921–928, 2008.

D. A. Doyle, A. Lee, J. Lewis, E. Kim, M. Sheng, and R. MacKinnon. Crystal structures of a complexed and peptide-free membrane protein-binding domain: molecular basis of peptide recognition by PDZ. *Cell*, 85(7):1067–1076, Jun 1996.

J. Dubochet, J. Lepault, R. Freeman, J. A. Berriman, and J.-C. Homo. Electron microscopy of frozen water and aqueous solutions. *Journal of Microscopy*, 128(3):219–237, 1982.

J. Dubochet, M. Adrian, J. J. Chang, J. C. Homo, J. Lepault, A. W. McDowall, and P. Schultz. Cryo-electron microscopy of vitrified specimens. *Q. Rev. Biophys.*, 21(2): 129–228, May 1988.

P. R. Dunkley, J. W. Heath, S. M. Harrison, P. E. Jarvie, P. J. Glenfield, and J. A. Rostas. A rapid Percoll gradient procedure for isolation of synaptosomes directly from an S1 fraction: homogeneity and morphology of subcellular fractions. *Brain Res.*, 441(1-2):59–71, Feb 1988.

A. e. l. D. El-Husseini, E. Schnell, S. Dakoji, N. Sweeney, Q. Zhou, O. Prange, C. Gauthier-Campbell, A. Aguilera-Moreno, R. A. Nicoll, and D. S. Bredt. Synaptic strength regulated by palmitate cycling on PSD-95. *Cell*, 108(6):849–863, Mar 2002.

H. P. Erickson and A. Klug. The fourier transform of an electron micrograph: Effects of defocussing and aberrations, and implications for the use of underfocus contrast enhancement. *Berichte der Bunsengesellschaft fr physikalische Chemie*, 74(11):1129–1137, 1970. ISSN 0005-9021.

N. E. Erondu and M. B. Kennedy. Regional distribution of type II Ca2+/calmodulin-dependent protein kinase in rat brain. *J. Neurosci.*, 5(12):3270–3277, Dec 1985.

A. Fera, A. Dosemeci, A. A. Sousa, C. Yang, R. D. Leapman, and T. S. Reese. Direct visualization of CaMKII at postsynaptic densities by electron microscopy tomography. *J. Comp. Neurol.*, 520(18):4218–4225, Dec 2012.

J. J. Fernandez and S. Li. An improved algorithm for anisotropic nonlinear diffusion for denoising cryo-tomograms. *J. Struct. Biol.*, 144(1-2):152–161, 2003.

J. J. Fernandez, S. Li, and R. A. Crowther. CTF determination and correction in electron cryotomography. *Ultramicroscopy*, 106(7):587–596, May 2006.

R. Fernandez-Busnadiego, B. Zuber, U. E. Maurer, M. Cyrklaff, W. Baumeister, and V. Lučić. Quantitative analysis of the native presynaptic cytomatrix by cryoelectron tomography. *J. Cell Biol.*, 188(1):145–156, Jan 2010.

N. Fischer, A. L. Konevega, W. Wintermeyer, M. V. Rodnina, and H. Stark. Ribosome dynamics and tRNA movement by time-resolved electron cryomicroscopy. *Nature*, 466(7304):329–333, Jul 2010.

D. K. Fong, A. Rao, F. T. Crump, and A. M. Craig. Rapid synaptic remodeling by protein kinase C: reciprocal translocation of NMDA receptors and calcium/calmodulin-dependent kinase II. *J. Neurosci.*, 22(6):2153–2164, Mar 2002.

F. Förster, O. Medalia, N. Zauberman, W. Baumeister, and D. Fass. Retrovirus envelope protein complex structure in situ studied by cryo-electron tomography. *Proc. Natl. Acad. Sci. U.S.A.*, 102(13):4729–4734, Mar 2005.

F. Forster, S. Pruggnaller, A. Seybert, and A. S. Frangakis. Classification of cryo-electron sub-tomograms using constrained correlation. *J. Struct. Biol.*, 161(3):276–286, Mar 2008.

A. S. Frangakis and F. Forster. Computational exploration of structural information from cryo-electron tomograms. *Curr. Opin. Struct. Biol.*, 14(3):325–331, Jun 2004.

A. S. Frangakis and R. Hegerl. Noise reduction in electron tomographic reconstructions using nonlinear anisotropic diffusion. *J. Struct. Biol.*, 135(3):239–250, Sep 2001.

A. S. Frangakis and R. Hegerl. Segmentation of two- and three-dimensional data from electron microscopy using eigenvector analysis. *J. Struct. Biol.*, 138(1-2):105–113, 2002.

A. S. Frangakis, J. Bohm, F. Forster, S. Nickell, D. Nicastro, D. Typke, R. Hegerl, and W. Baumeister. Identification of macromolecular complexes in cryoelectron tomograms of phantom cells. *Proc. Natl. Acad. Sci. U.S.A.*, 99(22):14153–14158, Oct 2002.

J. Frank. Single-particle imaging of macromolecules by cryo-electron microscopy. *Annu Rev Biophys Biomol Struct*, 31:303–319, 2002.

J. Frank. *Three-Dimensional Electron Microscopy of Macromolecular Assemblies: Visualization of Biological Molecules in Their Native State*. Oxford University Press, USA, 2006. ISBN 9780195182187.

J. Frank. *Electron Tomography: Methods for Three-Dimensional Visualization of Structures in the Cell*. Springer, 2008. ISBN 9780387690087.

J Frank and P Penczek. On the correction of the contrast transfer function in biological electron microscopy. *Optik*, 98(3):125–129, 1995.

K. M. Franks and T. J. Sejnowski. Complexity of calcium signaling in synaptic spines. *Bioessays*, 24(12):1130–1144, Dec 2002.

K. Fukunaga, L. Stoppini, E. Miyamoto, and D. Muller. Long-term potentiation is associated with an increased activity of Ca2+/calmodulin-dependent protein kinase II. *J. Biol. Chem.*, 268(11):7863–7867, Apr 1993.

T. R. Gaertner, S. J. Kolodziej, D. Wang, R. Kobayashi, J. M. Koomen, J. K. Stoops, and M. N. Waxham. Comparative analyses of the three-dimensional structures and enzymatic properties of alpha, beta, gamma and delta isoforms of Ca2+-calmodulin-dependent protein kinase II. *J. Biol. Chem.*, 279(13):12484–12494, Mar 2004.

F. Gardoni, L. H. Schrama, J. J. van Dalen, W. H. Gispen, F. Cattabeni, and M. Di Luca. AlphaCaMKII binding to the C-terminal tail of NMDA receptor subunit NR2A and its modulation by autophosphorylation. *FEBS Lett.*, 456(3):394–398, Aug 1999.

R. M. Glaeser and K. A. Taylor. Radiation damage relative to transmission electron microscopy of biological specimens at low temperature: a review. *J Microsc*, 112(1): 127–138, Jan 1978.

E. G. Gray. Axo-somatic and axo-dendritic synapses of the cerebral cortex: an electron microscope study. *J. Anat.*, 93:420–433, Oct 1959.

L. C. Griffith, C. S. Lu, and X. X. Sun. CaMKII, an enzyme on the move: regulation of temporospatial localization. *Mol. Interv.*, 3(7):386–403, Oct 2003.

R Grimm, AJ Koster, U Ziese, D Typke, and W Baumeister. Zero-loss energy filtering under low-dose conditions using a post-column energy filter. *Journal of Microscopy*, 183(1):60–68, 1996.

R. Grimm, M. Bärmann, W. Häckl, D. Typke, E. Sackmann, and W. Baumeister. Energy filtered electron tomography of ice-embedded actin and vesicles. *Biophysical journal*, 72(1):482–489, 1997.

R. Guckenberger. Determination of a common origin in the micrographs of tilt series in three-dimensional electron microscopy. *Ultramicroscopy*, 9(1–2):167–173, 1982.

R. L. Gulley and T. S. Reese. Cytoskeletal organization at the postsynaptic complex. *J. Cell Biol.*, 91(1):298–302, Oct 1981.

P. I. Hanson and H. Schulman. Inhibitory autophosphorylation of multifunctional Ca2+/calmodulin-dependent protein kinase analyzed by site-directed mutagenesis. *J. Biol. Chem.*, 267(24):17216–17224, Aug 1992.

P. I. Hanson, M. S. Kapiloff, L. L. Lou, M. G. Rosenfeld, and H. Schulman. Expression of a multifunctional Ca2+/calmodulin-dependent protein kinase and mutational analysis of its autoregulation. *Neuron*, 3(1):59–70, Jul 1989.

G. Harauz and F.P. Ottensmeyer. Direct three-dimensional reconstruction for macromolecular complexes from electron micrographs. *Ultramicroscopy*, 12(4):309–319, 1984.

G. Harauz and M. van Heel. Exact filters for general geometry three dimensional reconstruction. In *Proceedings of the IEEE Computer Vision and Pattern Recognition Conf*, volume 73, pages 146–156, 1986.

R. G. Hart. Electron microscopy of unstained biological material: the polytropic montage. *Science*, 159(3822):1464–1467, Mar 1968.

P. W. Hawkes. Computer processing of electron microscope images. *Computer Processing of Electron Microscope Images. Series: Topics in Current Physics*, 13, 1980.

M. A Hayat and S. E. Miller. *Negative staining.* McGraw-Hill Publishing Company New York, 1990.

R. Hegerl and W. Hoppe. Influence of electron noise on three-dimensional image reconstruction. *Zeitschrift Naturforschung Teil A*, 31:1717, 1976.

A. Hoelz, A. C. Nairn, and J. Kuriyan. Crystal structure of a tetradecameric assembly of the association domain of Ca2+/calmodulin-dependent kinase II. *Mol. Cell*, 11(5): 1241–1251, May 2003.

M. Hohn, G. Tang, G. Goodyear, P. R. Baldwin, Z. Huang, P. A. Penczek, C. Yang, R. M. Glaeser, P. D. Adams, and S. J. Ludtke. SPARX, a new environment for Cryo-EM image processing. *J. Struct. Biol.*, 157(1):47–55, Jan 2007.

W. Hoppe, J. Gassmann, N. Hunsmann, H. J. Schramm, and M. Sturm. Three-dimensional reconstruction of individual negatively stained yeast fatty-acid synthetase

molecules from tilt series in the electron microscope. *Hoppe-Seyler's Z. Physiol. Chem.*, 355(11):1483–1487, Nov 1974.

T. Hrabe, Y. Chen, S. Pfeffer, L. K. Cuellar, A. V. Mangold, and F. Forster. PyTom: a python-based toolbox for localization of macromolecules in cryo-electron tomograms and subtomogram analysis. *J. Struct. Biol.*, 178(2):177–188, May 2012.

Y. P. Hsueh, E. Kim, and M. Sheng. Disulfide-linked head-to-head multimerization in the mechanism of ion channel clustering by PSD-95. *Neuron*, 18(5):803–814, May 1997.

B. R. Hu, M. Park, M. E. Martone, W. H. Fischer, M. H. Ellisman, and J. A. Zivin. Assembly of proteins to postsynaptic densities after transient cerebral ischemia. *J. Neurosci.*, 18(2):625–633, Jan 1998.

A. Hudmon and H. Schulman. Structure-function of the multifunctional Ca2+/calmodulin-dependent protein kinase II. *Biochem. J.*, 364(Pt 3):593–611, Jun 2002.

H. Husi, M. A. Ward, J. S. Choudhary, W. P. Blackstock, and S. G. Grant. Proteomic analysis of NMDA receptor-adhesion protein signaling complexes. *Nat. Neurosci.*, 3 (7):661–669, Jul 2000.

W. Jiang, M. L. Baker, Q. Wu, C. Bajaj, and W. Chiu. Applications of a bilateral denoising filter in biological electron microscopy. *J. Struct. Biol.*, 144(1-2):114–122, 2003.

U. Karls, U. Muller, D. J. Gilbert, N. G. Copeland, N. A. Jenkins, and K. Harbers. Structure, expression, and chromosome location of the gene for the beta subunit of brain-specific Ca2+/calmodulin-dependent protein kinase II identified by transgene integration in an embryonic lethal mouse mutant. *Mol. Cell. Biol.*, 12(8):3644–3652, Aug 1992.

P. T. Kelly, R. K. Yip, S. M. Shields, and M. Hay. Calmodulin-dependent protein phosphorylation in synaptic junctions. *J. Neurochem.*, 45(5):1620–1634, Nov 1985.

M. B. Kennedy. The postsynaptic density at glutamatergic synapses. *Trends Neurosci.*, 20(6):264–268, Jun 1997.

V. N. Kharazia and R. J. Weinberg. Tangential synaptic distribution of NMDA and AMPA receptors in rat neocortex. *Neurosci. Lett.*, 238(1-2):41–44, Nov 1997.

E. Kim and M. Sheng. PDZ domain proteins of synapses. *Nat. Rev. Neurosci.*, 5(10): 771–781, Oct 2004.

C. Kisielowski, B. Freitag, M. Bischoff, H. van Lin, S. Lazar, G. Knippels, P. Tiemeijer, M. van der Stam, S. von Harrach, M. Stekelenburg, M. Haider, S. Uhlemann, H. Mller, P. Hartel, B. Kabius, D. Miller, I. Petrov, E.A. Olson, T. Donchev, E.A. Kenik, A.R. Lupini, J. Bentley, S.J. Pennycook, I.M. Anderson, A.M. Minor, A.K. Schmid, T. Duden, V. Radmilovic, Q.M. Ramasse, M. Watanabe, R. Erni, E.A. Stach, P. Denes, and U. Dahmen. Detection of single atoms and buried defects in three dimensions by aberration-corrected electron microscope with 0.5- information limit. *Microscopy and Microanalysis*, 14:469–477, 10 2008. ISSN 1435-8115.

S. J. Kolodziej, A. Hudmon, M. N. Waxham, and J. K. Stoops. Three-dimensional reconstructions of calcium/calmodulin-dependent (CaM) kinase IIalpha and truncated CaM kinase IIalpha reveal a unique organization for its structural core and functional domains. *J. Biol. Chem.*, 275(19):14354–14359, May 2000.

A. J. Koster, R. Grimm, D. Typke, R. Hegerl, A. Stoschek, J. Walz, and W. Baumeister. Perspectives of molecular and cellular electron tomography. *Journal of Structural Biology*, 120(3):276–308, 1997.

A.J. Koster, W.J. de Ruijter, A. Van Den Bos, and K.D. Van Der Mast. Autotuning of a tem using minimum electron dose. *Ultramicroscopy*, 27(3):251–272, 1989.

A.J. Koster, H. Chen, J.W. Sedat, and D.A. Agard. Automated microscopy for electron tomography. *Ultramicroscopy*, 46(1–4):207–227, 1992.

B. I. Kotlyar, G. G. Khludova, A. A. Myasnikov, P. A. Gusev, and V. F. Lyal'ka. Temporal specificity in the action of stimuli during the formation of associative ultrastructural reorganizations in neurons of the cerebral cortex. *Neurosci. Behav. Physiol.*, 20(4):289–297, 1990.

J. R. Kremer, D. N. Mastronarde, and J. R. McIntosh. Computer visualization of three-dimensional image data using IMOD. *J. Struct. Biol.*, 116(1):71–76, 1996.

O. L. Krivanek, S. L. Friedman, A. J. Gubbens, and B. Kraus. An imaging filter for biological applications. *Ultramicroscopy*, 59(1-4):267–282, Jul 1995.

U. K. Laemmli. Cleavage of structural proteins during the assembly of the head of bacteriophage T4. *Nature*, 227(5259):680–685, Aug 1970.

Y. Lai, A. C. Nairn, and P. Greengard. Autophosphorylation reversibly regulates the Ca2+/calmodulin-dependence of Ca2+/calmodulin-dependent protein kinase II. *Proc. Natl. Acad. Sci. U.S.A.*, 83(12):4253–4257, Jun 1986.

A. S. Leonard, I. A. Lim, D. E. Hemsworth, M. C. Horne, and J. W. Hell. Calcium/calmodulin-dependent protein kinase II is associated with the N-methyl-D-aspartate receptor. *Proc. Natl. Acad. Sci. U.S.A.*, 96(6):3239–3244, Mar 1999.

A. S. Leonard, K. U. Bayer, M. A. Merrill, I. A. Lim, M. A. Shea, H. Schulman, and J. W. Hell. Regulation of calcium/calmodulin-dependent protein kinase II docking to N-methyl-D-aspartate receptors by calcium/calmodulin and alpha-actinin. *J. Biol. Chem.*, 277(50):48441–48448, Dec 2002.

W. Li, A. Okano, Q. B. Tian, K. Nakayama, T. Furihata, H. Nawa, and T. Suzuki. Characterization of a novel synGAP isoform, synGAP-beta. *J. Biol. Chem.*, 276(24): 21417–21424, Jun 2001.

Y. Liu, P.A. Penczek, B. F. McEwen, and J. Frank. A marker-free alignment method for electron tomography. *Ultramicroscopy*, 58(3–4):393–402, 1995.

V. Lučić, F. Forster, and W. Baumeister. Structural studies by electron tomography: from cells to molecules. *Annu. Rev. Biochem.*, 74:833–865, 2005.

V. Lučić, G. J. Greif, and M. B. Kennedy. Detailed state model of CaMKII activation and autophosphorylation. *Eur. Biophys. J.*, 38(1):83–98, Nov 2008.

M. E. Martone, Y. Z. Jones, S. J. Young, M. H. Ellisman, J. A. Zivin, and B. R. Hu. Modification of postsynaptic densities after transient cerebral ischemia: a quantitative and three-dimensional ultrastructural study. *J. Neurosci.*, 19(6):1988–1997, Mar 1999.

D. N. Mastronarde. Dual-axis tomography: an approach with alignment methods that preserve resolution. *J. Struct. Biol.*, 120(3):343–352, Dec 1997.

D. N. Mastronarde. Automated electron microscope tomography using robust prediction of specimen movements. *J. Struct. Biol.*, 152(1):36–51, Oct 2005.

K Matsumoto, T Nakamura, A Yusa, and S Nagai. A new mos phototransistor operating in a non-destructive readout mode. *Japanese Journal of Applied Physics*, 24(5A):L323, 1985.

A. I. Matus and D. H. Taff-Jones. Morphology and molecular composition of isolated postsynaptic junctional structures. *Proc. R. Soc. Lond., B, Biol. Sci.*, 203(1151): 135–151, Dec 1978.

B. F. McEwen, K. H. Downing, and R. M. Glaeser. The relevance of dose-fractionation in tomography of radiation-sensitive specimens. *Ultramicroscopy*, 60(3):357–373, Oct 1995.

A. W. McGee, S. R. Dakoji, O. Olsen, D. S. Bredt, W. A. Lim, and K. E. Prehoda. Structure of the SH3-guanylate kinase module from PSD-95 suggests a mechanism for

regulated assembly of MAGUK scaffolding proteins. *Mol. Cell*, 8(6):1291–1301, Dec 2001.

G. McMullan, S. Chen, R. Henderson, and A. R. Faruqi. Detective quantum efficiency of electron area detectors in electron microscopy. *Ultramicroscopy*, 109(9):1126–1143, Aug 2009.

M. A. Merrill, Y. Chen, S. Strack, and J. W. Hell. Activity-driven postsynaptic translocation of CaMKII. *Trends Pharmacol. Sci.*, 26(12):645–653, Dec 2005.

C. R. Midgett and D. R. Madden. The quaternary structure of a calcium-permeable AMPA receptor: conservation of shape and symmetry across functionally distinct subunit assemblies. *J. Mol. Biol.*, 382(3):578–584, Oct 2008.

C. Millan, R. Lujan, R. Shigemoto, and J. Sanchez-Prieto. Subtype-specific expression of group III metabotropic glutamate receptors and Ca2+ channels in single nerve terminals. *J. Biol. Chem.*, 277(49):47796–47803, Dec 2002.

S. G. Miller and M. B. Kennedy. Distinct forebrain and cerebellar isozymes of type II Ca2+/calmodulin-dependent protein kinase associate differently with the postsynaptic density fraction. *J. Biol. Chem.*, 260(15):9039–9046, Jul 1985.

S. G. Miller and M. B. Kennedy. Regulation of brain type II Ca2+/calmodulin-dependent protein kinase by autophosphorylation: a Ca2+-triggered molecular switch. *Cell*, 44(6):861–870, Mar 1986.

J. A. Mindell and N. Grigorieff. Accurate determination of local defocus and specimen tilt in electron microscopy. *J. Struct. Biol.*, 142(3):334–347, Jun 2003.

N. Mori, T. Oikawa, T. Katoh, J. Miyahara, and Y. Harada. Application of the "imaging plate" to TEM image recording. *Ultramicroscopy*, 25(3):195–201, 1988.

E. P. Morris and K. Torok. Oligomeric structure of alpha-calmodulin-dependent protein kinase II. *J. Mol. Biol.*, 308(1):1–8, Apr 2001.

S. Naisbitt, E. Kim, J. C. Tu, B. Xiao, C. Sala, J. Valtschanoff, R. J. Weinberg, P. F. Worley, and M. Sheng. Shank, a novel family of postsynaptic density proteins that binds to the NMDA receptor/PSD-95/GKAP complex and cortactin. *Neuron*, 23(3): 569–582, Jul 1999.

T. Nakagawa, K. Futai, H. A. Lashuel, I. Lo, K. Okamoto, T. Walz, Y. Hayashi, and M. Sheng. Quaternary structure, protein dynamics, and synaptic function of SAP97 controlled by L27 domain interactions. *Neuron*, 44(3):453–467, Oct 2004.

T. Nakagawa, Y. Cheng, E. Ramm, M. Sheng, and T. Walz. Structure and different conformational states of native AMPA receptor complexes. *Nature*, 433(7025):545–549, Feb 2005.

T. Nakagawa, Y. Cheng, M. Sheng, and T. Walz. Three-dimensional structure of an AMPA receptor without associated stargazin/TARP proteins. *Biol. Chem.*, 387(2): 179–187, Feb 2006.

S. Nickell, F. Forster, A. Linaroudis, W. D. Net, F. Beck, R. Hegerl, W. Baumeister, and J. M. Plitzko. TOM software toolbox: acquisition and analysis for electron tomography. *J. Struct. Biol.*, 149(3):227–234, Mar 2005.

P. Opazo, S. Labrecque, C. M. Tigaret, A. Frouin, P. W. Wiseman, P. De Koninck, and D. Choquet. CaMKII triggers the diffusional trapping of surface AMPARs through phosphorylation of stargazin. *Neuron*, 67(2):239–252, Jul 2010.

N. Otmakhov, J. H. Tao-Cheng, S. Carpenter, B. Asrican, A. Dosemeci, T. S. Reese, and J. Lisman. Persistent accumulation of calcium/calmodulin-dependent protein kinase II in dendritic spines after induction of NMDA receptor-dependent chemical long-term potentiation. *J. Neurosci.*, 24(42):9324–9331, Oct 2004.

Y. Ouyang, A. Rosenstein, G. Kreiman, E. M. Schuman, and M. B. Kennedy. Tetanic stimulation leads to increased accumulation of Ca(2+)/calmodulin-dependent protein

kinase II via dendritic protein synthesis in hippocampal neurons. *J. Neurosci.*, 19(18): 7823–7833, Sep 1999.

G.E. Palade and S.L. Palay. Electron microscopic observations of interneuronal and neuromuscular synapses. *The anatomical record*, 118(2):335–336, 1954.

S. L. Palay. Synapses in the central nervous system. *J Biophys Biochem Cytol*, 2(4 Suppl):193–202, Jul 1956.

S. L. Palay. The morphology of synapses in the central nervous system. *Expl Cell. Res.*, 5(Suppl):275–293, 1958.

P. Penczek, M. Marko, K. Buttle, and J. Frank. Double-tilt electron tomography. *Ultramicroscopy*, 60(3):393–410, Oct 1995.

P. A. Penczek. Three-dimensional spectral signal-to-noise ratio for a class of reconstruction algorithms. *J. Struct. Biol.*, 138(1-2):34–46, 2002.

P. A. Penczek, R. A. Grassucci, and J. Frank. The ribosome at improved resolution: new techniques for merging and orientation refinement in 3D cryo-electron microscopy of biological particles. *Ultramicroscopy*, 53(3):251–270, Mar 1994.

P.A. Penczek. Chapter three-resolution measures in molecular electron microscopy. *Methods in enzymology*, 482:73–100, 2010.

PA Penczek, J Zhu, R Schröder, and J Frank. Three dimensional reconstruction with contrast transfer compensation from defocus series. *Scanning Microsc*, 11:147–154, 1997.

J. Peng, M. J. Kim, D. Cheng, D. M. Duong, S. P. Gygi, and M. Sheng. Semiquantitative proteomic analysis of rat forebrain postsynaptic density fractions by mass spectrometry. *J. Biol. Chem.*, 279(20):21003–21011, May 2004.

A. Peters and I. R. Kaiserman-Abramof. The small pyramidal neuron of the rat cerebral cortex. The perikaryon, dendrites and spines. *Am. J. Anat.*, 127(4):321–355, Apr 1970.

J. D. Petersen, X. Chen, L. Vinade, A. Dosemeci, J. E. Lisman, and T. S. Reese. Distribution of postsynaptic density (PSD)-95 and Ca2+/calmodulin-dependent protein kinase II at the PSD. *J. Neurosci.*, 23(35):11270–11278, Dec 2003.

E. F. Pettersen, T. D. Goddard, C. C. Huang, G. S. Couch, D. M. Greenblatt, E. C. Meng, and T. E. Ferrin. UCSF Chimera–a visualization system for exploratory research and analysis. *J Comput Chem*, 25(13):1605–1612, Oct 2004.

S. Pfeffer, F. Brandt, T. Hrabe, S. Lang, M. Eibauer, R. Zimmermann, and F. Forster. Structure and 3D arrangement of endoplasmic reticulum membrane-associated ribosomes. *Structure*, 20(9):1508–1518, Sep 2012.

C. Racca, F. A. Stephenson, P. Streit, J. D. Roberts, and P. Somogyi. NMDA receptor content of synapses in stratum radiatum of the hippocampal CA1 area. *J. Neurosci.*, 20(7):2512–2522, Apr 2000.

R. J. Racine, N. W. Milgram, and S. Hafner. Long-term potentiation phenomena in the rat limbic forebrain. *Brain Res.*, 260(2):217–231, Feb 1983.

B. Racz, T. A. Blanpied, M. D. Ehlers, and R. J. Weinberg. Lateral organization of endocytic machinery in dendritic spines. *Nat. Neurosci.*, 7(9):917–918, Sep 2004.

M. Rademacher. Weighted back-projection methods. *J. Frank (Ed.), Electron Tomography, Three-Dimensional Imaging with the Transmission Electron Microscope*, pages 91–115, 1992.

J. Radon. ber die bestimmung von funktionen durch ihre integralwerte lngs gewisser mannigfaltigkeiten. *Math Phys Klasse*, 69:262–277, 1917.

B. K. Rath, R. Hegerl, A. Leith, T. R. Shaikh, T. Wagenknecht, and J. Frank. Fast 3D motif search of EM density maps using a locally normalized cross-correlation function. *J. Struct. Biol.*, 144(1-2):95–103, 2003.

Ludwig Reimer and Helmut Kohl. *Transmission electron microscopy: physics of image formation*, volume 36. Springer, 2008.

P. Rellos, A. C. Pike, F. H. Niesen, E. Salah, W. H. Lee, F. von Delft, and S. Knapp. Structure of the CaMKIIdelta/calmodulin complex reveals the molecular mechanism of CaMKII kinase activation. *PLoS Biol.*, 8(7):e1000426, 2010.

A. J. Robison, M. A. Bass, Y. Jiao, L. B. MacMillan, L. C. Carmody, R. K. Bartlett, and R. J. Colbran. Multivalent interactions of calcium/calmodulin-dependent protein kinase II with the postsynaptic density proteins NR2B, densin-180, and alpha-actinin-2. *J. Biol. Chem.*, 280(42):35329–35336, Oct 2005.

A. M. Roseman. Docking structures of domains into maps from cryo-electron microscopy using local correlation. *Acta Crystallogr. D Biol. Crystallogr.*, 56(Pt 10):1332–1340, Oct 2000.

O. S. Rosenberg, S. Deindl, R. J. Sung, A. C. Nairn, and J. Kuriyan. Structure of the autoinhibited kinase domain of CaMKII and SAXS analysis of the holoenzyme. *Cell*, 123(5):849–860, Dec 2005.

O. S. Rosenberg, S. Deindl, L. R. Comolli, A. Hoelz, K. H. Downing, A. C. Nairn, and J. Kuriyan. Oligomerization states of the association domain and the holoenyzme of Ca2+/CaM kinase II. *FEBS J.*, 273(4):682–694, Feb 2006.

W. O. Saxton and W. Baumeister. The correlation averaging of a regularly arranged bacterial cell envelope protein. *J Microsc*, 127(Pt 2):127–138, Aug 1982.

W.O. Saxton, W. Baumeister, and M. Hahn. Three-dimensional reconstruction of imperfect two-dimensional crystals. *Ultramicroscopy*, 13(1):57–70, 1984.

S. H. Scheres. RELION: implementation of a Bayesian approach to cryo-EM structure determination. *J. Struct. Biol.*, 180(3):519–530, Dec 2012.

S. H. Scheres, H. Gao, M. Valle, G. T. Herman, P. P. Eggermont, J. Frank, and J. M. Carazo. Disentangling conformational states of macromolecules in 3D-EM through likelihood optimization. *Nat. Methods*, 4(1):27–29, Jan 2007.

O. Scherzer. The theoretical resolution limit of the electron microscope. *Journal of Applied Physics*, 20(1):20–29, 1949.

T. R. Shaikh, H. Gao, W.T. Baxter, F.J. Asturias, N. Boisset, A. Leith, and J. Frank. Spider image processing for single-particle reconstruction of biological macromolecules from electron micrographs. *Nature protocols*, 3(12):1941–1974, 2008.

K. Shen and T. Meyer. In vivo and in vitro characterization of the sequence requirement for oligomer formation of Ca2+/calmodulin-dependent protein kinase IIalpha. *J. Neurochem.*, 70(1):96–104, Jan 1998.

K. Shen and T. Meyer. Dynamic control of CaMKII translocation and localization in hippocampal neurons by NMDA receptor stimulation. *Science*, 284(5411):162–166, Apr 1999.

K. Shen, M. N. Teruel, K. Subramanian, and T. Meyer. CaMKIIbeta functions as an F-actin targeting module that localizes CaMKIIalpha/beta heterooligomers to dendritic spines. *Neuron*, 21(3):593–606, Sep 1998.

M. Sheng and C. C. Hoogenraad. The postsynaptic architecture of excitatory synapses: a more quantitative view. *Annu. Rev. Biochem.*, 76:823–847, 2007.

M. Sheng and E. Kim. The Shank family of scaffold proteins. *J. Cell. Sci.*, 113 (Pt 11):1851–1856, Jun 2000.

A. I. Sobolevsky, M. P. Rosconi, and E. Gouaux. X-ray structure, symmetry and mechanism of an AMPA-subtype glutamate receptor. *Nature*, 462(7274):745–756, Dec 2009.

C. O. Sorzano, R. Marabini, J. Velazquez-Muriel, J. R. Bilbao-Castro, S. H. Scheres, J. M. Carazo, and A. Pascual-Montano. XMIPP: a new generation of an open-source image processing package for electron microscopy. *J. Struct. Biol.*, 148(2):194–204, Nov 2004.

J.C.H. Spence. *High-Resolution Electron Microscopy*. OUP Oxford, 2013. ISBN 9780191508400.

D.G. Stearns and J.D. Wiedwald. Response of charge-coupled devices to direct electron bombardment. *Review of Scientific Instruments*, 60(6):1095–1103, Jun 1989. ISSN 0034-6748. doi: 10.1063/1.1140323.

S. Strack and R. J. Colbran. Autophosphorylation-dependent targeting of calcium/ calmodulin-dependent protein kinase II by the NR2B subunit of the N-methyl- D-aspartate receptor. *J. Biol. Chem.*, 273(33):20689–20692, Aug 1998.

S. Strack, R. B. McNeill, and R. J. Colbran. Mechanism and regulation of calcium/calmodulin-dependent protein kinase II targeting to the NR2B subunit of the N-methyl-D-aspartate receptor. *J. Biol. Chem.*, 275(31):23798–23806, Aug 2000.

M. Stratton, I. H. Lee, M. Bhattacharyya, S. M. Christensen, L. H. Chao, H. Schulman, J. T. Groves, and J. Kuriyan. Activation-triggered subunit exchange between CaMKII holoenzymes facilitates the spread of kinase activity. *Elife*, 3:e01610, 2014.

Y. Sugiyama, I. Kawabata, K. Sobue, and S. Okabe. Determination of absolute protein numbers in single synapses by a GFP-based calibration technique. *Nat. Methods*, 2 (9):677–684, Sep 2005.

T. Suzuki. Lipid rafts at postsynaptic sites: distribution, function and linkage to post-synaptic density. *Neurosci. Res.*, 44(1):1–9, Sep 2002.

T. Suzuki, K. Okumura-Noji, R. Tanaka, and T. Tada. Rapid translocation of cytosolic Ca2+/calmodulin-dependent protein kinase II into postsynaptic density after decapitation. *J. Neurochem.*, 63(4):1529–1537, Oct 1994.

L. W. Swanson, T. J. Teyler, and R. F. Thompson. Hippocampal long-term potentiation: mechanisms and implications for memory. Based on an NRP Work Session. *Neurosci Res Program Bull*, 20(5):613–769, Jun 1982.

M. T. Swulius, Y. Kubota, A. Forest, and M. N. Waxham. Structure and composition of the postsynaptic density during development. *J. Comp. Neurol.*, 518(20):4243–4260, Oct 2010.

G. Tang, L. Peng, P. R. Baldwin, D. S. Mann, W. Jiang, I. Rees, and S. J. Ludtke. EMAN2: an extensible image processing suite for electron microscopy. *J. Struct. Biol.*, 157(1):38–46, Jan 2007.

K. A. Taylor and R. M. Glaeser. Electron microscopy of frozen hydrated biological specimens. *Journal of Ultrastructure Research*, 55(3):448–456, 1976.

A. Thalhammer, Y. Rudhard, C. M. Tigaret, K. E. Volynski, D. A. Rusakov, and R. Schoepfer. CaMKII translocation requires local NMDA receptor-mediated Ca2+ signaling. *EMBO J.*, 25(24):5873–5883, Dec 2006.

W. Tichelaar, M. Safferling, K. Keinanen, H. Stark, and D. R. Madden. The Three-dimensional Structure of an Ionotropic Glutamate Receptor Reveals a Dimer-of-dimers Assembly. *J. Mol. Biol.*, 344(2):435–442, Nov 2004.

T. Tobimatsu and H. Fujisawa. Tissue-specific expression of four types of rat calmodulin-dependent protein kinase II mRNAs. *J. Biol. Chem.*, 264(30):17907–17912, Oct 1989.

R. M. Tombes, M. O. Faison, and J. M. Turbeville. Organization and evolution of multifunctional Ca(2+)/CaM-dependent protein kinase genes. *Gene*, 322:17–31, Dec 2003.

J. C. Trinidad, C. G. Specht, A. Thalhammer, R. Schoepfer, and A. L. Burlingame. Comprehensive identification of phosphorylation sites in postsynaptic density preparations. *Mol. Cell Proteomics*, 5(5):914–922, May 2006.

D. Typke, K. Dierksen, and W. Baumeister. Automatic electron tomography. *Proceedings of the 49th Annual Meeting of the Microscopy Society of America*, pages 544–545, 1991.

D. Typke, R. Hegerl, and J. Kleinz. Image restoration for biological objects using external {TEM} control and electronic image recording. *Ultramicroscopy*, 46(1-4): 157–173, 1992.

M. Unser, C. O. Sorzano, P. Thevenaz, S. Jonić, C. El-Bez, S. De Carlo, J. F. Conway, and B. L. Trus. Spectral signal-to-noise ratio and resolution assessment of 3D reconstructions. *J. Struct. Biol.*, 149(3):243–255, Mar 2005.

J. G. Valtschanoff and R. J. Weinberg. Laminar organization of the NMDA receptor complex within the postsynaptic density. *J. Neurosci.*, 21(4):1211–1217, Feb 2001.

M. Van Heel. Angular reconstitution: a posteriori assignment of projection directions for 3d reconstruction. *Ultramicroscopy*, 21(2):111–123, 1987.

M. van Heel and M. Schatz. Fourier shell correlation threshold criteria. *J. Struct. Biol.*, 151(3):250–262, Sep 2005.

D. Vanhecke, S. Asano, Z. Kochovski, R. Fernandez-Busnadiego, N. Schrod, W. Baumeister, and V. Lučić. Cryo-electron tomography: methodology, developments and biological applications. *Journal of Microscopy*, 242(3):221–227, 2011.

R. S. Walikonis, A. Oguni, E. M. Khorosheva, C. J. Jeng, F. J. Asuncion, and M. B. Kennedy. Densin-180 forms a ternary complex with the (alpha)-subunit of Ca2+/calmodulin-dependent protein kinase II and (alpha)-actinin. *J. Neurosci.*, 21 (2):423–433, Jan 2001.

J. Walz, T. Tamura, N. Tamura, R. Grimm, W. Baumeister, and A. J. Koster. Tricorn protease exists as an icosahedral supermolecule in vivo. *Mol. Cell*, 1(1):59–65, Dec 1997.

V. P. Whittaker. Thirty years of synaptosome research. *J. Neurocytol.*, 22(9):735–742, Sep 1993.

V.P. Whittaker. The synaptosome. In Abel Lajtha, editor, *Structural Elements of the Nervous System*, pages 1–39. Springer US, 1984. ISBN 978-1-4684-4588-6.

N. Wiener. *Extrapolation, interpolation, and smoothing of stationary time series: with engineering applications*. MIT press, Cambridge, MA, 1949.

M. Xu, M. Beck, and F. Alber. Template-free detection of macromolecular complexes in cryo electron tomograms. *Bioinformatics*, 27(13):69–76, Jul 2011.

E. Yang and H. Schulman. Structural examination of autoregulation of multifunctional calcium/calmodulin-dependent protein kinase II. *J. Biol. Chem.*, 274(37):26199–26208, Sep 1999.

L. H. Yen, J. T. Sibley, and M. Constantine-Paton. Fine-structural alterations and clustering of developing synapses after chronic treatments with low levels of NMDA. *J. Neurosci.*, 13(11):4949–4960, Nov 1993.

Z. H. Zhou and W. Chiu. Prospects for using an {IVEM} with a {FEG} for imaging macromolecules towards atomic resolution. *Ultramicroscopy*, 49(14):407 – 416, 1993. ISSN 0304-3991.

U. Ziese, W. J. Geerts, T. P. Van Der Krift, A. J. Verkleij, and A. J. Koster. Correction of autofocusing errors due to specimen tilt for automated electron tomography. *J Microsc*, 211(Pt 2):179–185, Aug 2003.

11 Acknowledgements

I would like to thank all the people that made the completion of this doctoral dissertation possible in one way or another.

First and foremost I wish to thank Professor Wolfgang Baumeister for both giving me the opportunity to join his department and for his guidance and support throughout my time there.

My direct supervisor, Vladan Lučić, for his patience, help and support as well as for fruitful discussions and proof reading of my thesis.

Oana Michalache for her invaluable help with sample preparation and data collection.

Jürgen Plitzko and Günter Pfeiffer for always being ready to help when a microscope wasn't behaving.

Radostin Danev for helpful discussions and valuable tips on sample preparation.

Birgit Book, Inga Wolf, Sabina Von Polenz and Nathalie Leclercq for making my life much easier.

Florian Beck, Thomas Hrabe and Yuxiang Chen for their help and support on various aspects of image processing.

The whole Department of Molecular Structural Biology, but especially the Lučić group, for the great work atmosphere and great times spent out of the lab.

I would like to thank Dennis Zimmerman for the fruitful collaboration on the CaMKII project that wouldn't have even started without him.

Special thanks goes to my girlfriend Denitsa for her endless patience, support and ability to cheer me up after each and every setback that I have encountered during that time.

Last but not least, I would like to thank my family and especially my parents for raising me up to be the man I am today. Without you none of this would have been possible.

12 Publication List

- R. Fernandez-Busnadiego, S. Asano, AM. Oprisoreanu, E. Sakata, M. Doengi, **Z. Kochovski**, M. Zürner, V. Stein, S. Schoch, W. Baumeister, and V. Lučić. (2013). Cryo-electron tomography reveals a critical role of RIM1α in synaptic vesicle tethering. *The Journal of cell biology*, 201 (5), 725-740.

- R. Fernandez-Busnadiego, N. Schrod, **Z. Kochovski**, S. Asano, D. Vanhecke, W. Baumeister and V. Lučić. (2011). Insights into the molecular organization of the neuron by cryo-electron tomography. *Journal of electron microscopy*, 60 (suppl 1), S137-S148.

- D. Vanhecke, S. Asano, **Z. Kochovski**, R. Fernandez-Busnadiego, N. Schrod, W. Baumeister and V. Lučić. (2011). Cryo-electron tomography: methodology, developments and biological applications. *Journal of microscopy*, 242 (3), 221-227.

List of Tables

List of Figures